Utrecht University

Institute for Theoretical Physics

The Fractal-Lattice Hubbard Model

Master Thesis

Monica Conte

Supervisors:

Prof. Dr. C. Morais Smith
Utrecht University

Dr. V. Zampronio
Universidade Federal do Rio Grande do Norte

Second Supervisor:

Dr. L. Fritz
Utrecht University

July 7, 2023

Abstract

The Hubbard model is the prototypical model to describe strongly-correlated electrons hopping in a lattice, with hopping parameter t and on-site interactions U. It captures the rich physics of metal-insulator transition, high-Tc superconductors, and spin liquids. Despite being "simple", the Hubbard Hamiltonian does not have an analytical solution in more than one dimension. It has been studied numerically in several dimensions, but not in fractal dimensions. In this project, we investigate the fractal-lattice Hubbard model using various numerical simulations: exact diagonalization, the self-consistent diagonalization of a (mean-field) Hartree-Fock Hamiltonian and state-of-the-art Auxiliary-Field Quantum Monte Carlo. In the tight-binding limit, we found compact localised states, that we understood in terms of symmetry and linked to the formation of a ferrimagnetic phase at weak interaction. Moreover, simulations at half-filling revealed the persistence of this type of magnetic order for every value of interaction strength and a Mott transition for $U/t \sim 4.5$. Finally, we found a remarkable dependence on the Hausdorff dimension regarding i) the number of compact localised states in different generations, ii) the scaling of the total many-body ground-state energy in the tight-binding limit, and iii) the density of the states at the corners for specific values of electronic filling.

Contents

1 Introduction

The Hubbard model is one of the simplest and most fundamental models for describing the movement and interactions of electrons on a lattice. In Solid-State physics, a widely employed approach to describe electron motion within a lattice is the tight-binding method. This method assumes that electrons are tightly bound to lattice sites, with a non-negligible probability of tunneling to neighboring sites, characterized by a parameter denoted as t. While this approach allows for the independent treatment of electrons, it fails to account for correlations originated from the Coulomb interaction. The Hubbard model effectively addresses this by introducing an interaction term, parameterized by U, enabling the study of various phases of the system. Notably, the Hubbard model describes Mott transitions, which are transitions between metallic and insulating behaviors driven by electron-electron interaction. These transitions cannot be predicted by the tight-binding approach. Furthermore, the Hubbard model can capture exotic phases of matter, such as spin and density waves, quantum spin liquids, and high-temperature superconductivity. Despite its simplicity, the Hubbard model remains unsolved analytically in dimensions higher than one, requiring the use of numerical methods. Examples of numerical methods employed to implement the Hubbard Hamiltonian include Density Matrix Renormalization Group (DMRG) [1], Variational Monte Carlo [2], and Quantum Monte Carlo [3]. The latter is the one that will be applied in this work.

This thesis delves into a crucial question: How do electrons behave in a non-integer dimension when described by the Hubbard model? The focus of our investigation revolves around exploring this intriguing phenomenon. Fractals offer a way to explore lattice configurations with non-integer dimensions. These geometrical structures are characterized by their intricate and self-replicating geometric patterns, which are obtained through iterative processes, where a basic shape is repeatedly transformed or replicated. In our study, we construct the lattice configuration using a specific type of fractal, the Sierpinski triangle. This fractal emerges by dividing an initial equilateral triangle into smaller triangles, removing the central portion, and continuing the process iteratively. This iterative removal of portions of the geometry leads to a lattice dimension that lies between 1 and 2. Indeed, the fractal or Hausdorff dimension of the Sierpinski trinagle in 1.58. By utilizing this fractal to build a lattice, we can delve into the unique properties and behaviors that emerge from the interplay between the Hubbard model and fractal geometry.

The outilne of the thesis is the following. In the opening chapter, we provide a concise introduction to fractal geometries and the selected fractal lattice. We highlight significant properties of the lattice, including non-periodicity, diverse connectivity between lattice sites, and bipartiteness. These characteristics establish a solid foundation for studying quantum systems. Importantly, these properties challenge conventional approaches, such as band theory, requiring the exploration of alternative methods to comprehend and analyze particle behavior on this types of lattices. We conclude this chapter by presenting some experimental results in fractal, that out in evidence their applicability in the real world.

In the second chapter, we discuss the Hubbard Model, initially providing an introduction to some preliminary concepts of Many-Body and Solid-State Physics. These notions lay the foundation for the framework within which our work operates. Building upon the fundamental notions of Solid-State Physics, we derive the Hubbard Hamiltonian. Subsequently, we describe the terms comprising the Hamiltonian, offering physical interpretations for each term. Finally, we provide a concise summary of the current state of research on the Hubbard Model, focusing on the relevant results that contribute to our study.

We initiate our study by examining the tight-binding limit, as we anticipate that the lattice connectivity will predominantly influence the electron dynamics on the lattice. The implementation method employed in this limit is based on the tight-binding approach, enabling the independent treatment of electrons. We solve the Hamiltonian in the single-electron basis and construct the many-body wave function by taking anti-symmetrized linear combination of single-electron orbitals. In the ground state, we investigate the distribution of the average density per site and analyze the many-body ground-state energy as a function of electronic filling. Furthermore, we focus on analyzing the energy spectrum of the Hamiltonian in the single-electron basis and explore relevant scaling behaviors. In fact, the property of self-similarity exhibited by fractals suggests potential scaling properties of quantities on the lattice, which we aim to investigate in our study.

In the final chapter, we introduce the crucial aspect of electron-electron interaction and employ three distinct numerical methods to implement it: exact diagonalization, mean-field Hartree-Fock approximation, and Constrained-Path Auxiliary-Field Quantum Monte Carlo (CP-AFQMC). Among these methods, we predominantly utilize CP-AFQMC due to its numerically exact nature. We provide a comprehensive explanation of the underlying theory behind each numerical approach, followed by a comparative analysis to discern their respective strengths and limitations. Subsequently, we investigate the implications of electron-electron interaction on the results obtained from the tight-binding model. Finally, we study the different phases exhibited by the system under the influence of interaction.

2 | Fractals

In this chapter, we introduce fractal geometries and the fractal lattice, which is the chosen lattice configuration for our model. We begin by discussing the motivations behind the choice of working on fractal geometries, highlighting some of their notable properties. Specifically, we focus on the Sierpinski triangle, from which we explain how to build the fractal lattice. We mention some of the remarkable properties that these lattice possesses, as they have implications on the behavior of the implemented Hubbard model. Finally, we highlight the practical applicability of fractals by presenting experimental results that underscore their relevance in the real world.

2.1 Fractal Geometries

The realm of fractal geometries offers a captivating and unconventional viewpoint on the nature of shape and structure. Diverging from traditional Euclidean geometries, which deal with smooth curves and regular shapes, fractals explore the domain of intricate patterns, self-replication, and infinite complexity.

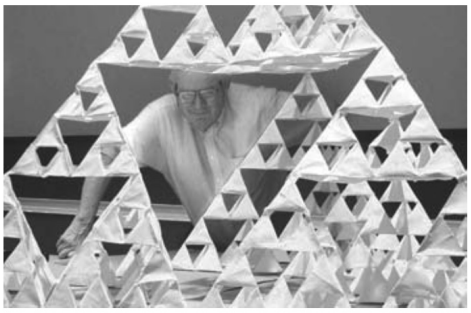

Figure 2.1: Benoit Mandelbrot [4].

Fractals are geometrical constructs that possess the fascinating property of self-similarity, meaning they exhibit similar structures at varying scales. Coined by Benoit Mandelbrot, Figure(2.1), in 1975, the term fractal originates from the Latin word fractus, signifying broken or irregular. Natural and artificial phenomena often showcase fractal characteristics, such as the branching patterns of trees, leaf veins, coastlines' intricate outlines, and even the convoluted shapes of clouds. Figure (2.2) shows some of these fractal configurations in nature.

What sets fractals apart from conventional geometric forms is their ability to maintain intricate

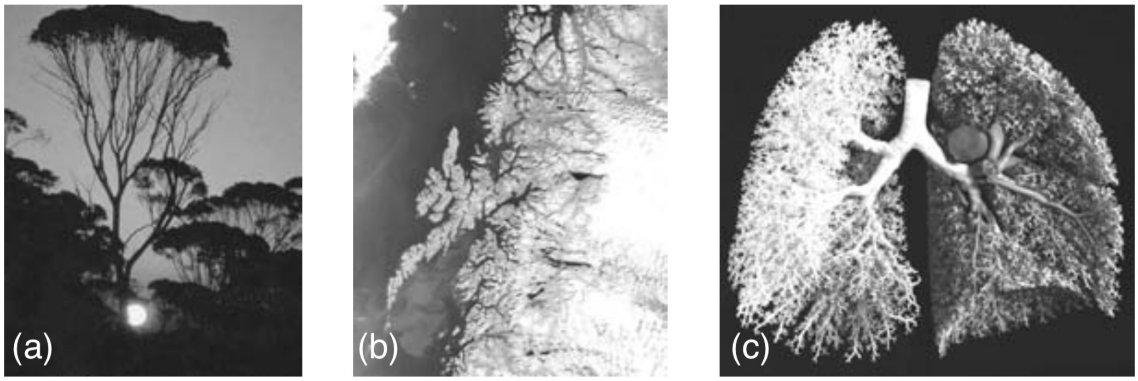

Figure 2.2: Fractal geometries in nature [4]. (a) A tree, (b) a coastline, (c) circulatory casts.

patterns, regardless of the level of magnification. This recursive property creates an infinite level of detail and complexity, making fractals captivating subjects of exploration.

Fractals can be generated through iterative mathematical processes involving repeated geometric transformations. With each iteration, the fractal pattern evolves and becomes increasingly intricate. Additionally, mathematical equations and algorithms can describe fractals, offering avenues for creation and exploration of these geometric forms.

The utility of fractal geometries spans across various fields apart from Physics, such as Mathematics, Computer Graphics, and Art. Fractals provide insights into the structures of natural phenomena, offer tools for data analysis and compression, and inspire artistic creations that capture the mesmerizing beauty of complexity.

2.2 Dimension of Fractals

This section begins by introducing the Sierpinski triangle, which serves as the fractal geometry for the construction of the fractal lattice studied throughout the thesis. The dimension of the Sierpinski triangle is calculated using an intuitive formula. Additionally, we introduce another type of fractal, the Sierpinski carpet, and apply a similar dimension calculation. The inclusion of this second fractal enables the discussion of an experiment, in the final section of this chapter, that utilizes this geometry.

The Sierpinski triangle is constructed through an iterative process that starts with a single equilateral triangle, see Figure 2.3(a). In the first iteration, we divide each side of the triangle into two equal segments and select the downward looking equilateral triangle in the center, as shown in Figure 2.3(b). We then remove this triangle to obtain the first generation of the Sierpinski triangle, see Figure 2.3(c). We repeat this process for each newly formed triangle in the subsequent

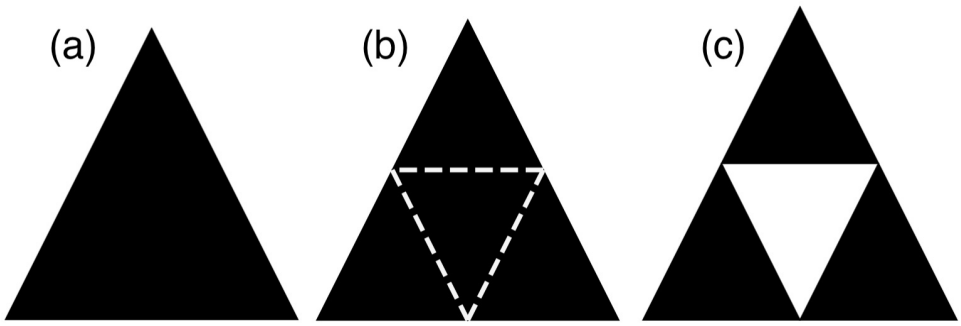

Figure 2.3: One step of the process to build the Sierpinski triangle. (a) An equilateral triangle, (b) the original triangle with inner downward triangle selected, (c) the first generation of the Sierpinski triangle.

iterations. In Figure 2.4(a) we show the second generation. As the iterations continue indefinitely, the Sierpinski triangle emerges, revealing its intricate self-similar structure composed of smaller triangles within larger ones. This recursive construction results in a fractal pattern, Figure 2.4(b), that exhibits remarkable complexity and detail.

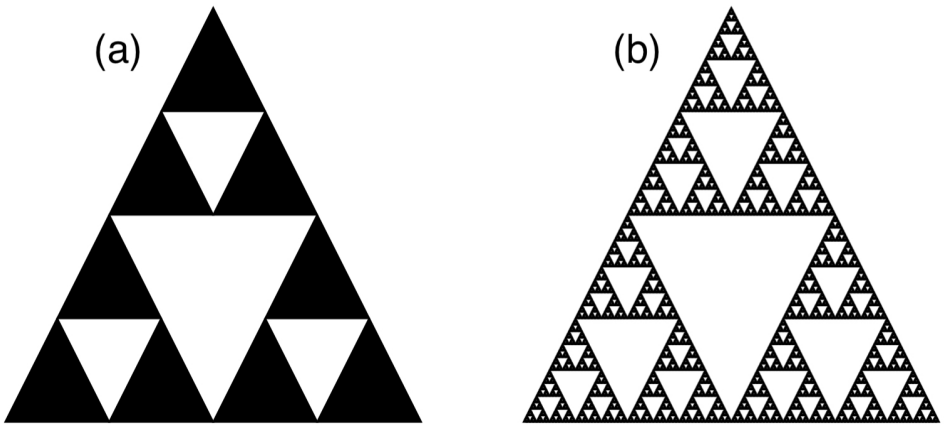

Figure 2.4: (a) Second generation of the Sierpinski triangle, (b) the Sierpinski triangle.

There are various methods that allow to compute the dimension of an object. In this work, we adopt a specific approach that has the advantage of being intuitively understandable. To begin with, we outline the general concept before applying it to the specific shapes. In this method, we utilize the scaling factor, α, and the formula

$$2^d = \alpha. \tag{2.1}$$

which allows us to determine the dimension, represented by the variable d. The scaling factor represents the ratio of the size of an object or structure at a particular iteration to its size in the previous iteration. By applying logarithms to both sides of the equation, we can solve for the fractal dimension.

Let us start by applying the formula to a square with edges of length L. When we double the length of the edge to $2L$, we find $N_{copies} = 4$ copies of the original square, as illustrated in Figure (2.5).

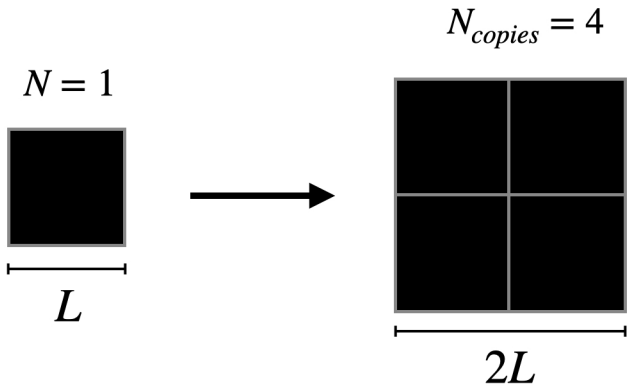

Figure 2.5: Pictorial representation of the procedure used to compute the dimension of an object, applied to a square.

The scaling factor is defined as the ratio

$$\alpha = \frac{N_{copies}}{N}$$

where N is the number of original squares, in our case $N = 1$. Solving equation (2.1) with this value of α, we obtain that the dimension of a square is $d = 2$.

Regarding the dimension of the Sierpinski triangle, we consider the first generation of the triangle, with basis of length L. Once again, we double the size of the base to $2L$, but now we get $N_{copies} = 3$ copies of the original geometry, as we can see in Figure (2.6). Equation (2.1), with

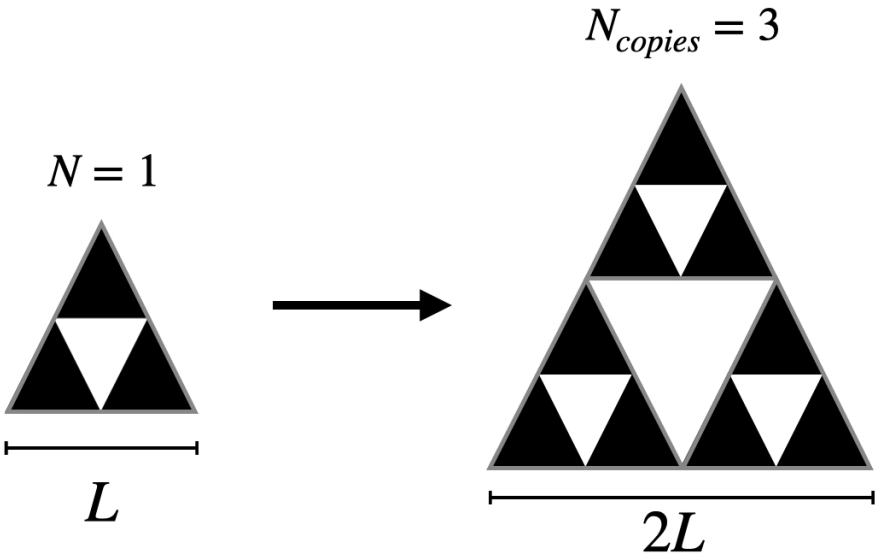

Figure 2.6: In (a) second generation of the Sierpinski triangle, in (b) the Sierpinski triangle.

this value of scaling α, suggests that the dimension of the fractal geometry we consider is not integer. It is in fact given by

$$d = \frac{\log 3}{\log 2} \simeq 1.58.$$

This remarkable property is one of the reasons why we are interested in a fractal geometry. One of our motivations is indeed to study Physics in a non-integer dimension.

The formula we just introduced only holds when we double the external perimeter of the object and the area scales α times. We adopt this choice to make the formula intuitive. However, it can be generalized to the case where we triplicate the external perimeter. Let us consider another fractal geometry, the Sierpinski carpet. Figure (2.7) illustrates the first four generations

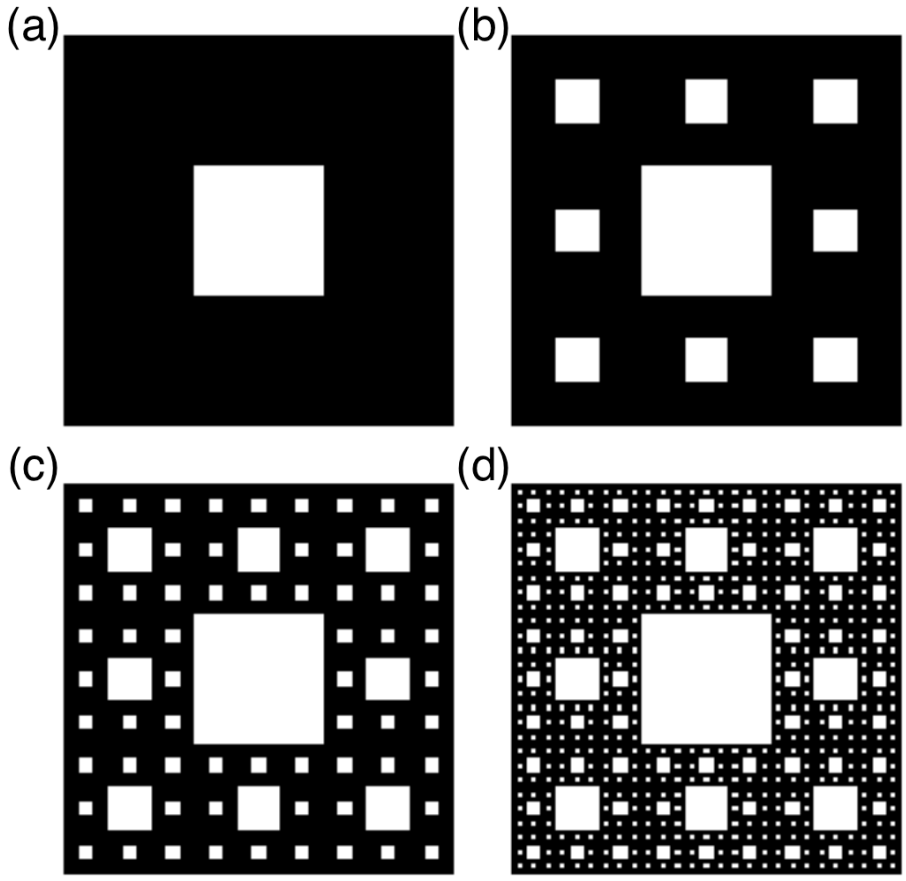

Figure 2.7: (a) First, (b) second, (c) third, (d) fourth generation of the Siepinski carpet.

of the fractal. To determine the dimension of this geometry, we can apply the same formula as before, but now we need to scale the length of the original geometry by a factor of 3. By comparing Figure 2.7(a) and Figure 2.7(b), we observe that this process generates eight copies of the system. Consequently, the dimension of this fractal structure is given by:

$$d = \frac{\log 8}{\log 3} \simeq 1.89.$$

2.3 The Fractal Lattice

Now that we have constructed the geometrical structure, we proceed building the lattice configuration. This involves placing lattice sites at the center and corners of every triangle in the Sierpinski structure. These sites are then linked together, ensuring that all the links have the same length. In Figure 2.8(a), we can observe the resulting lattice configuration for the second generation.

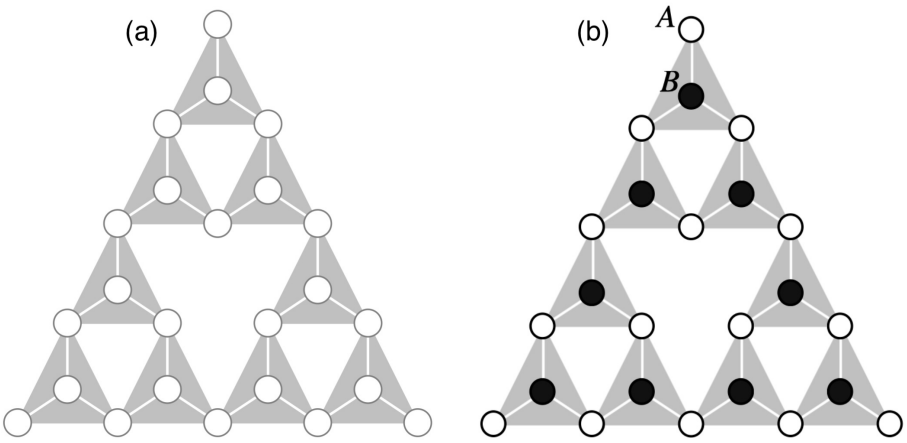

Figure 2.8: (a) Fractal lattice built from the second generation of the Sierpinski triangle. (b) Shows the division in two sub-lattices in the second generation: sites with a black dot belong to sub-lattice B, sites with a white dot belong to sub-lattice A.

A characteristic feature of the resulting lattice geometry is that sites in the lattice have different connectivity. In fact, there are sites linked to their neighbours through three connections, sites that are connected by two links and the sites, in the corners, that are connected by just one link to the rest of the lattice.

It is important to highlight a significant property of this lattice configuration for future considerations: it is bipartite. This means that it can be divided into two sub-lattices, such that each site in one sub-lattice has neighboring sites in the other sub-lattice. In Figure 2.8(b), we can observe that the second generation of the lattice can be effectively partitioned into two sub-lattices: sub-lattice A, consisting of $N_A = 15$ sites, and sub-lattice B, consisting of $N_B = 9$ sites. It is worth noting that this property carries substantial implications for the physics of the model, as will be elaborated in the following chapters.

2.4 Fractals in experiments

Fractal geometries, not only confined to theoretical investigations, have also been successfully realized in experimental settings, offering empirical validation of theoretical concepts. A recent study [5] exemplifies this by demonstrating the controlled construction and characterization of a fractal lattice with electrons. The experiment involved confining electrons on a Cu(111) surface within a self-similar 35 Sierpinski geometry. This intricate lattice structure was achieved through precise atomic manipulation of CO molecules on the Cu(111) surface. By strategically arranging these molecules, the researchers successfully created a fractal lattice configuration with electrons, providing a platform for experimentally investigating the interplay between fractal geometry and electronic properties. In Figure (2.9), the experimental realization of the first three generations of the Sierpinksi triangle.

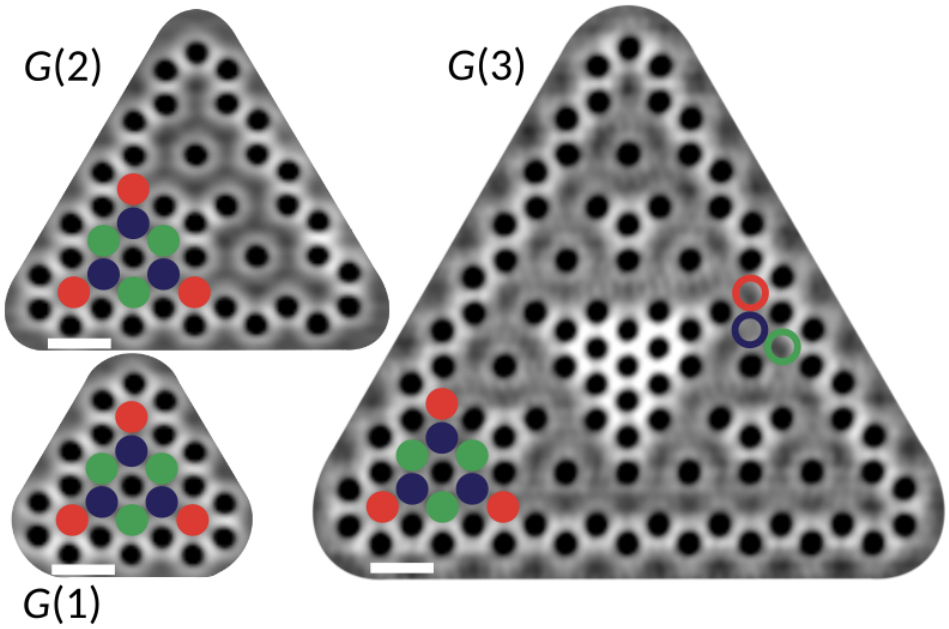

Figure 2.9: Experimental realization of the first three generations of the Sierpinski triangle G(1), G(2) and G(3) [5]. These images where generated using a constant-current scanning tunneling microscopy technique. In the figures, the dots indicate lattice sites and are a guide to the eye.

Another important experimental result on fractal geometries regards quantum transport in fractal photonic lattices [6]. These experiments explored various fractal geometries, including the Sierpinski triangle and Sierpinski carpet. Intriguingly, quantum transport in fractals exhibits anomalous behavior, deviating from the expected patterns observed in infinite regular lattices. Notably, the mean square displacement (MSD), a measure of particle spread, exhibits different regimes in fractals. Of particular interest is the fractal regime, where the behavior of the MSD is solely determined by the fractal dimension.

Finally, we would like to present a recent research that regards Higher Order Topological Insulators (HOTI) in the Sierpinski carpet [7]. A topological insulator is a quantum material that behaves as an insulator in the $d-$dimensional bulk but possesses conducting states on its $(d-1)-$dimensional surfaces or edges, protected by topological properties against impurities or disorder. A HOTI is a specialized class of topological insulators where protected boundary states exist at dimensions $2-d$ or lower. Hence, a $2d$ HOTI would have $0d$ corner modes, and a $3d$ HOTI would have a $1d$ hinges or $0d$ corner state. Through applying the Benalcazar, Bernevig, and Hughes model [8] into a Sierpinski carpet fractal lattice, a recent study revealed the presence of zero-dimensional inner corner states and 1.89-dimensional outer corner states. Remarkably, the dimension of these states coincides with the dimension of the fractal [7]. The experimental realization of these states is shown in Figure (2.10). They also found these states

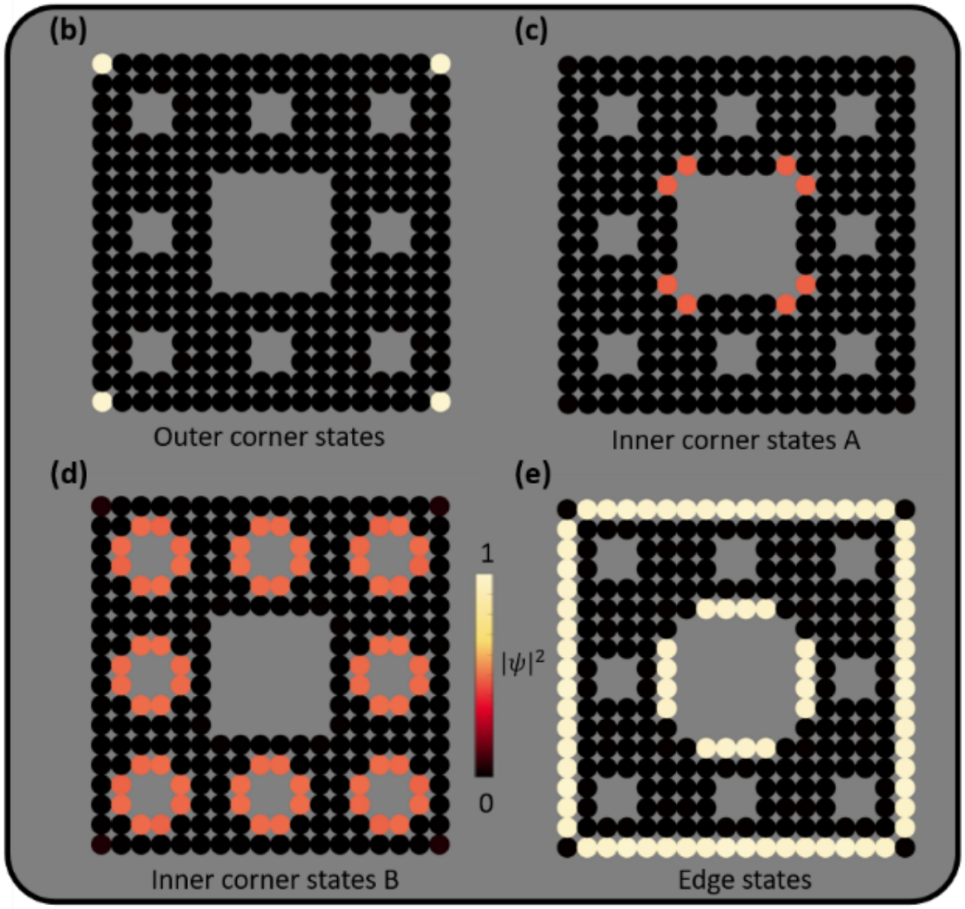

Figure 2.10: Spatial distribution of outer and inner corner states [7].

to be topologically non trivial. These counter-intuitive results indicate that the HOTIs in the fractal model are significantly different from the conventional HOTIs. These results were also observed experimentally with acoustic measurements [7].

3 | The Hubbard Model

The Hubbard model is one of the cornerstone models in Condensed Matter Physics, due to its ability to describe many properties and phases of matter while being simple in its formulation. It was introduced simultaneously, but independently, in 1963 by Martin Gutzwiller[9], Junjiro Kanamori[10] and John Hubbard[11] to study the physics of correlated electrons in solids, when a great effort was made to understand magnetism in transition metals. After 60 years of its introduction, its applicability and relevance goes surprisingly far beyond that initial context.

Explained in a simple way, which reflects the simplicity of the model itself, the Hubbard Model introduces interaction to a tight-binding description of electrons in a solid. In Solid-State Physics (SSP), a tight-binding model assumes the electron to be tightly bounded to the atoms of the solid. This, in turn, can be considered as a lattice of sites where the electrons are allowed to move. The Hubbard model introduces an on-site interaction between electrons on the same lattice sites, accounting for their Coulomb interaction.

The additional interaction term allowed the model to explain and predict the existence of a type of insulators, called *Mott insulators*, which are expected to be conductors by conventional band theory. As explained in more detailed in the next sections, the insulating nature of these materials originates from correlations between electrons, which are not taken into account by ordinary band theory. The Mott transition is just the first important achievement of the Hubbard model, the discovery of many interesting effects followed.

The versatility of the model is demonstrated by its applicability to a wide range of lattice structures, leading to the exploration of numerous phases. For example, when applied to square lattices, the model unveils the interesting physics of antiferromagnetism [12], charge and spin density waves [13] and superconductivity [14]. The model's extension to other lattice geometries, such as triangular lattices, has enabled the discovery of new exotic phases, such as spin liquids [15], which originate from magnetic frustration. These diverse applications showcase the significance of the model in elucidating new phases and understanding complex materials. Finally, a boost of activity regarding the Hubbard model followed the discovery of high-temperature superconductivity, since an adaptation of the model constitutes a candidate for hosting such a behaviour [16].

While significant progress has been made, the full understanding of the Hubbard model and

its intricate phases remains a challenging task. Despite its deceptive simple form, the Hubbard model is not analytically solvable in more than one dimension. For this reason, the study of the model usually requires the implementation of numerical techniques, DMRG (Density Matrix Renormalization Group) and QMC (Quantum Monte Carlo) methods being some of them. In this thesis, we apply the later.

In this chapter, after revising some concepts from Many-Body Quantum Physics and Sold-State Physics, we derive the Hubbard Hamiltonian. Subsequently, we provide a brief discussion on the current state of research on the Hubbard Model, focusing on the significant findings relevant to our study and without claiming to be exhaustive.

3.1 Preliminary notions

In order to derive the Hubbard Hamiltonian and become familiarized with the concepts and methods developed in this work, we dedicate the following two sections to some preliminary notions.

The first sub-section regards second quantization in Many-Body Quantum Physics. First, we extend the principles of single-particle states in quantum mechanics to many-particle systems. Then, we introduce the concept of second quantization, which better suits the model we consider. This approach allows us to effectively capture the dynamics and characteristics of these complex systems.

In the second sub-section, we delve into basic concepts in SSP in order to provide a framework for understanding the formulation of the Hubbard Hamiltonian.

3.1.1 Second Quantization in Many-Body Systems

In quantum mechanics, a single-particle state is represented by a vector in the Hilbert space $\mathcal{H}$ of general dimension n. We denote by $\{|\chi_i\rangle\}_{i=1}^n$ an orthonormal basis of the space and by $\chi_i(\boldsymbol{r}) = \langle \boldsymbol{r}|\chi_i\rangle$ the orbitals of $\mathcal{H}$, with $\boldsymbol{r}$ the space coordinates of the particle. A general wave-function $\phi(\boldsymbol{r})$ can be written as a linear combination of such orbitals,

$$\phi(\boldsymbol{r}) = \langle \boldsymbol{r}|\phi\rangle = \sum_{i=1}^{n} \phi_i \chi_i(\boldsymbol{r}),$$

where we used the completeness of the basis. Quantum mechanics postulates that the probability to find a particle associated to this wave-function $\phi(\boldsymbol{r})$ in an infinitesimal volume element $d\boldsymbol{r}$ around $\boldsymbol{r}$ is given by $|\phi(\boldsymbol{r})|^2 d\boldsymbol{r}$.

Our goal is to generalize the one-particle formalism to a system with N particles and obtain the corresponding many-body wave-function $\Phi(\boldsymbol{R})$, which can be interpreted as [17]:

$$|\Phi(\boldsymbol{R})|^2 \prod_{j=1}^{N} d\boldsymbol{r}_j = \left\{ \begin{array}{c} \text{Probability of finding the } N \text{ particles in the} \\ \text{volume } \prod_{j=1}^{N} d\boldsymbol{r}_j \text{ surrounding } \boldsymbol{R} \end{array} \right\},$$

with $\boldsymbol{R} = (\boldsymbol{r}_1, \boldsymbol{r}_2, \cdots, \boldsymbol{r}_N)$ the configuration of the system containing the coordinates $\boldsymbol{r}_j$ of each particle. The Hilbert space describing N non-interacting particles is the tensor product between the N single-particle spaces

$$\mathcal{H} = \mathcal{H}_1 \otimes \mathcal{H}_2 \otimes \cdots \otimes \mathcal{H}_N,$$

and a general state as the tensor product of single-particle states

$$|\phi_1\rangle \otimes |\phi_2\rangle \otimes \ldots |\phi_N\rangle \,. \tag{3.1}$$

We are now going to show that an orthonormal basis of this space can be constructed by taking the tensor product of single particle basis states:

$$\{|\chi_{i_1}\rangle\}_{i_1}^{n_1} \otimes \{|\chi_{i_2}\rangle\}_{i_2}^{n_2} \otimes \cdots \otimes \{|\chi_{i_N}\rangle\}_{i_N}^{n_N} \,,$$

where $|\chi_{i_j}\rangle$ stands for the set of orthonormal basis of the j-th particle and n_j the dimension of its Hilbert space. Since the single-particle states are orthonormal themselves, it is trivial to see that the set is orthonormal. To show that it is complete, we use the fact that in Equation (3.1) the single particle wave-functions themselves can be decomposed on their basis,

$$|\Phi\rangle = \sum_{i_1, i_2, \ldots, i_N} \phi_{i_1}\phi_{i_2}\ldots\phi_{i_N} \, |\chi_{i_1}\rangle \otimes |\chi_{i_2}\rangle \otimes \cdots \otimes |\chi_{i_N}\rangle \,,$$

proving that any general state can be written as a linear combination of the $\{|\chi\rangle\}$ set, which is thus a basis. We are now able to write the N-particle wave function in the space configuration

$$\Phi(\boldsymbol{R}) = \sum_{i_1, i_2, \ldots, i_N} \phi_{i_1}\phi_{i_2}\ldots\phi_{i_N}\chi_{i_1}(\boldsymbol{r}_1)\chi_{i_2}(\boldsymbol{r}_2)\ldots\chi_{i_N}(\boldsymbol{r}_N). \tag{3.2}$$

However, in systems of identical particles, interchanging two spacial should lead to the same physical result. Thus, the wave-function differs by at most a phase $\lambda = e^{i\theta}$ and, in two dimensions it describes particles called anyons. For three or more dimensions, the phase can take values $\lambda = \pm 1$ and the wave-function will be, respectively, symmetric or anti-symmetric with respect to the exchange of coordinates. Since we are dealing with fermions, the latter case will be considered. Because of this requirement, the meaningful sector in the N-particle space is made of properly antisymmetrized wave-functions that we can write as

$$\Pi(\boldsymbol{R}) = \frac{1}{\sqrt{N!\prod_i n_i}} \sum_P (-1)^P \chi_{i_1}(\boldsymbol{r}_{P_1})\ldots\chi_{i_N}(\boldsymbol{r}_{P_N}),$$

where we sum over all possible permutations P of particles. The sum in the RHS term can also be written as a determinant, known as Slater determinant:

$$\begin{vmatrix} \chi_{i_1}(\boldsymbol{r}_1) & \chi_{i_2}(\boldsymbol{r}_1) & \ldots & \chi_{i_N}(\boldsymbol{r}_1) \\ \chi_{i_1}(\boldsymbol{r}_2) & \chi_{i_2}(\boldsymbol{r}_2) & \ldots & \chi_{i_N}(\boldsymbol{r}_2) \\ \vdots & \vdots & & \vdots \\ \chi_{i_1}(\boldsymbol{r}_N) & \chi_{i_2}(\boldsymbol{r}_N) & \ldots & \chi_{i_N}(\boldsymbol{r}_N) \end{vmatrix}.$$

Therefore, using this basis we can find the proper antisymmetrized wave function:

$$\Phi(\boldsymbol{R}) = \sum_{i_1,i_2,\ldots,i_N} \phi_{i_1}\phi_{i_2}\ldots\phi_{i_N}\Pi(\boldsymbol{R}). \tag{3.3}$$

At this point we can see that even in the best case scenario when only a single combination of states is occupied, such that the string $i_1,\ldots,i_N$ is fixed, there are still $N!$ terms coming from the permutations to be considered. Things get even worse when we try to compute averages of operators, which will be our final goal. The origin of this complication is that we are taking into account useless information, namely, the position of each particle in a certain state, while what we need to know is just the number of occupied states. This is where second quantization becomes very useful.

It is more convenient to express the state of a many-body system by specifying the occupation number n_i for every i-th possible state, namely, the number of particles occupying that state. The many-body state is defined by the occupation numbers for each possible state,

$$|\boldsymbol{N}\rangle = |n_1, n_2, \ldots\rangle$$

and it represents an anti-symmetrized state with n_1 particles in state $|\chi_1\rangle$, n_2 particles in state $|\chi_2\rangle$ and so on. For a fixed number of particles, $\sum_i n_i = N$ is a constraint in the Fock space. The set $\{|\boldsymbol{N}\rangle\}$ is an orthonormal basis for a subspace of the Fock space which, relaxing the condition of the total number of particles, is defined as

$$\mathcal{F} = \mathcal{H}_0 \oplus \mathcal{H}_1 \oplus \mathcal{H}_2 \ldots,$$

and contains all the possible anti-symmetrized many-body states [18].
We now define the creation and annihilation operators $c_i^\dagger$ and c_i that, for fermions, satisfy the following anti-commutation relations:

$$\{c_i, c_j\} = \{c_i^\dagger, c_j^\dagger\} = 0,$$
$$\{c_i, c_j^\dagger\} = \delta_{i,j}.$$

They can be used to verify that the Pauli exclusion principle holds. We also define the number operator $n_i = c_i^\dagger c_i$ which, given the above relations, can have eigenvalues 0 or 1 when acting on the one-body i-th orbital that is either empty $|0\rangle$ or occupied by a single fermion $|1\rangle$. It follows that the creation and annihilation operators act on the states in this way

$$c_i^\dagger|0\rangle = 1 \qquad c_i|0\rangle = 0$$
$$c_i^\dagger|1\rangle = 0 \qquad c_i|1\rangle = 0.$$

Finally, we can write a general basis state in terms of creation operators

$$|\boldsymbol{N}\rangle = \frac{(c_1)^{n_1}}{\sqrt{n_1!}}\frac{(c_2)^{n_2}}{\sqrt{n_2!}}\cdots\frac{(c_N)^{n_N}}{\sqrt{n_N!}}|\emptyset\rangle,$$

where $|\emptyset\rangle = |0,0,\cdots,0\rangle$ is the vacuum and $n_j = 0$ or 1, $j = 1,2,\cdots N$. The general many-body state is written as a combination of these basis states

$$|\Phi\rangle = \sum_{\boldsymbol{N}} c_{\boldsymbol{N}}|\boldsymbol{N}\rangle.$$

3.1.2 Solid-State Physics

A proper beginning of the study of SSP can be set with the discovery of X-ray diffraction in crystals in 1912 by Laue and his coworkers. At that point, the importance of crystal structures was understood: since electrons have short wavelength compared with the order of the regular periodic crystal structure that hosts them, they are dramatically subject to it and their properties can be understood in such a framework [19].

Crystals are defined as structures built by repeating identical groups of atoms, called *basis*, and attaching them on a set of points called *lattice*. More rigorously, a lattice is a mathematical set of points $\boldsymbol{r}$ which, in three dimensions, are constructed by taking the combination of some *translation vectors* $\boldsymbol{a}_1, \boldsymbol{a}_2, \boldsymbol{a}_3$,

$$\boldsymbol{r} = u_1\boldsymbol{a}_1 + u_2\boldsymbol{a}_2 + u_3\boldsymbol{a}_3,$$

where u_1, u_2 and u_3 are arbitrary integers. This set of vectors is said to be primitive if any point $\boldsymbol{r}$ of the lattice is reachable by constructing combinations of these vectors by integer coefficients. Moreover, they define a parallelepiped called *primitive cell*, which is the minimum volume unit cell that fills the space with a repetition of suitable crystal translation operations. The lattice is said to be *transationally invariant* in the sense that any translation $\boldsymbol{T}$

$$\boldsymbol{T} = u_1\boldsymbol{a}_1 + u_2\boldsymbol{a}_2 + u_3\boldsymbol{a}_3$$

maps the lattice into itself. The basis attached to the lattice can be an atom or a group of atoms, see Figure (3.1). The overall cohesion of atoms in the crystal is guaranteed by the interaction between the negative electronic charges of the atom and the positive charges of the neighbouring nuclei.

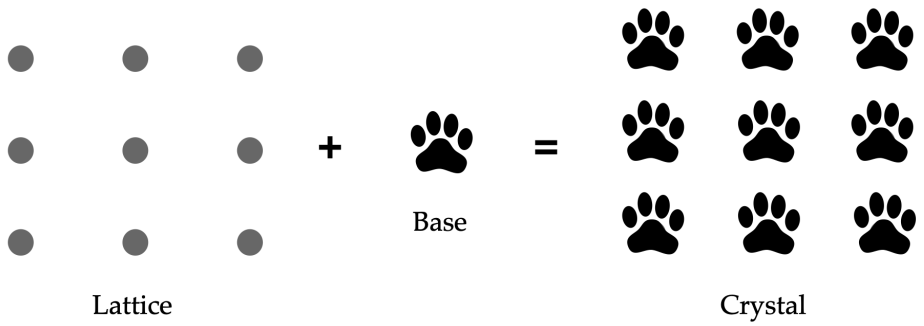

Figure 3.1: Representative example of a crystal: to each site on a lattice, a generic and purely illustrative basis is attached to form a crystal structure.

The periodicity of lattice structures allows the application of Fourier analysis. Let us consider a periodic function in one dimension, for example the electron number density,

$$n(x) = n(x + a),$$

where a is the unit cell in one dimension, and expand it in a Fourier series

$$n(x) = \sum_p n_p e^{i2\pi px/a},$$

where the sum runs over all integers p, and the coefficient $2\pi/a$ ensures the periodicity of the function. The points $2\pi p/a$, coefficients of the expansion, depict allowed terms in the Fourier series, i.e. terms consistent with the periodicity of the lattice, and form a lattice called *reciprocal lattice*. Generalizing to three dimensions, the electron density is expanded in series as:

$$n(\boldsymbol{r}) = \sum_{\boldsymbol{G}} n_{\boldsymbol{G}} e^{(i\boldsymbol{G}\cdot\boldsymbol{r})}$$

where the vectors in the reciprocal space $\boldsymbol{G}$ are to be found such that $n(\boldsymbol{r}) = n(\boldsymbol{r} + \boldsymbol{T})$. This condition leads to the restriction $e^{i\boldsymbol{G}\cdot\boldsymbol{T}} = 1$, which does not uniquely define the $\boldsymbol{G}$ vectors in the reciprocal space. An important concept in the reciprocal space is the so called *Brillouin zone*, defined as the Wigner-Seitz (WS) cell in reciprocal space. This WS is a particular type of primitive cell.

The quantum description of particles in a solid (electrons and nuclei) is given by the Schrödinger equation,

$$H\Phi = E\Phi,$$

where $H = K + U$ is a Hamiltonian that models the system, Φ is an eigenstate of this Hamiltonian and E is the eigenenergy. This model takes into account multiple terms: kinetic contributions from both electrons and nuclei contained in K, potential interactions between nuclei, between electrons and between nuclei-electrons pairs contained in U.

Because of the complexity of this framework, some approximations are adopted. One of them considers the electrons in the inner core to be part of the nuclei, forming an ion. This approximation is referred to as *valence approximation* and allows to only take into account valence electrons in the Hamiltonian. Another important approximation concerns the movement of the nuclei: due to the fact that the mass of the nuclei is much larger than the mass of electrons, electrons move faster than nuclei. We can thus consider the ions as fixed in the positions of the lattice. This approximation is called *Born-Oppenheimer approximation*. Finally, to simplify the many-body problem that stems from considering both one-electron potentials, describing nuclei-electrons interactions, and pair potentials, describing interactions between electrons, the *independent electron approximation* is usually made. In this context, the electrons are considered to be moving in an effective one-electron potential [20].

With these approximations, the Hamiltonian of the system becomes the sum of one-electron Hamiltonians h_i,

$$H = \sum_i h_i = \sum_i \left(-\frac{\hbar^2}{2m}\nabla_i^2 + \hat{U}_i(\boldsymbol{r}) \right), \tag{3.4}$$

each of which contains a kinetic term related to the motion of electrons and a potential term $\hat{U}(\boldsymbol{r})$ in which an effective potential for both electron-nucleus and electron-electron interaction is considered. The complex problem of solving the Hamiltonian of a solid has been reduced to the study of single electrons in a period potential. In fact, since the ions in the crystal are arranged in a regular fashion, the potential felt by the electrons is taken to have the same periodicity of

the underlying lattice,

$$\hat{U}(\boldsymbol{r}) = \hat{U}_i(\boldsymbol{r} + \boldsymbol{T}).$$

The solution to the many-electrons Hamiltonian H can be written as the product of single-electron wave-functions,

$$\Phi = \phi_1(\boldsymbol{r}_1)\phi_2(\boldsymbol{r}_2)\dots\phi_N(\boldsymbol{r}_N),$$

with N being the number of electrons.

We are now left with finding the solution to the motion of a single-electron in a periodic potential. To this aim, there is an important theorem in SSP which goes under the name of *Bloch's Theorem*, the statement of which is the following:

Theorem 3.1.1 (Bloch's theorem) *The solutions ϕ to the one-electron Schrödinger equation with periodic potential must be of a special form:*

$$\phi_{\boldsymbol{k}}(\boldsymbol{r}) = e^{i\boldsymbol{k}\cdot\boldsymbol{r}}u_{\boldsymbol{k}}(\boldsymbol{r}).$$

They are the product of a plane-wave $e^{i\boldsymbol{k}\cdot\boldsymbol{r}}$ times a function $u_{\boldsymbol{k}}(\boldsymbol{r})$ which has the same periodicity of the crystal lattice.

The theorem is a consequence of the translational symmetry: since the Hamiltonian and the generator of the translational group $\hat{T}$ commute, they can be simultaneously diagonalized, enforcing the appearance of a quantum number $\boldsymbol{k}$, which can be associated to a quantity $\hbar\boldsymbol{k}$ named *crystal momentum*. An important consequence of Bloch's theorem is that the functions $\phi_{\boldsymbol{k}}(\boldsymbol{r})$ are periodic in the reciprocal space, meaning that $\phi_{\boldsymbol{k}}(\boldsymbol{r}) = \phi_{\boldsymbol{k}+\boldsymbol{G}}(\boldsymbol{r})$ for any translation $\boldsymbol{G}$ in the reciprocal space. This allows to restrict the study of the wave-functions $\phi_{\boldsymbol{k}}$ to the vectors $\boldsymbol{k}$ belonging to the first Brillouin zone.

Due to the periodicity of Bloch's functions in $\boldsymbol{k}$, they can be expanded in Fourier series in the direct space

$$\phi_{\boldsymbol{k}}(\boldsymbol{r}) = \sum_j W_{\boldsymbol{R}_j}(\boldsymbol{r})e^{i\boldsymbol{k}\cdot\boldsymbol{R}_j}$$

by introducing a set of functions $W_{\boldsymbol{R}}(\boldsymbol{r})$ called *Wannier functions*, here $\boldsymbol{R}$ is any lattice vector in the direct space. These functions have the important property of being localized on lattice vectors $\boldsymbol{R}$ [21].

It is convenient to simplify this model even further, by making use of the *tight-binding approximation*. As illustrated in Figure (3.2), in a tight-binding approach, valence electron wave-functions are localized on the atoms and, thus, on lattice sites. This model is considered to be appropriate to describe the low-energy physics that we are interested in. Moreover, we assume that all the orbitals except for the lowest in energy, the s-band, are energetically unavailable. The localization property of Wainner functions makes them a good candidate to be used in this context: we introduce creation and annihilation operators, such that the former, $c^\dagger_{i\sigma}$, creates an electron with spin σ in a Wannier state localized at site i and the latter, $c_{i\sigma}$, destroys it.

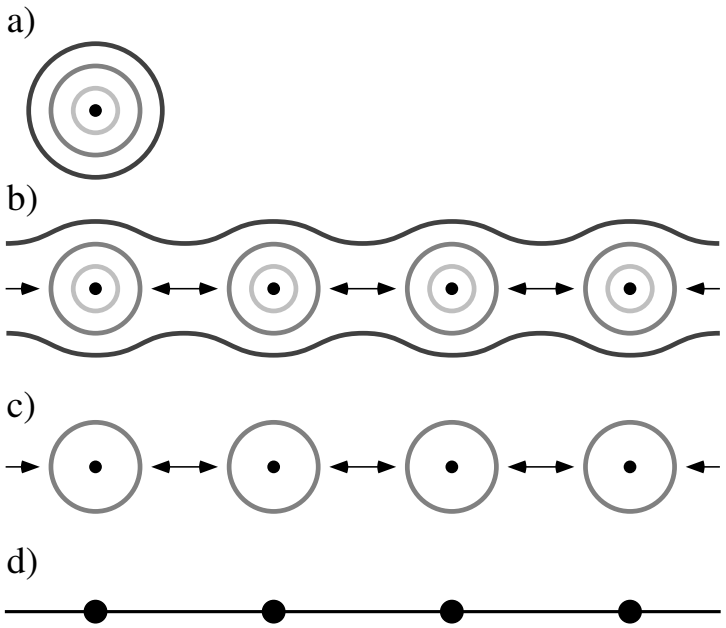

Figure 3.2: Schematic represenation of tight-binding approach [22]. (a) A single atom with its energy levels. (b) When atoms of this kind are put on a lattice structure, it can happen that external atomic orbitals overlap and hybridize, forming conducting bands (for example the black band if the figure) where electrons become itinerant. Electrons on these bands are not considered in a tight-binding approach. Rather, it focuses on electrons that are mostly localized on atomic sites, but have a non-negligible probability of tunnelling to neighbouring atoms, as depicted by the dark-gray energy level in (c). Schematically, this approach reduces to electrons positioned on lattice sites, shown in (d), with the ability of hopping to other sites.

At this point, we introduce a term in the Hamiltonian that reflects the essence of the Hubbard model: a pair-wise interaction V between electrons. With the addition of this interaction term, the Hamiltonian in equation (3.4) becomes

$$H = \sum_i \left(-\frac{\hbar^2}{2m}\nabla_i^2 + \hat{U}_i(\boldsymbol{r}) \right) + \sum_{i,j} V(\boldsymbol{r}_i, \boldsymbol{r}_j).$$

It is possible [23] to rewrite the Hamiltonian in terms of the Wannier creation and annihilation operators that we introduced, obtaining the Hamiltonian in second quantization

$$H = \sum_{ij}\sum_{\sigma} t_{ij} c_{i\sigma}^\dagger c_{j\sigma} + \sum_{ijmn}\sum_{\sigma\sigma'} v_{ijmn} c_{i\sigma}^\dagger c_{j\sigma'}^\dagger c_{n\sigma'} c_{m\sigma},$$

where i, j, m, n label sites and σ, σ' indicate the spin of the operators. The coefficients in the above expression are given by

$$t_{ij} = \int d\boldsymbol{r} W_{\boldsymbol{R}_i}^*(\boldsymbol{r}) \left[-\frac{\hbar^2}{2m}\nabla_i^2 + \hat{U}_i(\boldsymbol{r}) \right] W_{\boldsymbol{R}_j}(\boldsymbol{r})$$

$$v_{ijmn} = \int d\boldsymbol{r} \int d\boldsymbol{r}' W_{\boldsymbol{R}_i}^*(\boldsymbol{r}) W_{\boldsymbol{R}_j}^*(\boldsymbol{r}') V(\boldsymbol{r}, \boldsymbol{r}') W_{\boldsymbol{R}_m}(\boldsymbol{r}') W_{\boldsymbol{R}_n}(\boldsymbol{r})$$

The Wannier states are mostly localised on atomic sites, it is thus reasonable to assume only nearest neighbor interaction and, furthermore, we consider the parameter $t_{i,} = t$ to be site-independent. If the interaction parameters v_{ijmn} are negligible compared to the hopping parameter t, we obtain the tight-binding limit and the model can be treated with conventional band theory. The Hubbard Hamiltonian introduces non-negligible interaction to the picture. In particular, we will focus on on-site interactions $v_{ijmn} = v_{iiii}$. The parameter $v_{iiii} = U$ is assumed to be site independent. Hubbard made an estimate of the order of magnitude of the various matrix elements present in the Hamiltonian, which lead to the possibility of neglecting all the terms except for the on-site interaction U and the nearest neighbour hopping t. These final approximation leads to the Hubbard Hamiltonian in its simplest form:

$$H = \boxed{-t \sum_{\langle i,j \rangle} \sum_{\sigma} \left(c^{\dagger}_{i\sigma} c_{j\sigma} + h.c. \right)} + \boxed{U \sum_i c^{\dagger}_{i\uparrow} c_{i\uparrow} c^{\dagger}_{i\downarrow} c_{i\downarrow}}. \tag{3.5}$$

It is important to notice that the some of the arguments used to derive the Hubbard Hamiltonian are based on the periodicity of the lattice. As introduced in Section (2), the lattices we consider in this thesis are not periodic and, even if this feature enables the emergence of new interesting properties, Bloch theorem is not applicable. This problem was tackled in a recent study [24] in the context of quasicrystals. In a quasicrystal, the atoms are arranged in a pattern not regularly repeated, they are not periodic but have long-range order. In the study, a numerical method is introduced to generate the Wannier orbitals, required by the Hubbard Hamiltonian, without making use of the Bloch theorem. The authors argue that the external potential induced by such structure still has minima on the lattice sites, the depth of which is not the same for all sites. The resulting Hamiltonian has parameters t and U which are site dependent. However, for our lattice configurations, the distance between the nearest-neighbor sites is always the same, and there is no apparent reason for the potential, and thus the parameters, to be site dependent. Therefore, we are going to consider the Hamiltonian as originally derived in the context of SSP.

3.2 The Hubbard Hamiltonian

In this section, we describe the Hubbard Hamiltonian of equation (3.5) from a more phenomenological point of view. In the tight-binding approximation and with the s-orbital choice, each site can host four different type of states: one electron with spin-up, one electron with spin-down, no electrons or one spin-up and one spin-down electron,

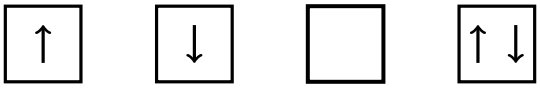

The behaviour of these electrons is governed by the Hamiltonian, which contains two terms: a kinetic term (gray box in Equation (3.5)) and a potential term (black box in Equation (3.5)).

The kinetic term describes the hopping of electrons to neighbouring sites $\langle i, j \rangle$, it destroys the electron on one site and creates it on the other. The energy scale of hopping is moderated by

the parameter t, sometimes referred to as *hopping parameter*, which, in turn, quantifies the overlap of the wave-functions of the pair of atoms. We approximate the electrons to only jump to neighbouring site and justify this assumption by considering that the wave-functions decay exponentially from the center of the atom, i.e. from the lattice site.

The potential term describes on site interaction between electrons with opposite spin on the same site. It originates from Coulomb interaction between electrons. Since this type of interaction is inversely proportional to the distance between electrons, we assume it to be 0 if the site is empty or has only one electron, while it equals U if the site has double occupancy. These two terms are schematically represented in the following picture:

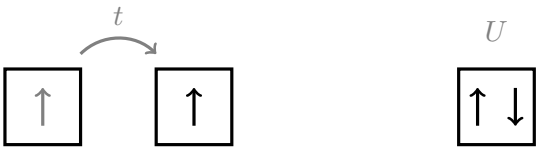

The Hubbard Hamiltonian is meaningful because it captures the interplay between two behaviours:

- electron hopping, consequence of the kinetic term, tends to delocalize the electrons, leading to a metallic behaviour,
- on-site electron interaction, which stems from the potential term, and favours the localization of electrons on sites. This term leads to insulating behaviour.

Finally, we list some symmetry properties of the system, which will play a determinant role in the next sections. The Hamiltonian is invariant under global $U(2)$ symmetry, which can be written as the direct product of the $U(1) \times SU(2)$ groups. The $U(1)$ element of this product satisfies the missing degree of freedom of the $SU(2)$ element by introducing a phase. The Gauge $U(1)$ symmetry leads to conservation of the charge and, hence, of the total number of particles. Moreover, we can also claim that the total number of particles with spin-up and spin-down is separately conserved, and it is immediate to see that this holds for both the kinetic and potential term in the Hamiltonian. In fact, the former simply moves electrons in the lattice without changing their number, while the latter commutes with the number operators $n_{i,\sigma} = c^{\dagger}_{i,\sigma} c_{i,\sigma}$.
The $SU(2)$ symmetry implies that H, $\mathbf{S}$ and S_z can be simultaneously diagonalized, and makes the system spin-rotational invariant C. Under specific conditions of the lattice, the system presents particle-hole symmetry (Appendix A) which will be useful to interpret some of our result in the next sections.

3.3 Quantum Phases of the Hubbard Model

Despite extensive analytical and numerical explorations, there are still unresolved questions regarding the properties of the Hubbard model, which is considered one of the fundamental models in quantum physics. Even at the mean-field level, the complete determination of its phase diagram and the comprehensive understanding of its ground state magnetic properties

are yet to be achieved. The scope of this section is to present some of the most meaningful results discovered after the introduction of the model, with a focus on systems related to the studies performed in this thesis.

One of the first achievements of the Hubbard model [25] was to explain the insulating nature of certain types of materials called *Mott insulators*, such as NiO, which are predicted to be conductors by band theory. In band theory, within the independent electron description, a material is considered metallic if the density of states at the Fermi level (defined as the thermodynamic work necessary to add one electron to the system) is non vanishing [26]. On the other hand, if the density of electrons in the Fermi level is null, the material must be an insulator. The insulating nature of Mott insulators derives instead from the strong Coulomb interaction between electrons. To make this concept clear, let us consider a half-filled band, a band with one electron per lattice site. The electrons are allowed to move on sites populated by another electron with opposite spin and the probability of this process depends on the strength of the interaction between electrons. In fact, if the interaction is small, electrons hop around the lattice leading to a metallic behaviour, while if the interaction is strong, they avoid moving from their positions, leading to an insulating behaviour [27].

Another established result regards the strong-interaction limit, where the Hubbard model can be mapped to the spin-$1/2$ antiferromagnetic Heisenberg Hamiltonian [28]. This result was obtained by perturbatively expanding the Hamiltonian in t/U, the first order of which vanishes, leading to the aforementioned result in second-order of perturbation. It is also known that in the translationally invariant case, there is long-range spin order for $d \geq 3$, d being the dimension of the lattice [29].

A great result was achieved in 1968 by Lieb and Wu, who solved the model exactly in one dimension (1d), using the extension of the "Bethe ansatz" technique [30]. However, even if the model in $1d$ is exactly solvable, the two dimensional $(2d)$ Hubbard model has become a focal point of research in condensed matter and quantum many-body physics, soon after the discovery of high-Tc cuprate superconductors. In fact, it was pointed out that the 2D Hubbard model might be an appropriate minimal model for high-Tc cuprates [31]. Moreover, $2d$ allows the choice of different lattice geometries, which can lead to the existence of new types of phases. One of such geometries is the triangular lattice, where geometrical frustration could lead to exotic phases. The model at $U = 0$ is exactly solvable. At half-filling it forms a metal, while at $U \to \infty$ it tends to the Heisenberg model with long-range antiferromagnetic spin order. There is a phase transition between the metallic and Mott-insulating regime, which has been found to be a non-magnetic insulating phase [15][3].

The studies on honeycomb types of lattices are also meaningful for our investigation, due to the similarity to the unfrustrated Sierpinski lattice that we consider. In contrast to the square lattice at half-filling, where the ground state of the system is found to be an antiferromagnetic insulator for every value of interaction strength $U > 0$ due to perfect nesting, the half-filled Hubbard

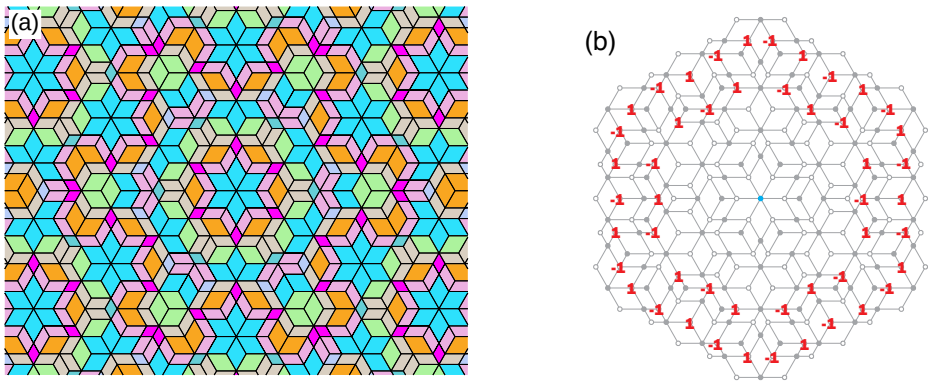

Figure 3.3: Figures from a recent study of the Hubbard model on the hexagonal golden-mean tiling [33]. In (a) the lattice, in (b) one of the confined states found in the tight-binding regime. 1 and -1 represent the amplitude of the wave-function on a particular site.

model on the honeycomb lattice undergoes a transition to the antiferromagnetic phase at a finite value of interaction. Using QMC simulations[32], it was found the ground-state of the system on this lattice was found to behave as a paramagnetic semi-metal in the small-U regime and antiferromagnetic at strong-U, identifying the transition at a critical value of $U_c/t \simeq 4.5$.

Since more has been established theoretically and numerically on the Hubbard Hamiltonian at half-filling, studies tend to focus on this particular regime. However, investigation of the model away from half-filling also revealed interesting physics. For example, doping the antiferromagnetic phase of the Hubbard Model on the square lattice revealed the presence of spin and density waves with different characters, at a mean-field level [13].

Finally, a study very relevant for this thesis, due to the aperiodicity of the related lattice, is related to the Hubbard model on an hexagonal golden-mean tiling [33], shown in Figure (3.3). The implementation of the Hubbard Hamiltonian reveled, at a tight-binding level, the existence of degenerate states with interesting spatial patterns. These states were found to be responsible for a ferrimagnetically ordered regime for weak-interaction. Stronger Coulomb interaction lifts this degeneracy, giving rise to a finite staggered and uniform magnetization.

4 | Tight-binding Model on a Fractal Lattice

As a first approach to the system, we consider the non-interacting Hubbard Hamiltonian, since we expect the connections among the sites on a fractal to affect mainly the hopping term of the Hamiltonian. After setting $U = 0$ in equation (3.5), we get the Hamiltonian in the tight-binding limit

$$H_{TB} = -t \sum_{\langle i,j \rangle \in \Lambda} \sum_{\sigma} \left(c^{\dagger}_{i\sigma} c_{j\sigma} + \text{h.c.} \right), \tag{4.1}$$

which physically represents electrons freely hopping around the lattice, without any energy cost for double occupation of lattice sites. Here, and for the rest of the work, we set open boundary conditions. Our aim is to find the ground-state energy and wave-function of this Hamiltonian, and study their properties.

Naively and driven by the simplicity of the form of the Hamiltonian, one could think of diagonalizing the Hamiltonian exactly and identifying the ground-state energy as the lowest energy eigenvalue and the ground-state wave-function as its corresponding eigenvector. To diagonalize the Hamiltonian, we first need to choose a basis and our convention for the basis choice is, in the Fock space, strings with $2 \times M$ entries that can take values of either 0 or 1 (1 means that there is an electron, 0 that there is not) and that identify the positions of the electrons on the lattice [34]. We also need to define an order: the first half of the entries represents spin up particles populating the numbered lattice sites, while the second represents spin down particles with the same lattice site ordering. For example, some basis vectors can have the form:

$$|\underbrace{1,0,\ldots,0}_{N_\uparrow},\underbrace{0,\ldots,0}_{N_\downarrow}\rangle \quad \longrightarrow \quad \text{One spin-up particle on site one}$$

$$|\underbrace{1,0,\ldots,0}_{N_\uparrow},\underbrace{1,\ldots,0}_{N_\downarrow}\rangle \quad \longrightarrow \quad \text{One spin-up and one spin-down particle on site one.}$$

For now, it is not important to have in mind a specific ordering of the lattice sites, we will specify it later in this section.

The number of such basis states depends on the number of particles we consider: if we choose $N_\uparrow$ spin-up particles and $N_\downarrow$ spin-down particles, the number of basis states coincides with the

number of possible ways we can distribute $N_\uparrow$ indistinguishable spin-up electrons on M sites and, similarly for the spin-down electrons, obtaining a number of

$$\binom{M}{N_\uparrow}\binom{M}{N_\downarrow}$$

basis states for a specific configuration of $N_\uparrow$ and $N_\downarrow$ electrons. Summing over the possible number of spin-up and -down electrons, which goes from zero to the number of sites, we get the total number of basis states

$$\sum_{N_\uparrow=0}^{M}\sum_{N_\downarrow=0}^{M}\binom{M}{N_\uparrow}\binom{M}{N_\downarrow} = 4^M.$$

Since this number grows exponentially with the number of sites, exact diagonalization is a computationally demanding method to solve the Hamiltonian and we need to follow a different approach in order to be able to study large-size systems.

As better detailed in the next section, we are going to make use of some properties of the many-body Salter Determinant to compute interesting expectation values of the ground-state, such as ground-state energy and average electron density per lattice site.

4.1 Slater Determinant space

In this section, we are going to develop the formalism behind the implementation of our model [35]. The idea behind the method is that, in the framework of the second quantization and tight-binding approach, one builds the possible single-particle orbitals as superpositions of single-site wave-functions. These orbitals, in turn, are used as basis of the N-particle Fock space where we are able to construct anti-symmetrized many-body wave-functions making use of Slater determinants.

Let us consider a single particle with M possible states, which can be seen as the M lattice sites in the context of the Hubbard model. The basis in the Fock space with $N = 1$ is made of states denoted by $|\chi_i\rangle$, which represent the single particle in the $i-$th state with $i = 1, \ldots, M$. These states can also be written in terms of their relative creation operators $c_i^\dagger$ acting on the null vector as $\chi_i = c_i^\dagger |0\rangle$.

A general-single particle state $|\phi\rangle$ can be written as a linear combination of the single-particle basis states

$$|\phi\rangle = \sum_{i=1}^{M} \phi_i |\chi_i\rangle ,$$

from which it is clear that, given the chosen basis, the single-particle state is uniquely deter-

mined by the coefficients

$$\begin{pmatrix} \phi_1 \\ \phi_2 \\ \vdots \\ \phi_M \end{pmatrix}.$$

We are going to denote by $\hat{\phi}^\dagger$ the creation operator that, acting on the null vector, generates $|\phi\rangle$.

In order to find the total N-particle state, we need to take anti-symmetrised linear combinations of the single-particle states

$$|\Phi\rangle = \hat{\phi}^\dagger{}_1 \hat{\phi}^\dagger{}_2 \dots \hat{\phi}^\dagger{}_N |0\rangle ,$$

which is referred to as a Slater determinant since its first-quantized counterpart (**??**) involves the computation of a determinant. This many-body is represented by the following matrix:

$$\Phi = \begin{pmatrix} \phi_{1,1} & \phi_{2,1} & \dots & \phi_{N,1} \\ \phi_{1,2} & \phi_{2,2} & \dots & \phi_{N,1} \\ \vdots & \vdots & & \vdots \\ \phi_{1,M} & \phi_{2,M} & \dots & \phi_{N,M} \end{pmatrix}.$$

and we will refer to this also, for brevity, as a Slater determinant. In fact, the determinant of this matrix corresponds to the Slater determinant introduced in first quatization where, instead of considering the coefficients as entries of the matrix we considered the orbitals.

The Slater determinants we introduced satisfy some useful properties:

- The product of two Slater determinants $|\Phi\rangle$ and $|\Phi'\rangle$ satisfies $\langle\Phi|\Phi'\rangle = \det(\Phi^\dagger \Phi')$.
- The action of an operator of the form $\hat{B} = \exp\left(\sum_{i,j}^{M} c_i^\dagger U_{i,j} c_j\right)$ on a Slater determinant $|\Phi\rangle$ yields another Slater determinant

  $$\hat{B}|\Phi\rangle = |\Phi'\rangle \quad \text{with} \quad \hat{\phi}'^\dagger_m = \sum_j c_j^\dagger \Phi'_{jm} \quad \text{and} \quad |\Phi'\rangle = e^U |\Phi\rangle .$$

  This is also known as the *Thouless Theorem*.
- We can write the total state $|\Phi\rangle$ as the tensor product of the states in the spin up and spin down sector

  $$|\phi\rangle = |\phi_\uparrow\rangle \otimes |\phi_\downarrow\rangle$$

  or, in matrix representation:

  $$\Phi = \Phi^\uparrow \otimes \Phi^\downarrow.$$

Using these properties, we can relate the Slater Determinant to physical quantities through the following identity

$$\langle c^\dagger_{j,\sigma} c_{i,\sigma}\rangle = \frac{\langle\Phi|c^\dagger_{j,\sigma} c_{i,\sigma}|\Phi\rangle}{\langle\Phi|\Phi\rangle} = \left[\Phi^\sigma[(\Phi^\sigma)^\dagger \Phi^\sigma]^{-1}(\Phi^\sigma)^\dagger\right]_{i,j} = G^\sigma_{ij}, \tag{4.2}$$

the validity of which is shown in Appendix (B).

The average density of electrons per lattice site $\langle n_i \rangle$ is given by the sum of the density of spin-up $\langle c^\dagger_{i,\uparrow} c_{i,\uparrow} \rangle = \langle n_{i,\uparrow} \rangle$ and spin-down $\langle c^\dagger_{i,\downarrow} c_{i,\downarrow} \rangle = \langle n_{i,\downarrow} \rangle$ electrons

$$\langle n_i \rangle = \langle n_{i,\uparrow} \rangle + \langle n_{i,\downarrow} \rangle = \langle c^\dagger_{i,\uparrow} c_{i,\uparrow} \rangle + \langle c^\dagger_{i,\downarrow} c_{i,\downarrow} \rangle = G^\uparrow_{ii} + G^\downarrow_{ii}. \tag{4.3}$$

The total energy corresponds to the expectation value of the Hamiltonian in the many-body wave-function

$$E_T = \langle H_F \rangle = -t \sum_{\langle i,j \rangle \in \Lambda} \sum_\sigma \left(\langle c^\dagger_{i\sigma} c_{j\sigma} \rangle + \langle c^\dagger_{j\sigma} c_{i\sigma} \rangle \right) = -t \sum_{\langle i,j \rangle \in \Lambda} \sum_\sigma \left(G^\sigma_{ji} + G^\sigma_{ij} \right). \tag{4.4}$$

4.1.1 Implementation

We implemented the tight-binding Hubbard Hamiltonian (4.1) in MATLAB with the aim of studying its ground-state properties. The implementation method is based on the idea of relating physical properties to the matrices G that we introduced in the previous section: the first part of the code deals with generating the matrices and the second with using them to compute interesting quantities. In this section, we are going to give more details on the implementation method.

Looking at equation (4.2), we realize that generating the desired matrix G requires the computation of the Slater determinants Φ. These are matrices built by vertically casting single-particle solutions of the tight-binding Hubbard Hamiltonian, which can be divided into the sum of the Hamiltonian that describes the hopping of up and down electrons: these two Hamiltonians are identical and independent of each other. Therefore, we can simplify the problem and diagonalize the Hamiltonian as if we had only spin-up or down, this is a $N \times N$ matrix. After obtaining the single-particle eignevalues and eigenvectors, we build the Slater determinant $\Phi^\uparrow$ by casting the $N_\uparrow$ eigenvectors corresponding to the lowest $N_\uparrow$ eigenvalues. The same is done for $\Phi^\downarrow$. These Slater determinants can be used to compute $G^\uparrow$ and $G^\downarrow$ which, in turn, yield the desired expectation values when plugged in the expressions in equations (4.3) and (4.4). By employing this method, we are able to reduce the computational demand when considering large systems: exact-diagonalization scales exponentially with the size of the system while the implementation just introduced scales algebraically.

In the next sections, we study the density of electrons per lattice site and the many-body ground-state energy, computed as in equation (4.3) and (4.4), for different values of electronic filling and for different generation of the fractal lattice. We do this with the aim of understanding how the geometry of the lattices influences the way the electrons distribute and the energy spectrum. In fact, the kinetic part of the Hubbard Hamiltonian contains information about the structure of the lattice: each element of the Hamiltonian matrix corresponds to a link between two sites and its value determines the possibility and the amplitude of the hopping between them.

4.2 First generation of the fractal lattice

Let us start considering the first generation of the fractal lattice, which has 9 lattice sites and is shown in Figure 4.1(a). Figure 4.1(b) shows the ground-state energy for different values of electron filling, keeping them balanced $N_\uparrow = N_\downarrow = N_\sigma$.

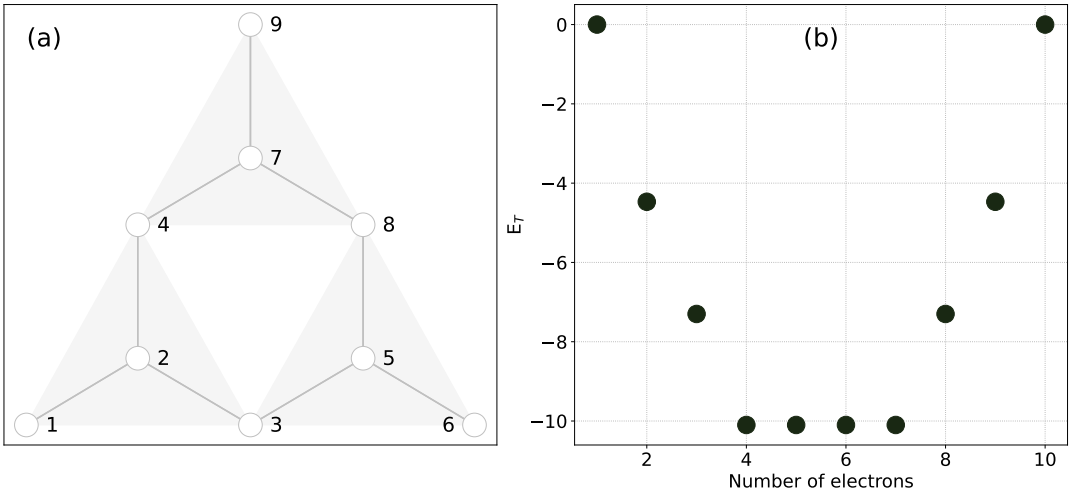

Figure 4.1: (a) First generation of the fractal lattice and (b) its corresponding many-body ground-state energy for different values of N_σ. The x axis in (b) indicates the number of electrons of one kind σ, the total number of electrons in the system is $2N_\sigma$.

We consider the average density per lattice site, which is found by computing the quantity derived in equation (4.3) for each lattice site. Then, we examine the configurations as we increase the number of electrons that populate the system, again keeping the total number of up and down electrons equal.

In Figure 4.2(a), we show the density distribution when the system is populated with one spin-up and one spin-down electron $N_\sigma = 1$. Notice that the sites with higher connectivity, i.e. the three sites with three neighbours at the centre of the triangles, have a higher density. We can understand this behaviour by taking into account the fact that hopping is energetically favourable, so in the ground-state it is preferable to store electrons in sites where they have more probability to hop. Along this logic, the sites with connectivity 2 are less populated, followed by the sites at the corners, which are connected to the lattice just through one link. If we increase the number of electrons and place $N_\sigma = 3$ electrons, the Pauli exclusion principle starts to play a role, meaning that two electrons with same spin can not occupy the same lattice site. The electrons do not have a choice but to be placed on sites kinetically less favourable, if the most favourable are already occupied. In Figure 4.2(b) we observe that, for example, the corner sites are populated.

When we exceed half-filling, i.e. the case where the total number of electrons coincides with the number of sites, the pattern is inverted: the three corners are then more populated, followed by the sites with connectivity 2 and finally the sites with connectivity 3, as shown in Figure 4.2(c). It seems energetically more favourable to store electrons in the corners and let the ones in the

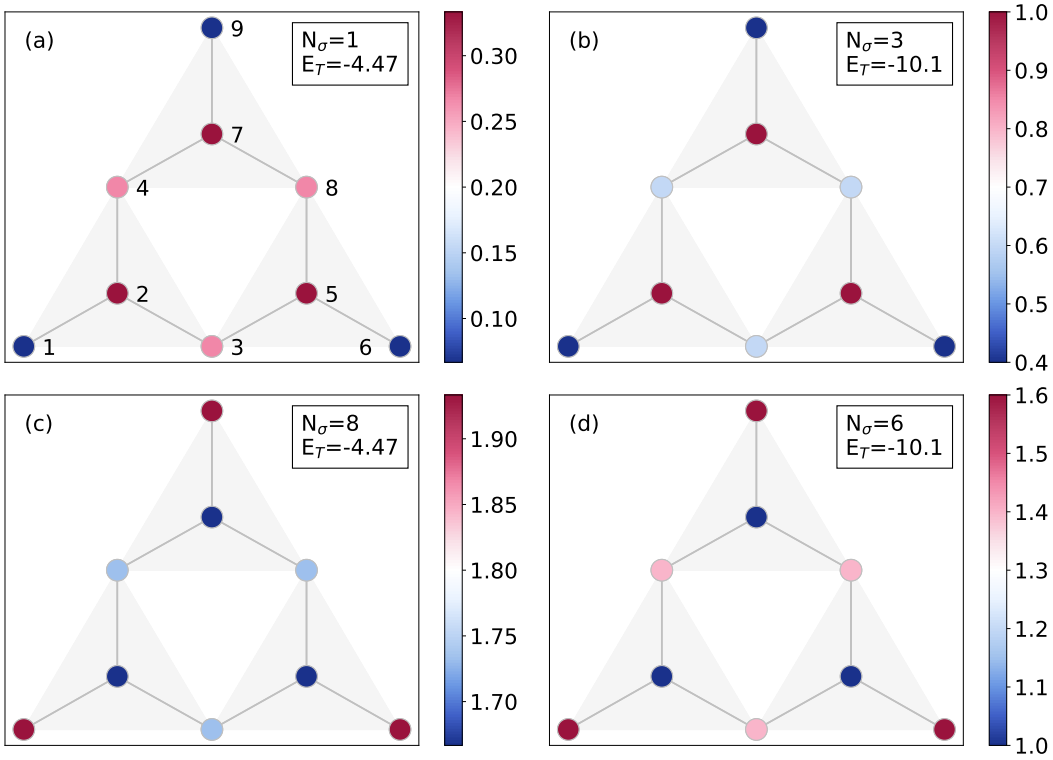

Figure 4.2: Average density configuration of the tight-binding ground-state on the first generation of the fractal lattice with filling (a) $N_\sigma = 1$, (b) $N_\sigma = 3$, (c) $N_\sigma = 8$ and (d) $N_\sigma = 6$.

bulk hop. Configurations above half filling follow this patter, as we can see if we look at the configuration with $N_\sigma = 8$ in Figure 4.2(c).

The behaviour of the system can be explained in terms of particle-hole symmetry. In fact, the tight-binding Hubbard Hamiltonian on the fractal lattice is particle-hole symmetric, as we can see by setting $U = 0$ in equation (A.2). This explains the symmetry of the energy spectrum around half-filling in Figure (4.1). Regarding the average density per site, from the equality of the Hamiltonians, it follows that the density configuration obtained by placing $N_\sigma = 1$ particles in an empty lattice is the same density configuration obtained by placing $\overline{N}_\sigma = 1$ holes in a fully-filled lattice, which corresponds to $N_\sigma = 8$. Therefore, recalling that

$$n_i = 2 - \overline{n}_i$$

we get the density configuration of particles in $N_\sigma = 8$ by subtracting the density corresponding to $N_\sigma = 1$ from 2. The same reasoning applies to configurations $N_\sigma = 3$ and $N_\sigma = 6$. We also notice that the symmetry is manifest in the dependence of the total many-body energy as a function of electronic filling, Figure 4.1(b). Moreover, in this figure we observe the presence of a degenerate level around half-filling.

The sites on the lattice can be categorized and grouped depending on their connectivity and position in the lattice. We expect sites belonging to the same group to have the same density. In

the density configurations shown in Figure (4.2), this property holds. Let us look, for example, the configuration with $N_\sigma = 1$: the first group of sites with identical geometrical property is constituted by sites $2, 5$ and 7, the second group is made of sites $4, 8$ and 3, finally the third group has sites $1, 6$ and 9. This behaviour can be seen as a consequence of the rotational symmetry of 120 degrees and, therefore, we expect it to be satisfied for any value of N_σ. However, we observed that some of the configurations from our implementation do not respect this property, as it is shown in Figure (4.4) for the case $N_\sigma = 2$. The reason behind this behaviour is that the filling does not close the degenerate energy level to which the higher-energy single-particle wave-functions belong to. In the next section, we study the single-particle problem and we will be able to make this statement clearer.

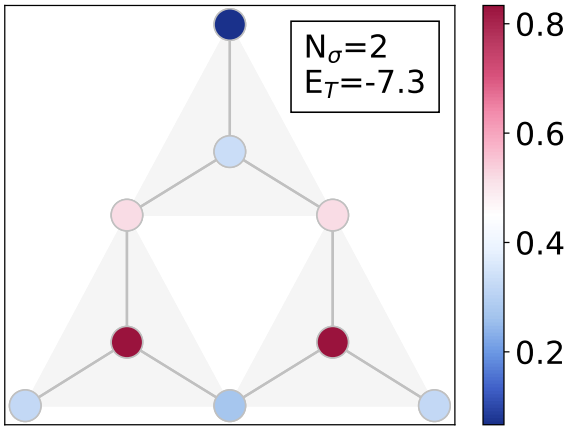

Figure 4.3: Average density configuration of the tight-binding ground-state on the first generation of the fractal lattice with filling $N_\sigma = 2$.

4.2.1 Spectral Analysis

In order to understand more in detail the behaviour of the system, we must determine the eigenvalues and eigenvectors of the single-particle Hamiltonian which, in turn, are used in the Slater determinant to construct the many-body wave-function and, therefore, responsible for the many-body properties. The first generation of the Sierpinski lattice has 9 sites. Recalling that spin-up and down are decoupled and can be treated independently, the Hamiltonian is a 9×9 symmetric matrix, has 9 real eigenvalues and corresponding eigenvectors.

Before proceeding with the study of the degeneracies, it is convenient to give an interpretation to the tight-binding Hamiltonian as the adjacency matrix of a graph. In graph theory, a graph is a set of vertices $\{u_1, \dots u_n\}$ linked between each other. It can also be characterised by a $n \times n$ matrix $\mathcal{A}$, called *adjacency matrix*, whose elements $\mathcal{A}_{ij}$ describe the connection between the sites u_i and u_j: if the element is zero the vertices are not connected; if it is different than zero, the vertices are connected and its value quantifies the weight of the connection. In our case, the

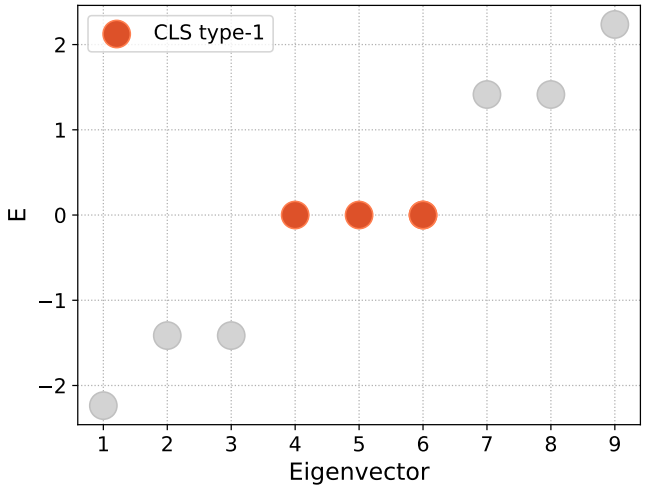

Figure 4.4: Spectrum of the single-particle tight-binding Hamiltonian for the first generation of the Sierpinski lattice. The spectrum shows different energy levels: three-fold degenerate level that we call CLS type-1 (the reason will be explained in this section) at zero energy, two two-fold degenerate levels at $E = \pm\sqrt{2}$ and two non-degenerate levels.

tight-binding Hamiltonian in equation (4.1) can be seen as the adjacency matrix of the graph in Figure 4.1(a), where the weight of the links between connected sites is $-t$,

$$\begin{pmatrix} 0 & -t & 0 & 0 & 0 & 0 & 0 & 0 & 0 \\ -t & 0 & -t & -t & 0 & 0 & 0 & 0 & 0 \\ 0 & -t & 0 & 0 & -t & 0 & 0 & 0 & 0 \\ 0 & -t & 0 & 0 & 0 & 0 & -t & 0 & 0 \\ 0 & 0 & -t & 0 & 0 & -t & 0 & -t & 0 \\ 0 & 0 & 0 & 0 & -t & 0 & 0 & 0 & 0 \\ 0 & 0 & 0 & -t & 0 & 0 & 0 & -t & -t \\ 0 & 0 & 0 & 0 & -t & 0 & -t & 0 & 0 \\ 0 & 0 & 0 & 0 & 0 & 0 & -t & 0 & 0 \end{pmatrix}.$$

Moreover, we can interpret the action of the Hamiltonian on a state as *walks* on the graph. For instance, let us consider a particular state χ, which in our formalism is a 9-elements vector. The ith element can be associated to the probability amplitude for the state to be on the ith site. The state we choose has an amplitude 1 of being on site 1. Acting with the Hamiltonian on the state

generates another state χ'

$$|\chi\rangle = \begin{pmatrix} 1 \\ 0 \\ 0 \\ 0 \\ 0 \\ 0 \\ 0 \\ 0 \\ 0 \\ 0 \end{pmatrix} \quad \longrightarrow \quad |\chi'\rangle = -t \begin{pmatrix} 0 \\ 1 \\ 0 \\ 0 \\ 0 \\ 0 \\ 0 \\ 0 \\ 0 \\ 0, \end{pmatrix}$$

which has been moved to site 2 with amplitude $-t$. The Hamiltonian walks the states on the graph according to its links and its weights.

With these insights from graph theory, we are now ready to investigate the spectrum of the Hamiltonian looking at the eigenstates and starting from the three-fold degenerate level at zero energy. In this analysis, we set the hopping parameter to be $t = 1$. In Figure (4.5), we show a pictorial representation of the states on the lattice with their amplitude and parity.

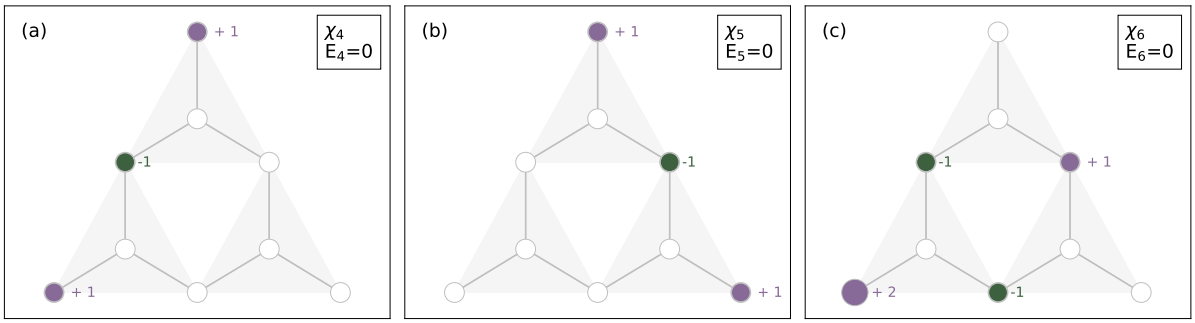

Figure 4.5: Amplitude scaled to unity of the three eigenvectors in the the zero-energy level of the tight-binding Hamiltonian, in (a) χ_4, in (b) χ_5 and in (c) χ_6. Dark-green and purple dots on the lattice represent, respectively, negative and positive amplitude of the wave-function on the sites. On sites where there are white dots, the amplitude is zero.

An interesting behaviour becomes evident: the amplitudes on sites that belong to the sub-lattice in the center of the triangles are zero. This is a consequence of the fact that the amplitudes of their neighbouring sites sum up to zero. We are going to refer to this type of behaviour as *destructive interference*. It is not possible to walk these $+1$ and -1 states on the lattice applying the Hamiltonian because these sites are connected to sites on the lattice where destructive interference takes place. Therefore, these states are referred to as *compact-localized states* (CLS), since they are localized on a specific set of sites in the lattice and their amplitude on the rest of the sites is exactly zero.

Moreover, from these eigenvectors we can deduce the emergence of corner modes after half-filling. First, we are going to select, in the degenerate space of eigenvectors, three convenient linearly-independent eigenvectors that are generators in the degenerate space. This means that from the linear combination of these eignevectors, we should be able to construct every state in the degenerate space. Being aware that these zero-energy states occupy the sub-lattice in the corners of the triangle, and inspired by the three-fold rotational symmetry of 120 degrees, we can substitute eigenvector χ_6 with a new eigenvector χ_6', obtained by rotating χ_5 and χ_4 of 120 degrees, the former clockwise and the latter counterclockwise. We obtain the set of eigenvectors shown in Figure (4.6) which, even-though non-orthogonal, span the degenerate space.

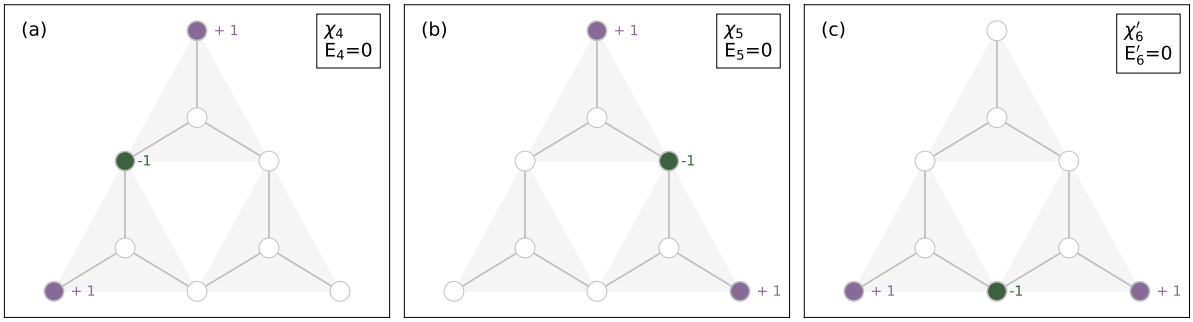

Figure 4.6: Amplitude scaled to unity of the three basis eigenvectors in the zero-energy level of the tight-binding Hamiltonian, in (a) χ_4, in (b) χ_5 and in (c) χ_6' obtained by rotating one of the other eigenvectors. Dark-green and purple dots on the lattice represent, respectively, negative and positive amplitude of the wave-function on the sites. On sites where there are no dots, the amplitude is zero.

Since the eigenstates in the zero-energy degenerate space are linear combinations of these three basis states, we can understand why these states contribute more to the amplitude in the corners: they share the corners, where amplitudes can add up. We can see this happening in eigenstate χ_6 in the first set of eigenstates in Figure (4.6). This can be written as

$$|\chi_6\rangle = |\chi_4\rangle + |\chi_6'\rangle - |\chi_5\rangle$$

and we notice that the site in the corner number 1 has at least double the modulus of the amplitude of the rest of the lattice sites. A possible final configuration is then obtained by summing up $\chi_4 + \chi_5 + \chi_6'$, leading to the wave-function shown in Figure (4.7).

We are now going to consider the states in the two-fold degenerate energy levels. Unlike the degeneracies corresponding to the zero level, which are due to destructive interference, these states originate from symmetries of the system. It is quite straightforward to understand how symmetries and degeneracies are connected. Consider a transformation T that is a symmetry of the system, and thus commutes with the Hamiltonian. If $|\chi\rangle$ is an eigenvector of the Hamiltonian,

$$H\,|\chi\rangle = \chi\,|\chi\rangle\,,$$

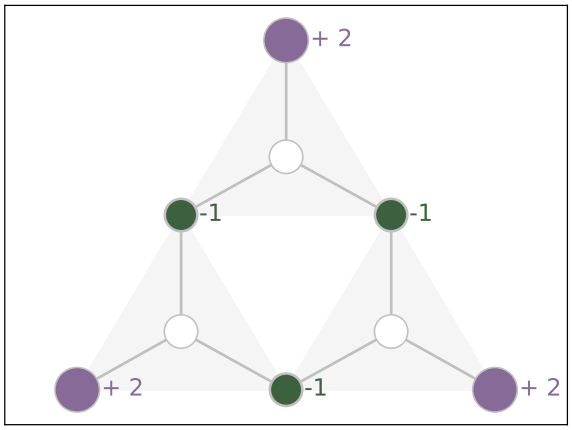

Figure 4.7: Wave-function with great contribution to the corners, obtained by summing the basis of the zero-energy degenerate eigenvectors $\chi_4 + \chi_5 + \chi_6'$.

all the states obtained by applying a transformation T are eigenvectors corresponding to the same eigenvalue

$$H\left(T\left|\chi\right\rangle\right) = TH\left|\chi\right\rangle = \chi\left(T\left|\chi\right\rangle\right).$$

If there is a finite number of such transformations, i.e. the transformations form a group with finite order, then we can argue that there are possibly as many degenerate states. Actually, the number of degenerate states coincides with the dimension of the irreducible representation of the group [36].

The symmetries of our system belong to the C_{3v} point-symmetry group, which has order 6 and the symmetries operations are:

- E identity: leaves the coordinates unchanged,
- C_3 and C_3^2 rotations: rotates the coordinates by an angle of $2\pi/3$ counter-clockwise,
- σ_1, σ_2 and σ_3 reflections: reflection of the coordinated with respect to the planes 1, 2 and 3 in Figure (4.8).

The dimension of the irreducible representations of C_{3v} is 2 and this explains the two-fold degeneracy of these states. In Figure (4.9), we can see the eigenvectors corresponding to the two-fold negative energy level. They make evident the symmetry with respect to two of the possible reflection axis. In order to intuitively check that this is an eigenstate of the Hamiltonian with energy $-\sqrt{2}$, we observe that computing each element of the vector $H\left|\chi\right\rangle$ simply consists in summing the amplitudes of neighbouring sites and multiplying by -1. Following this logic, it is plausible that in the ground-state larger amplitudes are placed in sites with more connectivity, explaining why the sites in center of the triangles are more populated in these degenerate levels.

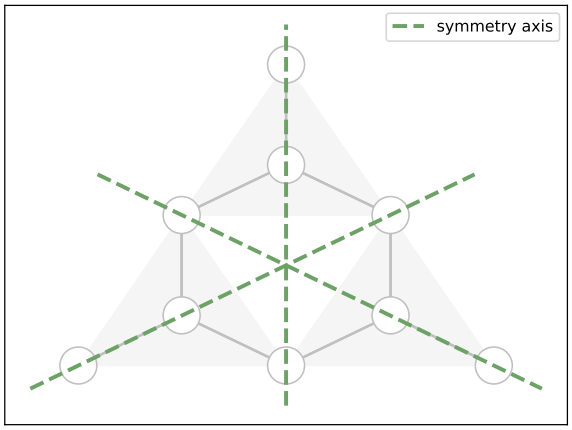

Figure 4.8: Pictorial representation of the three reflection-symmetry axis (lines in green) of the Sierpinski triangle σ_1, σ_2 and σ_3.

In Figure 4.9(b) and Figure 4.9(c), we observe the eigenvectors corresponding to the positive energy level. The pattern is similar to the negative energy states, and the opposite energy derives from casting amplitudes with opposite parity in the centre and in the corners of the populated sub-triangles.

From the study of the eigenvectors, we can conclude that it is in accordance with what we observed in the behaviour of the density configurations for increasing number of electrons: when considering lower energy eigenvalues, the sites in the center get populated, followed by the corners and finally again by the sites in the centre until filling up the whole lattice. The energy spectrum of the many-body configurations can be reconnected to the energy levels: the configurations have negative many-body energy below half-filling, followed by a region where the energy does not change (we are filling the system with zero-energy degenerate CLS), and finally the positive-energy eigenstates arise when increasing the filling, bringing the final many-body energy back to the initial value. Moreover, it is now possible to explain the wrong behaviour of the density configurations for certain values of electronic filling: if the filling corresponds to an eigenstate that does not close a degenerate energy-level, the code could select states found by taking arbitrary combinations of the eigenvector basis, spoiling the symmetry properties that we observe in other configurations. We indeed find that the issue emerges in configurations with filling $N_\sigma = 2, 4, 5, 7$. This random choice of eigenvectors in the level disappears when the filling closes the degenerate energy level.

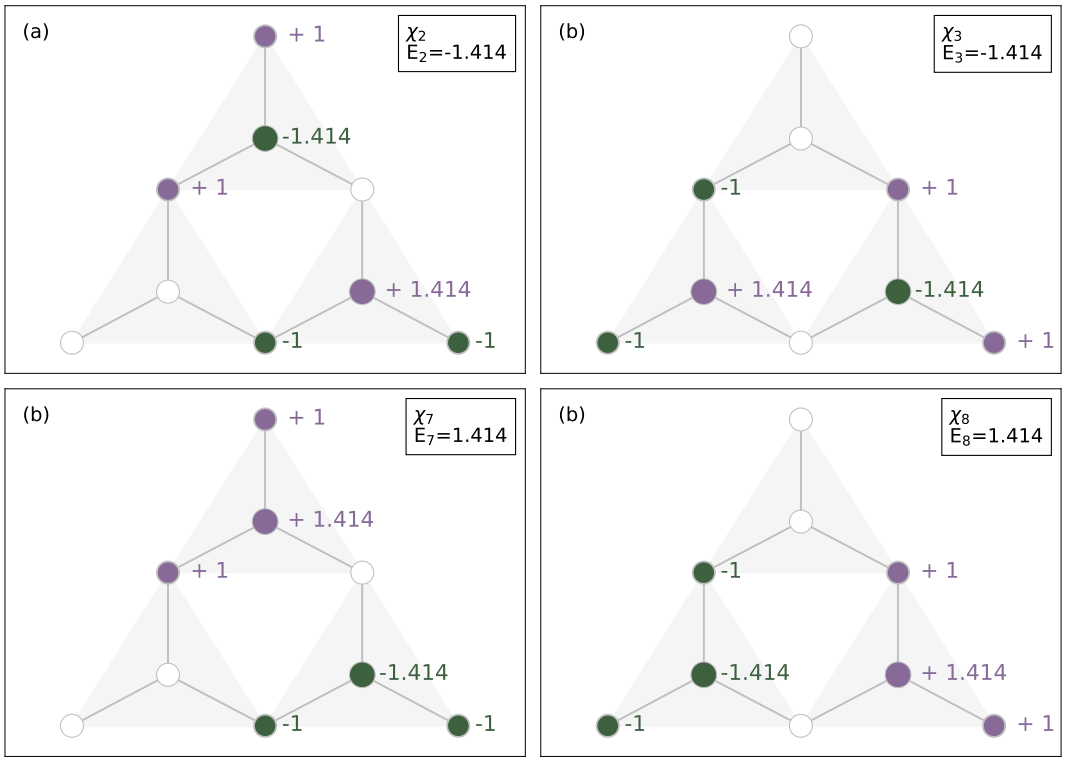

Figure 4.9: Eigenvectors (a) χ_3 and (b) χ_4 corresponding to the two-fold degenerate eigenvalues with energy $E = -\sqrt{2}$, eigenvectors (c) χ_7 and (b) χ_8 belonging to the two-fold degenerate level with energy $E = \sqrt{2}$.

4.3 Second generation of the fractal lattice

Given the self-similarity of the fractal structure that we consider, we expect to observe a similar behaviour for higher generations of the Sierpinski triangle. Let us consider, for example, the second generation. We represent in Figure (4.10) both the lattice with our enumeration convention and the energy dependence of the many-body ground-state on the electronic fillings. Now, there are 24 sites in the system. As expected, we observe a similar behaviour in the energy level distribution: it is symmetric around half-filling, where the energy is zero and other degenerate states are present. What changes is the number of such degenerate states, that will be explained in this section again through spectral analysis.

Before considering the single-particle contributions, let us observe some density configurations. In Figure 4.11(a) and Figure 4.11(b), we show the average density for with $N_\sigma = 3$ and $N_\sigma = 21$. First, notice that the particle-hole symmetry is still present, as expected: one places particles in a lattice of holes the same way as one places holes in a lattice of particles. From the behaviour in Figure 4.11(a), one can argue that it is energetically favourable for the electrons to not only be on sites with more connectivity, as we saw for the first generation, but also on sites placed in the inner part of the structure. The reason for this to happen is that hopping is energetically convenient; hence it is natural that positions where this is more probable are preferred.

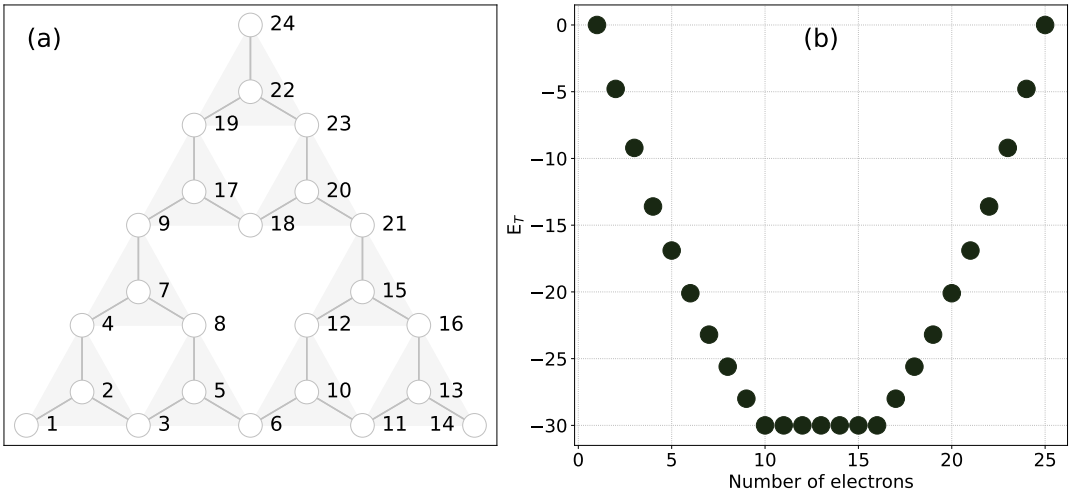

Figure 4.10: (a) Second generation of the fractal lattice and (b) its corresponding many-body ground-state energy for different values of N_σ. The x axis in (b) indicates the number of electrons of one kind σ, the total number of electrons in the system is $2N_\sigma$.

In order to investigate what happens in the zero-energy band around half-filling, we present the first and last density configuration states in the band, which are the configurations with $N_\sigma = 9$ and $N_\sigma = 15$ in Figure 4.11(c) and Figure 4.11(d) respectively. Comparing configuration $N_\sigma = 9$ with configuration $N_\sigma = 3$, we see that as the number of electrons is increased, the sites with more connectivity in the outer regions become populated, as a consequence of the Pauli exclusion principle.

We now compare configuration $N_\sigma = 9$ with $N_\sigma = 15$ to understand the consequence of the zero-energy states populating the system. In order to do so, we divide the lattice sites in groups of sites that undergo the same change: we will call *corners* the sites $1, 14, 24$ at the three corners of the lattice, *center* refers to the sites at the center of the triangles, *connection* stands for the sites $6, 9, 21$ that connect the three 1st generation triangles and *inner connection* labels the remaining sites that connect the three smallest triangles in each of the 1st generation triangles, for example sites $3, 4, 8$. Figure (4.12) shows how the density changes from configuration $N_\sigma = 9$ to $N_\sigma = 15$ and compares their rate of increase. First, we notice that all curves intercept at unity the density in the centre sites, which is consistent with the fact that at half-filling $N_\sigma = 12$, we expect the average density to be one on every site. Since the density on the centre sites does not change from configuration $N_\sigma = 9$ and $N_\sigma = 15$, we expect the destructive interference to take place at a single-particle level on those sites also in this generation. Then, we notice that the corners are the sites where the density increases the most, followed by the inner connections and finally by the connection between the smallest triangles. In order to be able to explain this behaviour, as well as the number of zero-energy degenerate states, we are now going to solve the tight-binding Hamiltonian at a single-particle level, as we did for the first generation.

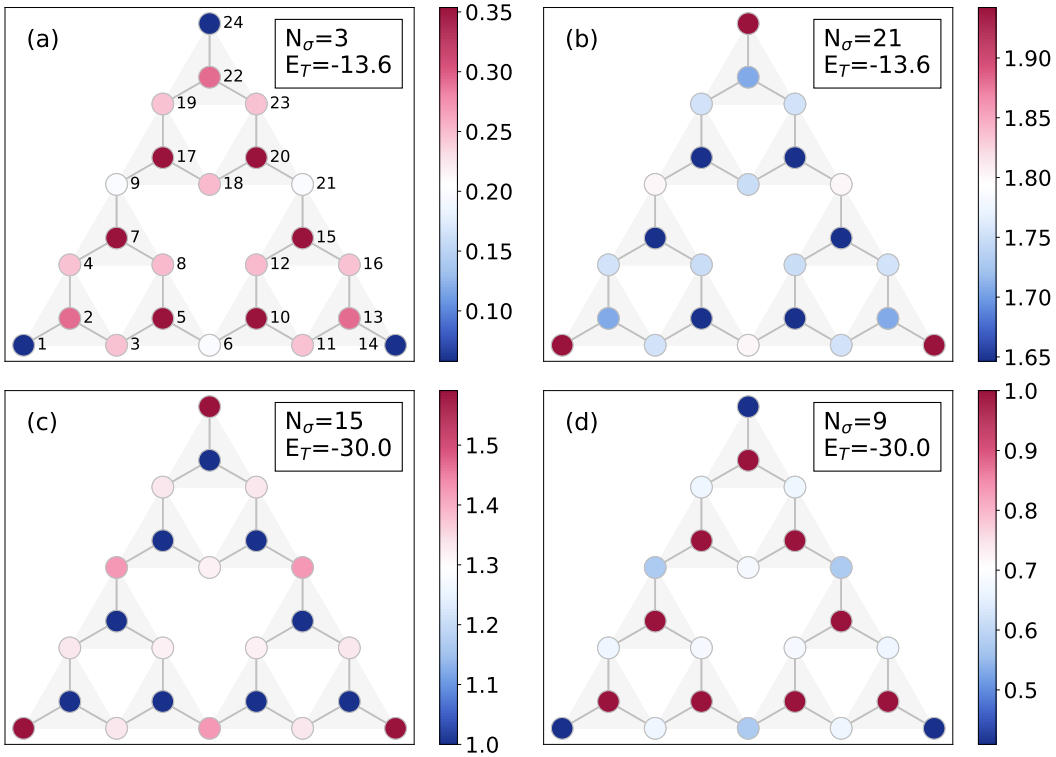

Figure 4.11: Average density configuration of the tight-binding ground-state on the second generation of the fractal lattice with filling (a) $N_\sigma = 3$, (b) $N_\sigma = 21$, (c) $N_\sigma = 15$ and (d) $N_\sigma = 9$.

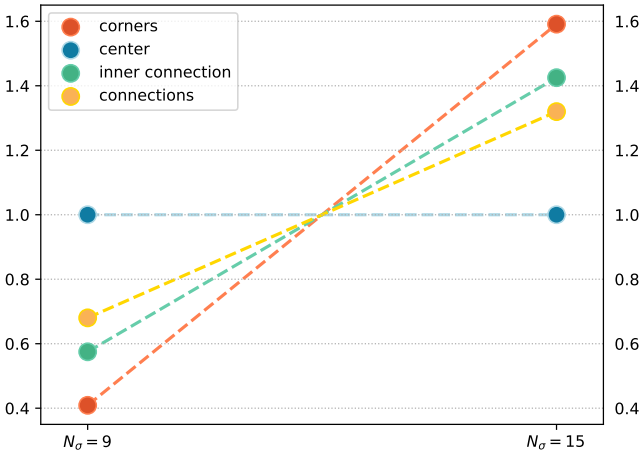

Figure 4.12: Increase in average density on the sites belonging to the 4 sub-set of lattices we identified in the configuration with $N_\sigma = 9$ and $N_\sigma = 15$. This representation doesn't contain information about the density in the fillings between 9 and 15, but only compares the values at these two fillings.

4.3.1 Spectral Analysis

Following the same method used for the first generation, we obtain the energy spectrum of the Hamiltonian at the single-particle level. The results are shown in Figure 4.13(a), where we can count the number of zero-energy degenerate states to be 6 for this generation. This number corresponds to the dimension of the degenerate space of energy zero, i.e. to the number of linearly independent basis states. In the first generation, we selected the eigenstate χ_4 of Figure 4.6(a) and by a rotation of 120 degrees clockwise and counterclockwise, we found the other two eigenstates. In order to explain the existence of 6 degenerate states, the idea is to find two prototypical states, the rotation of which gives 6 basis of the degenerate sub-space, meaning that they need to be linearly independent and generate the possible states in the space. We proceed by constructing these eigenstates manually, since numerically we would obtain combinations of the building-blocks states that we are looking for. On the other hand, the numerical solutions are useful to detect that indeed destructive interference still takes place and that the states belonging to the zero-energy band are CLS. An example is shown in Figure 4.13(b).

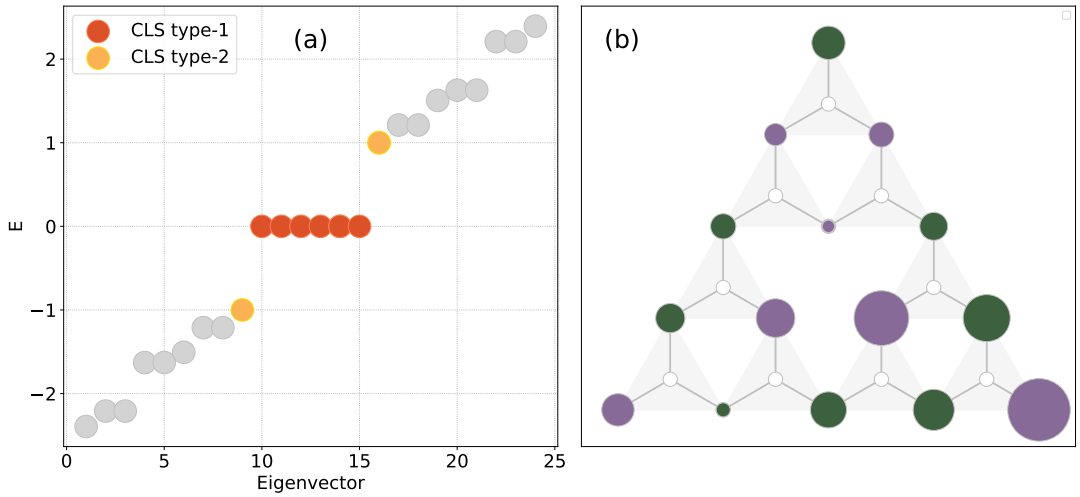

Figure 4.13: (a) Energy spectrum of the single-particle tight-binding Hamiltonian of the second generation of the fractal lattice. (b) An eigenvector belonging to the zero-energy band CLS type-1. Dark-green and purple dots on the lattice represent, respectively, negative and positive amplitude of the wave-function on the sites. On sites where there are no dots, the amplitude is zero.

Figure (4.14) shows the two basis-state prototypes that we found for the second generation. On sites in the centre of the triangles, the sum of the amplitudes of neighbouring sites must be zero due to destructive interference. Hence, we claim that these two states and their respective rotations of 120 degrees span the zero-energy degenerate space, giving in total 6 eigenstates. Once again, we see the origin of the corner states: these eigenstates share states on the corners, the amplitude of which gets amplified when taking linear combinations.

Moreover, we see that also some of inner connection sites are shared between multiple basis states. For example, site 4 is populated in both state in Figure 4.14(a) and in Figure 4.14(b),

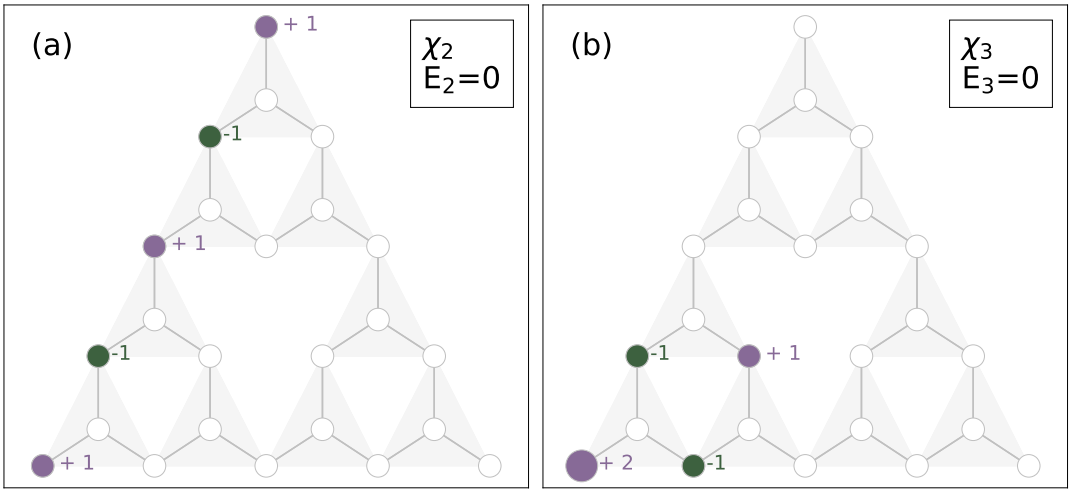

Figure 4.14: Prototype basis states in the zero-energy degenerate space of the second generation of the fractal lattice.

and this is the reason why the density on these states gets notably amplified. Comparing with the case of the corners, we can explain the reduced rise in density by noticing that corners are shared between three different basis states and one of them with double amplitude, while some of inner connection stated are shared by only two basis states. Regarding the connections between the three 1st generation triangles, they are not shared by different basis states. Hence, their amplitude grows, but does not get amplified, and this is why the growth of the density is smaller in Figure (4.12).

Studying non-zero energy levels also revealed the presence of CLS. Figure 4.15(a) shows the energy spectrum of the second generation and puts in evidence eigenstates where compact localization takes place: aside from the zero-energy level also found in the first generation CLS type-1, we observe the formation of a new type of CLS, one at energy level $E_T = 1$ and one at $E_T = -1$, referred to as CLS type-2. The amplitudes of the wave-functions of the new class of eigenvectors are shown in Figure (4.15), together with their parity on the lattice sites. Here and in the remaining of the work, the type of a CLS identifies where destructive interference takes place: states belonging to the same type have zero amplitude on the same sites.

In this new type of CLS, destructive interference is not restricted to only one of the sub-lattices and takes place along the three reflection symmetry axis. This is the reason why this state is not present in the first generation, where all the sites belong to the symmetry axis. Moreover, it is already possible to predict that the property of compact localization will persist in the next generations with the same energy: the corners are empty, so the entire configuration will not be perturbed by adding compact localized configurations with same energy to the corners.

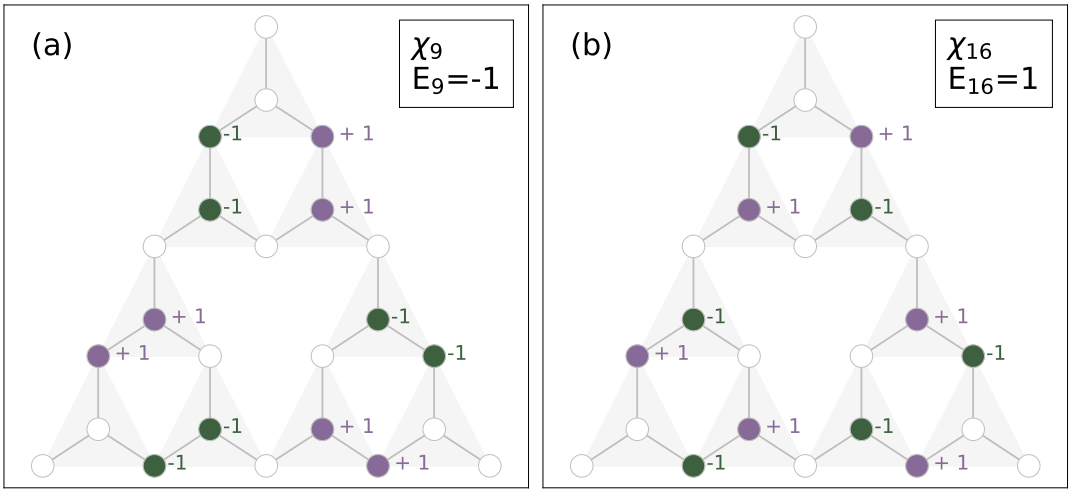

Figure 4.15: Eigenstates corresponding to the eigenvalues of the two-fold unitary degenerate level CLS type-2. (a) One of the eigenvectors with energy $E = -1$. (b) One of the eigenvectors with energy $E = 1$. They are the second type of CLS found by spectral analysis.

4.4 Higher Generations

With the aim of understanding how the states in the unitary energy level behave in higher generations and, perhaps, find new CLS, let us consider the spectrum of the tight-binding Hamiltonian for a next generation, shown in Figure (4.16).

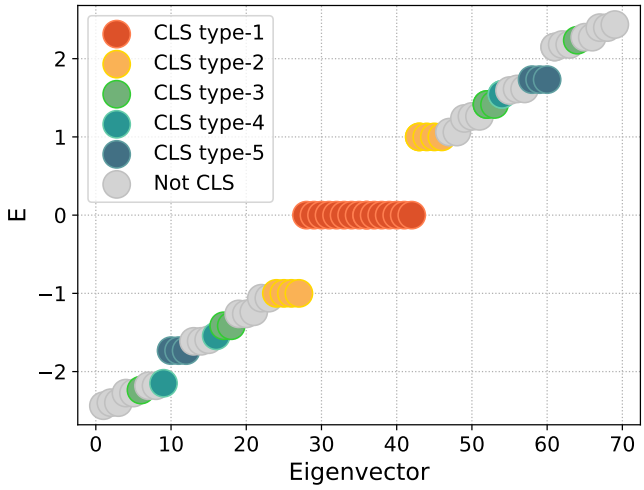

Figure 4.16: Energy spectrum of the tight-binding Hamiltonian on the third generation of the fractal lattice. Energies of eigenvectors where compact localization takes place are identified by dots of different colors. Each color corresponds to a type of CLS. The light-gray dots identify eigenvalues corresponding to eigenvector that do not have property of compact localization.

In the third generation, CLS with unitary energy become four-fold degenerate and other three types of CLS appear at different energy levels. Figure (4.17) represents the different types of CLS on the third generation, without considering the type-1, which has destructive interference in the centre sites, since it doe not add new information.

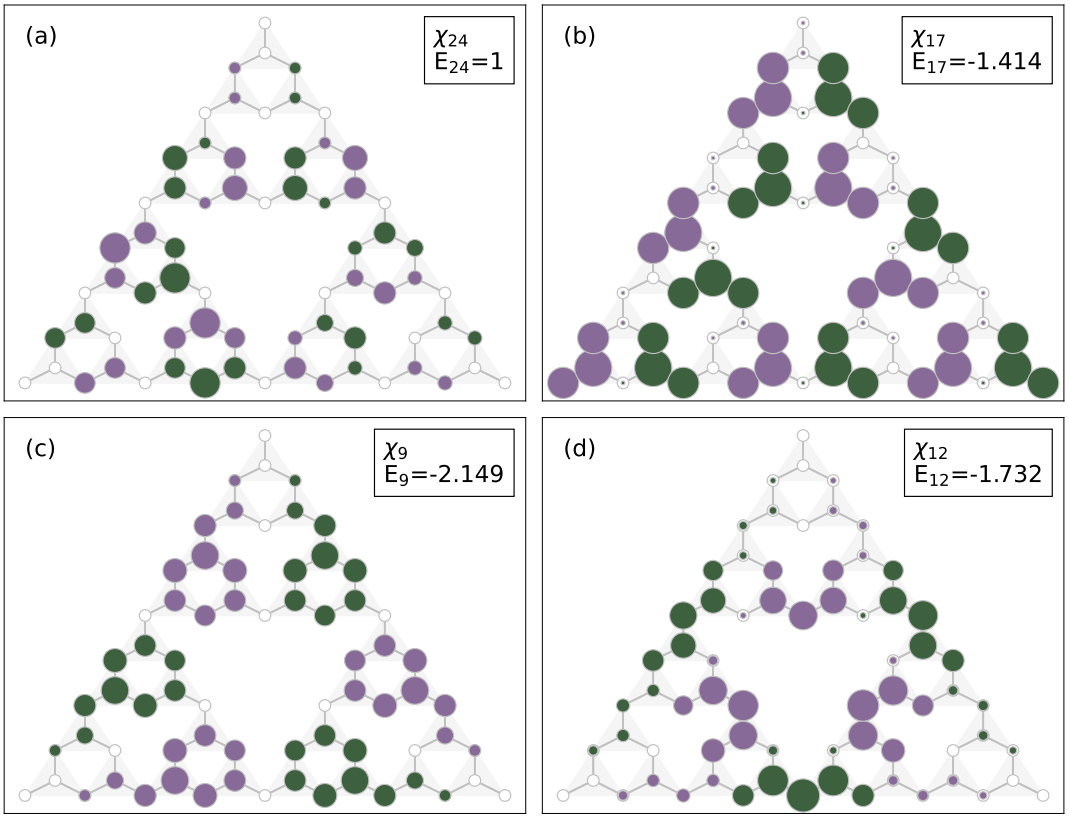

Figure 4.17: Four types of CLS on the third generation of the fractal lattice. (a) One of the CLS type-2 with energy $E = 1$, (b) one of the CLS type-3 with energy $E = \sqrt{2}$, (c) CLS type-4 with energy $E = -2.149$, (d) one of the CLS type-5 with energy $E = \sqrt{3}$. The dark-green (purple) dots indicate sites with negative (positive) parity, the size of the dots is indicative of the value of the amplitude: the bigger the dot the higher the amplitude.

In Figure 4.17(a), it is possible to observe how the CLS with unitary energy evolves in the next generation: destructive interference happens on sites along the symmetry axis of the three 2nd generation triangles. These sites are obtained by adding CLS of unitary energy of the second generation to the base-corners of another CLS of the same kind. Figure 4.17(b) shows an example of CLS type-3, which appears on four different energy levels, with energy $E = \pm\sqrt{2}$ and $E = \pm\sqrt{5}$. A possible CLS of type-4 is represented in Figure 4.17(c). It corresponds to the eigenvector of the non-degenerate energy level $E = -2.149$. This type of CLS, also present at non-degenerate energy levels $E = 2.149$ and $E = \pm 1.543$, present destructive interference on the symmetry axis of the 3rd generation triangle. Finally, in Figure 4.17(d) we observe one of the CLS of type-5. They appear at the three-fold degenerate levels $E = \pm\sqrt{3}$.

We studied how the number of CLS states within the CLS energy levels that appear in the third generation changes when increasing the generation of the lattice. The scaling behaviour is presented in Figure (4.18) and shows that the number of CLS states of types $1, 2, 4$ and 5 tends to scale as the Hausdorff dimension when the generation number increases. We notice that CLS states of type-4 share the same scaling, even if they belong to different energy levels, see Figure (4.16). Regarding CLS of type 3, we found that the number of states in the corresponding energy levels $\pm\sqrt{2}$ and $\pm\sqrt{5}$ does not increase but remains the same for odd generations, and is zero for even generations, see Table (4.1).

E	g_1	g_2	g_3	g_4	g_5	g_6	g_7	g_8
$\pm\sqrt{2}$	0	0	2	0	2	0	2	0
$\pm\sqrt{5}$	0	0	1	0	1	0	1	0

Table 4.1: The number of CLS of type-3 in energy levels $E = \pm\sqrt{2}$ and $E = \pm\sqrt{5}$, from the first generation g_1 to generation g_8.

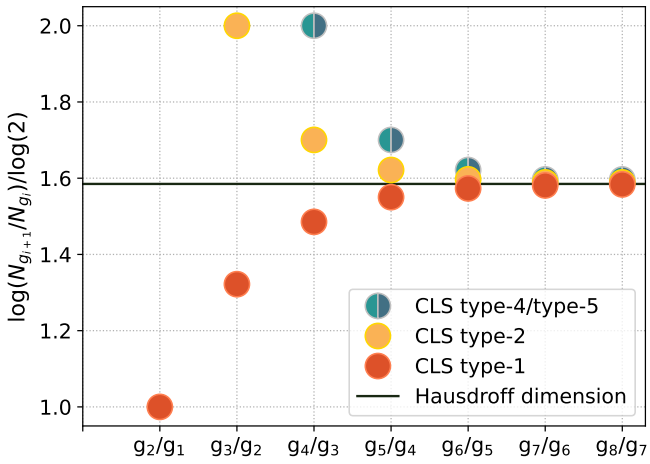

Figure 4.18: Scaling of the number N of CLS of different types when increasing the generation of the fractal triangle, from first generation g_1 to generation g_8.

Motivated by these scaling behaviours, we also studied how the many-body ground-state energy E_T at half-filling changes when increase the generation. As shown in Figure (4.19), this values also scales as the Hausdorff dimension. It is therefore possible to derive it by recursively computing it upon increasing the generation without, the need of diagonalizing the Hamiltonian. This also holds for the number of CLS in the energy levels shown in Figure (4.18), and constitutes a great advantage because the computational cost increases rapidly as we increase the generation.

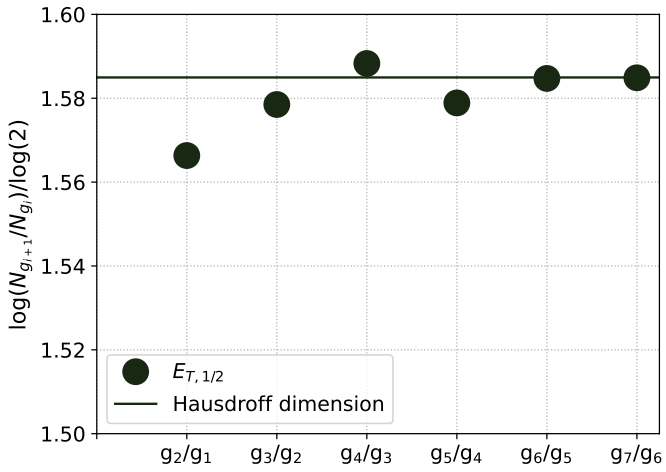

Figure 4.19: Scaling of the ground-state many-body energy at half-filling $E_{T,1/2}$ when increasing the generation of the fractal triangle, from first generation g_1 to generation g_8.

As a last addition to the analysis of the zero-energy level, we looked at the average density on the corners in the last configuration of the half-filling energy level of the many-body spectrum. This means, for example, filling $N_\sigma = 6$ for the first generation, $N_\sigma = 15$ for the second and so on. We noticed that its value is $\langle n \rangle \simeq 1.5909$ for every generation we implemented, very close to the Hausdorff dimension.

5 | Quantum Monte Carlo

5.1 Introduction to Monte Carlo methods

Monte Carlo (MC) methods represent a class of algorithms that use (pseudo-) random numbers to estimate quantities of interest. It has applications in the most diverse fields of science, ranging from economics to quantum physics.

In Quantum Physics, where those methods are dubbed as Quantum Monte Carlo (QMC), notable applications include the solution of differential equations and the computation of expected values. The latter case gives good intuition on how QMC methods work, therefore let us consider the computation of an expected value of the form:

$$\langle E \rangle = \int_{\xi_0}^{\xi_F} p(\xi) E(\xi) d\xi \tag{5.1}$$

where E is the observable we want to study and ξ_i is some variable distributed according to the probability distribution function (pdf) $p(\xi)$. When an analytical solution to Eq. (5.1) is not possible, one can appeal to numerical integration. For integration of multi-dimensional variables, numerical algorithms, such as the trapezium rule, will certainly fail due to long computational time. In these cases, MC methods are often the optimal solution since the simulation time scales algebraically with the number of variables. For simplicity, we will consider the one-dimensional case; the generalization to higher dimensions is straightforward.

The most intuitive way of proceeding to numerically perform the calculation in Eq. (5.1) is by randomly sampling the variables' interval $[\xi_0, \xi_F]$ a number N of times and compute

$$\langle E_N \rangle = \frac{1}{N} \sum_{i=1}^{N} p(\xi_i) E(\xi_i). \tag{5.2}$$

This estimate is more accurate the bigger is N. However, this method can be very inefficient: we are sampling less probable variables in the same way as we are sampling variables with high probability which, in turn, are the ones contributing the most to the sum in equation (5.2).

A smarter way of tackling the problem is by adapting a more efficient sampling method. In fact, we would like to be able to select the variables in a way that reflects their probability distribution, this means that we select with higher frequency more probable and meaningful values for

the variables ξ. There are different possible algorithms that can be used to achieve this goal, Metropolis and heat bath algorithms being two of them. If the random variables ξ are sampled according to their probability distribution, the MC estimate of Eq. (5.2) becomes

$$\langle E_N \rangle = \frac{1}{N} \sum_{i=1}^{N} E(\xi_i), \tag{5.3}$$

where the role played by the multiplication by the factor $p(\xi)$ is now replaced by the number of times a variable ξ is chosen. In other words,

$$p(\xi) \to \frac{N_\xi}{N}$$

where N_ξ is the number of times $\xi_i = \xi$.

In the next section, we pedagogically use MC methods together with Metropolis sampling to solve the problem of a quantum particle in a box in order to become familiar with the methods. After that, we will have the right tools to adapt this method to our complex system, for which we will need to introduce more advanced concepts and implementation strategies.

5.1.1 Metropolis Algorithm and Particle in a Box

As briefly introduced in the previous section, in order to compute Eq. (5.2) we need to sample random numbers ξ in a way that resemble their pdf p. For certain specific probabilities distributions, this can be achieved through formulas, such as de Box-Muller formula for Gaussian distributions. These types of formulas map uniformly distributed random numbers to random numbers that sample the desired distribution. When dealing with arbitrary distributions, the Metropolis algorithm is usually the optimal choice [37].

Starting from a randomly generated variable ξ_0, a chain of variables is generated via some transition probability $w(\xi_i \to \xi_j)$ of going from the variable ξ_i to ξ_j in one step of the process. To ensure that the set of variables asymptotically reaches the probability distribution p, the transition probabilities need to satisfy two conditions: *ergodicity* and *principle of detailed balance*. The former states that it is possible to reach any realization ξ_i from any other realization ξ_j in a finite number of steps, while the latter imposes a condition on the fluxes of configurations,

$$p(\xi_i) w(\xi_i \to \xi_j) = p(\xi_j) w(\xi_j \to \xi_i),$$

that symmetrizes the transition between two states. We can further write the transition probability as the product of the probability of performing the move $\alpha(\xi_i \to \xi_j)$ and the probability of accepting it $\text{acc}(\xi_i \to \xi_j)$

$$w(\xi_i \to \xi_j) = \text{acc}(\xi_i \to \xi_j) \alpha(\xi_i \to \xi_j).$$

Choosing the probability α to be symmetric, $\alpha(\xi_i \to \xi_j) = \alpha(\xi_j \to \xi_i)$, we get that the acceptance rule has to satisfy this condition

$$\frac{\text{acc}(\xi_i \to \xi_j)}{\text{acc}(\xi_j \to \xi_i)} = \frac{p(\xi_j)}{p(\xi)}$$

in order for the detailed balance principle to be satisfied.

In practice, the sampling algorithm proceeds in moves, each of which results in the generation of a value for ξ. Starting from a randomly chosen ξ_0, the first move consists in randomly generating a new possible outcome ξ_T and deciding to accept or reject this value basing the decision on the acceptance rule. If the move is accepted, the new value of ξ in the series is $\xi_1 = \xi_T$, otherwise the previous value is repeated $\xi_1 = \xi_0$. Iteratively implementing the move on the new generated value of ξ generates the desired set of variables.

The acceptance rule commonly used in Metropolis algorithm can be written as

$$\text{acc}(\xi_i \to \xi_T) = \min\left(1, \frac{p(\xi_T)}{p(\xi_i)}\right) \tag{5.4}$$

and considers the ratio r between the probability associated to the variable ξ_i the move is acting on and to the new generated variable ξ_T,

$$r = \frac{p(\xi_T)}{p(\xi_i)}.$$

The way it is implemented in practice is by performing the following checks:

- $r \geq 1$: the variable ξ_T is more probable than ξ_i, so it is selected to be the next element $\xi_{i+1} = \xi_T$,
- $r \leq 1$ but $r \geq \epsilon$ where ϵ is a uniform random number in the interval $[0, 1]$: the variable ξ_T is not more probable than ξ_i, but it is still probable enough to be accepted,
- both the previous conditions are not satisfied: the move is rejected and $\xi_{i+1} = \xi_i$.

The second point in the list is there to avoid the generation of a sequence of variables with increasing probability and to make sure that the simulation does not get stuck in configurations of local minima. It is easy to see that the rule in Equation (5.4) satisfies detailed balance, which, for the transition between states ξ_i and ξ_T, can be written as

$$p(\xi_i)\text{acc}(\xi_i \to \xi_T) = p(\xi_T)\text{acc}(\xi_T \to \xi_i)$$

assuming α symmetric. Substituting 5.4 in this equation we find the identity

$$\min\left[p(\xi_i), p(\xi_T)\right] = \min\left[p(\xi_T), p(\xi_i)\right]$$

which confirms that detailed balance is satisfied.

To get a pedagogical intuition of a practical application of this method, let us consider a particle in one dimension confined in an infinite square-well potential located at equal distance $L/2$ away from the origin along the x axis. The Hamiltonian reads

$$H = -\frac{1}{2}\frac{d^2}{dx^2} + V(x)$$

where, for simplicity, we set to unity the ratio $\hbar^2/m$ with m being the mass of the particle. The potential is described by the function

$$V(x) = \begin{cases} 0 & -L/2 < x < L/2 \\ \infty & \text{otherwise.} \end{cases}$$

In a variational sense, our goal is to compute an upper-bound to the ground-state energy E_0 using a parabola as a trial wave-function, which reads

$$\Psi_T(x) = A\left(-\frac{4}{L^2}x^2 + 1\right),$$

where A is a normalization factor. The expectation value of the Hamiltonian on this trial function can be computed using the definition of the expectation value of an observable

$$E_T = \langle \Psi_T | H | \Psi_T \rangle$$

which can be written in position coordinates using the completeness of the coordinates basis

$$E_T = \int_{-L/2}^{L/2} dx \Psi_T^*(x) H \Psi_T(x) = \int_{-L/2}^{L/2} dx \, |\Psi_T(x)|^2 \, \frac{H\Psi_T(x)}{\Psi_T(x)} \tag{5.5}$$

where we multiplied and divided by $\Psi_T(x)$ in order to get an expression similar to Eq. (5.1). We can interpret the modulus squared as a probability function,

$$p(x) = |\Psi_T|^2 = A^2\left(-\frac{4}{L^2}x^2 + 1\right)^2$$

and the remaining term in the integral as a quantity that we will call *local energy*

$$E_L(x) = \frac{H\Psi_T(x)}{\Psi_T(x)} = \frac{4}{L^2}\frac{1}{(-\frac{4}{L^2}x^2 + 1)},$$

so that now we are able to tackle the problem of solving the integral with the Monte Carlo approach.

The problem we are considering and numerically solving is analytical easy to solve. It just consists in performing the integral in equation (5.5), the result of which is

$$E_T = \frac{8A^2}{3L}$$

but the whole point of this example is to give a first approach to Monte Carlo methods, being able to compare its output with the exact solution.

In our simulation, we divide the total number of moves, or steps, N_S in a number N_B of blocks with $N_{SB} = N_S/N_B$ steps per block. We do this to take care of the fact that successive measures of local energies are not independent of each other (the value of the local energy at a certain time step is found by adding a new contribution to the energy of the previous step). At each step, we use Metropolis sampling to update the position x and we compute the associated local energy

$E_L(x)$. Every block consists in N_{SB} measures of local energy $E_{L,1}, \ldots, E_{L,N_{SB}}$, the expectation value is given by

$$E_B = \frac{1}{N_{SB}} \sum_{i=1}^{N_{SB}} E_{L,i}$$

following the MC scheme as in equation (5.3).

At the end of the simulation, we have a set of N_B block energies, which are variables we can consider to be independent and that constitute our statistical population. Each block energy has they same probability $1/N_B$, so the expectation value coincides with the average

$$E = \frac{1}{N_B} \sum_{i=1}^{N_B} E_{B,i}. \tag{5.6}$$

while the variance relative to the set of block energy variables E_B is given by

$$\sigma^2_{E_B} = \frac{1}{N_B} \sum_{i=1}^{N_B} (E_{B,i} - E)^2.$$

We are not interested in the distribution of the block energies but rather in their mean and in the distribution of the mean. For this reason, at each block step, we consider the set of block energies computed until then to be samples of the entire population of block energies. Their mean value, that we can call sample mean, is a random variable itself and follows its own probability distribution, also known as sample mean distribution. For the central limit theorem, we know that this distribution tends to the normal distribution $N(E, \sigma_{E_B}/\sqrt{N_B})$ for large N_B and finite variance. Therefore, the variance associated to the mean of the block energies is the following:

$$\sigma^2_E = \frac{\sigma^2_{E_B}}{N_B} = \frac{1}{N_B - 1} \frac{1}{N_B} \sum_{i=1}^{N_B} (E_{B,i} - E)^2 = \frac{\langle E_B^2 \rangle - E^2}{N_B - 1}.$$

Finally, to get a better approximation of the output, we divide the set of blocks in two types: equilibration and accumulation blocks. In the equilibration blocks, we perform Monte Carlo steps and measure the energies, but we do not count them when we perform the block energies average because only the accumulation blocks contribute to it. This is because we want to let the system first equilibrate to a region where the position outcomes are meaningfully probable, and then accumulating the values of block energies for the final average. Moreover, having an equilibration regime allows to get rid of the bias introduced by the random initial choice for the position and to achieve detailed balance.

We are now ready to start implementing the simulation and study the parameters of the model to get the best result. The first parameter that we want to investigate is the number of equilibrium blocks given the number of steps per block, that we will set to $N_{SB} = 500$. Figure (5.1) shows the behaviour of the block energy in block-step time and suggests that a number of equilibrium blocks $N_{EQ} = 15$ is sufficient to reach equilibrium, since the system at that point is already fluctuating around the exact value.

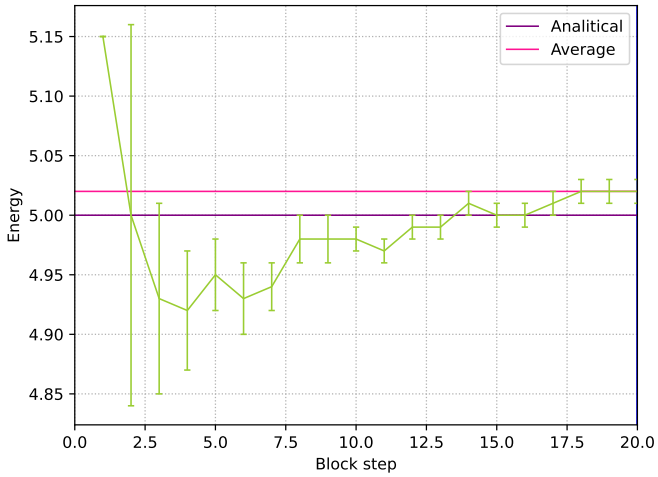

Figure 5.1: Plot representing the value of block energy (the average of local energies computed at each step) as a function on block step in the equilibration pahse. The purple horizontal line indicates the analytical value of energy found by analytically integrating equation (5.5). The dark-pink line indicates the value of the final average energy, so the result of our simulation.

Having set the equilibration blocks, we choose the number of accumulation blocks high enough, so that the result of the simulation (the average energy over the blocks in equation (5.6)) is in accordance with the exact result within the error interval. Recalling that the distribution of the sample mean tends to a normal distribution, we are 95% sure that the average we compute lays in the interval $[E-2\sigma_E, E+2\sigma E]$. In Figure (5.2) we show the behaviour of the block energies in

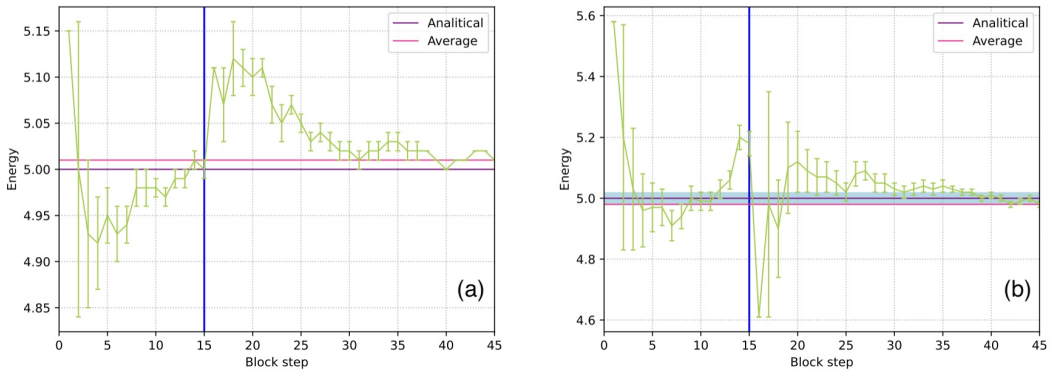

Figure 5.2: Plots representing block energy in block-step time for different values of N_{SB}. (a) $N_{SB} = 1$, (b) $N_{SB} = 15$. The vertical blue line delimits the equilibration region (to the left) to the accumulation region (to the right). The light-blue shaded region in (b) indicates the confidence interval of 2σ around the average E. In (a) the error is smaller than numerical accuracy.

block-step time before and after the equilibration period for a number of $N_{AC} = 30$ accumulation blocks and we also indicate the confidence interval. Since the agreement of the simulation with the expected value Figure 5.2(a) is not optimal, we decided not to measure at each time-step in each block, but to introduce a number, N_{ME}, that indicates how many steps we make

before measuring the energy. The result for a value of $N_{ME} = 15$ is shown in Figure 5.2(b). This procedure is made to avoid considering local energies that are still correlated, which can bias the numerical result.

This method of proposing a trial wave-function to describe the system in a variational sense, and computing the integrals with MC is known in literature as the Variational Monte Carlo method. It is applied nowadays in the simulation of complex many-body systems, the Hubbard Model being one of them [2].

5.2 Constrained-Path Auxiliary-Field Quantum Monte Carlo

In this section, we are going to formulate the theoretical background behind the QMC method used to solve the Hubbard Model on the fractal lattice. The method is called Constrained-Path Auxiliary-Field Quantum Monte Carlo (CP-AFQMC). The meaning of this terminology and the reasons for its need will be clarified in the following paragraphs.

5.2.1 Ground-State Projection

We start considering the imaginary-time dependence of some wave-function $|\Psi(\tau)\rangle$. This is found by applying the imaginary-time evolution operator to a wave-function at a certain initial time $\tau = 0$, called trial wave-function Ψ_T

$$|\Psi(\tau)\rangle = e^{-\tau(H-E_T)} |\Psi_T\rangle , \tag{5.7}$$

where H is the Hamiltonian of the system and E_T is the energy of the trial wave-function. We take a complete basis made of eigenstates of the Hamiltonian, denoted by $\{\Phi_n\}$ which satisfy

$$H |\Phi_n\rangle = E_n |\Phi_n\rangle ,$$

with E_n the energy eigenvalue associated with the $n-$th eigenvector. It is possible to decompose the wave-function at $\tau = 0$ on this basis

$$|\Psi_T\rangle = \sum_n c_n(0) |\Phi_n\rangle \tag{5.8}$$

introducing some time-dependent coefficients $c_n(\tau)$. Using this expansion and the fact that Φ_n are eigenvectors of the Hamiltonian, equation (5.7) becomes

$$|\Psi(\tau)\rangle = \sum_n c_n(0) e^{-\tau(H-E_T)} |\Phi_n\rangle = \sum_n c_n(0) e^{-\tau(E_n-E_T)} |\Phi_n\rangle .$$

In the limit of large τ, the contributions from exited eigenstates decay exponentially faster than the contribution of the ground state Φ_0. Therefore, for large τ,

$$|\Psi(\tau)\rangle \propto |\Phi_0\rangle .$$

This yields an approach to find the eigenstate of the Hamiltonian: we start from a certain wave-function $|\Psi(0)\rangle = |\Psi_T\rangle$, not orthogonal to $|\Phi_0\rangle$, and we evolve it in imaginary-time long enough

for it to be proportional to the desired ground-state wave-function. The energy E_T is updated in a self-consistent way during the simulation in order to be an approximation to E_0 and slow the exponential decay of the exponential coefficient.

We are then left with the task of evolving the initial wave-function in time, as in equation (5.7). The exponential of the kinetic part of the Hamiltonian simply involves a matrix multiplication: suppose we have an $M \times M$ matrix U, where is the number of single-electron basis states. Its exponential $B = e^U$ is an $M \times M$ matrix itself. Hence, applying it to the Slater determinant $\Psi(\tau)$, which has dimensions $M \times N$, only involves a matrix multiplication. The challenging part comes from the two-body operator in the interaction, which we cannot write as a $M \times M$ matrix. Moreover, the kinetic and interacting parts of the Hamiltonian, that we indicate with K and V, do not commute. Therefore, we have that

$$e^{-\tau H} \neq e^{\tau K} e^{\tau V}.$$

We can use the *Trotter approximation* to the second order to separate the terms in the exponential

$$e^{-\tau H} \sim e^{-\frac{\tau}{2}K} e^{-\tau V} e^{-\frac{\tau}{2}K},$$

which only this holds for sufficiently small values of τ. Thus, we can divide τ into a sufficiently large number N of intervals

$$e^{-\tau H} = \prod_{i=1}^{N} e^{-\delta\tau H}$$

and apply the Trotter decomposition to the exponent in the product

$$e^{-\delta\tau H} = e^{-\frac{\delta\tau}{2}K} e^{-\delta\tau V} e^{-\frac{\delta\tau}{2}K} + \mathcal{O}(\delta\tau^2). \tag{5.9}$$

By choosing a sufficiently large number of steps, we can make the error associated to the Trotter decomposition smaller than the statistical uncertainty associated to the MC methods. The procedure remains numerically exact.
We are essentially projecting an initial wave-function on the ground-state by evolving it in time. For this reason, we will call the operator

$$\mathcal{P}_{gs} = e^{-\delta\tau(H - E_T)}$$

ground-state projector. From this we are able to single out the contribution of the interaction term. In the next section, we show a method to deal with this term and make it numerically implementable in our basis of one-body orbitals.

5.2.2 Hubbard-Stratonovich Transformation

In this section, we focus on the exponential factor in Equation (5.9) that contains the problematic interaction term

$$e^{-\delta\tau V} = e^{-\delta\tau \sum_{i=1}^{M} U n_{i\uparrow} n_{i\downarrow}} = \prod_{i=1}^{M} e^{-\delta\tau U n_{i\uparrow} n_{i\downarrow}}. \tag{5.10}$$

We proceed by rewriting the product in the argument of the exponential using the following identity

$$n_{i\uparrow}n_{i\downarrow} = -\frac{1}{2}(n_{i\uparrow} - n_{i\downarrow})^2 + \frac{1}{2}(n_{i\uparrow} + n_{i\downarrow}).$$

The validity of this equation is promptly verified recalling that $n_{i\sigma}^2 = n_{i\sigma}$ for both $\sigma = \uparrow, \downarrow$. Considering the contribution to an individual $i-$th site, the exponential becomes

$$e^{\delta\tau U n_{i\uparrow}n_{i\downarrow}} = e^{-\delta\tau U(n_{i\uparrow}+n_{i\downarrow})/2} e^{\delta\tau U(n_{i\uparrow}-n_{i\downarrow})^2/2}. \tag{5.11}$$

The way we tackle the problem of having the two-body operator in the rightmost term in equation (5.11) is by performing a Hubbard-Stratonovich (HS) transformation, which allows to decouple quadratic exponential dependences. It makes use of a Gaussian integration property applied to the exponential of a certain operator $\hat{A}$

$$e^{\hat{A}^2} = \frac{1}{\sqrt{2\pi}} \int_{-\infty}^{\infty} dx e^{-x^2/2} e^{\sqrt{2x}\hat{A}}$$

by introducing the variable x, called *auxiliary-field*. The variable x is continuous and, in order for this method to be useful numerically, we use a discrete version of the HS [38], where the variable x can assume only two possible values $x_i = \pm 1$. The auxiliary variable is introduced to decouple the operators in the following way:

$$e^{\delta\tau U(n_{i\uparrow}-n_{i\downarrow})^2/2} = w \sum_{x_i=\pm 1} e^{x_i\gamma(n_{i\uparrow}-n_{i\downarrow})},$$

with w and γ to be determined by solving the equation for the possible values of the number operators $(n_{i\uparrow}, n_{i\downarrow})$. With the cases $(0,0)$ and $(1,1)$, we get

$$1 = 2w \quad \Rightarrow \quad w = \frac{1}{2},$$

while with the cases $(0,1)$ and $(1,0)$, we get a condition for the other free variable

$$e^{\delta\tau U/2} = w\cosh(\gamma).$$

We interpret the factor $w = 1/2$ as the probability for the auxiliary field to assume one of the two possible values $p(x_i) = 1/2$, so the system with on-site interaction

$$e^{-\delta\tau U n_{i\uparrow}n_{i\downarrow}} = e^{-\delta\tau U(n_{i\uparrow}+n_{i\downarrow})/2} \sum_{x_i=\pm 1} p(x_i) e^{x_i\gamma(n_{i\uparrow}-n_{i\downarrow})}$$

has been converted into a non-interacting system living in a space of fluctuating auxiliary fields, the summation of which restores the many-body interaction.

By applying the HS transformation to every site, which means introducing an auxiliary-field per lattice site, the interaction factor of equation (5.10) becomes

$$e^{-\delta\tau V} = \prod_{i=1}^{M} e^{-\delta\tau U n_{i\uparrow}n_{i\downarrow}} = \prod_{i=1}^{M} p(x_i) \sum_{x_i=\pm 1} e^{x_i\gamma(n_{i\uparrow}-n_{i\downarrow})},$$

which can be rewritten as

$$e^{-\delta\tau V} = \sum_{\vec{x}} P(\vec{x}) B_V(\vec{x}),$$

where we introduced the operators

$$P(\vec{x}) = \prod_i p(x_i) = \left(\frac{1}{2}\right)^M \quad \text{and} \quad B_V(\vec{x}) = \prod_{i=1}^{M} e^{-\delta\tau U(n_{i\uparrow}+n_{i\downarrow})/2} e^{x_i \gamma (n_{i\uparrow}-n_{i\downarrow})}.$$

Therefore, by using a Trotter decomposition and a Hubbard-Stratonovich transformation, the ground-state projector can now be expressed only in terms of one-body operators

$$\mathcal{P}_{gs} \sim e^{\delta\tau E_T} \sum_{\vec{x}} P(\vec{x}) B_{K/2} B_V(\vec{x}) B_{K/2},$$

where we introduced the kinetic operator $B_{K/2} = e^{-\delta\tau K/2}$.

5.2.3 Random walk in Slater Determinant Space

In the previous section, we discretized the imaginary-time, we now write the wave-function at a certain time-step n as $|\Psi^{(n)}\rangle$. In the method we use, these wave-functions are represented by a finite ensemble of Slater determinants

$$|\Psi^{(n)}\rangle \propto \sum_k |\phi_k^n\rangle$$

called *random walkers* and labelled by k. Here we omit a normalizing constant. Applying the ground-state projection to $|\Psi^{(n)}\rangle$ means applying it to each individual random walker, so that

$$|\phi_k^{(n+1)}\rangle = \mathcal{P}_{gs} |\phi_k^n\rangle$$

or, in an explicit form

$$|\phi_k^{(n+1)}\rangle = e^{\delta\tau E_T} \sum_{\vec{x}} P(\vec{x}) \left[B_{K/2} B_V(\vec{x}) B_{K/2}\right] |\phi_k^n\rangle\,, \tag{5.12}$$

where $\vec{x} = (x_1, x_2, \ldots, x_M)$ is a configuration of auxiliary fields. Implementing this expression implies generating all the possible configurations of these fields which, since we have M sites and in each of them the field can assume 2 values, are 2^M for each walker. The iteration of equation (5.12) is achieved stochastically using the idea of the MC integration scheme introduced in the first section: for each random walker we choose a configuration of fields $\vec{x}$ according to the probability distribution $P(\vec{x})$ instead of sampling the whole space of configurations. The walkers evolved in time represent the wave-function at the next time-step

$$|\Psi^{(n+1)}\rangle \propto \sum_k |\phi_k^{(n+1)}\rangle\,.$$

5.2.4 Importance Sampling

To make the algorithm more efficient, we introduce a scheme called *importance sampling*, in which we change the way how we sample the random walkers at each time step. The main idea is to make the sampling method reflect the importance of the walker relative to certain conditions. In fact, when we iterate

$$|\phi_k^{(n)}\rangle \longrightarrow |\phi_k^{(n+1)}\rangle = \sum_{\vec{x}} P(\vec{x}) B(\vec{x}) \, |\phi_k^{(n)}\rangle \,, \tag{5.13}$$

we are sampling the auxiliary fields considering a probability distribution $P(\vec{x})$ that is a constant, making it equally probable for any walker to be sampled. Our goal in this section is to introduce a sampling method that biases in a positive way our sampling procedure.

We start by introducing a function, called *importance function*, that computes the overlap between a certain walker and the trial wave-function $O_T(\phi_k) = \langle \phi_T | \phi_k \rangle$. This function is used to assign a weight $w_k = O_T(\phi_k)$ to each walker

$$|\Psi^{(n)}\rangle \propto \sum_k w_k^n \frac{|\phi_k^{(n)}\rangle}{O_T(\phi_k^n)} = \sum_k w_k^n \, |\tilde{\phi}_k^{(n)}\rangle \,,$$

so that now the ground state is represented by the ensemble of walkers $\{\tilde{\phi}_k\}$ that contribute with their respective weights. The individual walkers evolve with a modified probability distribution

$$|\tilde{\phi}_k^{(n)}\rangle \longrightarrow |\tilde{\phi}_k^{(n+1)}\rangle = \sum_{\vec{x}} \tilde{P}(\vec{x}) B(\vec{x}) \, |\tilde{\phi}_k^{(n)}\rangle \tag{5.14}$$

defined as

$$\tilde{P}(\vec{x}) = \prod_{i=1}^{M} \tilde{p}(x_i),$$

where $\tilde{p}(x_i)$ is the probability of choosing a value for the auxiliary field x_i on the $i-$th site and it is normalized using the normalization factor

$$\mathcal{N}_i = \tilde{p}(x_i = +1) + \tilde{p}(x_i = -1),$$

which is incorporated in the weights at each evolution of the potential operator

$$w_{k,i}^{(n)} = \mathcal{N}_i w_{k,i-1}^{(n)}.$$

For each walker and each lattice site, we need to update the auxiliary filed x_i, which can only assume two values. The Metropolis algorithm introduced in the second section of this chapter is not efficient, since the ratio between probabilities would be constant half of the time. Therefore, a *heat-bath* like algorithm is implemented: the value for the auxiliary field is chosen using as acceptance rule the pdf $\tilde{p}(x_i)/N_i$. In practice, a random number in $[0, 1]$ is generated. If the ratio of the acceptance rule for a field value x_i is larger than this value, the field x_i is accepted. Otherwise, the other possible value for the field is selected.

The new probability distribution $\tilde{P}$ is chosen so that it favours auxiliary-filed configurations that have a bigger overlap with the trial wave-function, in this sense we are guiding the simulation sampling taking into account the importance of the resulting wave-functions in representing the ground-state. It is important to mention that, even with this bias in the sampling of the $\vec{x}$, Equation (5.13) and Equation (5.14) are formally the same and the overall simulation gives unbiased estimates of ground-state properties. That said, a bad importance function can spoil the ground-state projection.

5.2.5 Computation of observables

In analogy to what was discussed in the example of the particle in the box, we divide the total number of steps (now imaginary-time steps) into blocks and, within each block, we perform measurements of the energy after each certain number of steps. The statistical analysis is equivalent.

At a given imaginary time-step, the total ground-state energy is defined as:

$$E^{(n)} = \frac{\langle \Psi^{(n)}|H|\Psi^{(n)}\rangle}{\langle \Psi^{(n)}|\Psi^{(n)}\rangle},$$

which, however, is computationally demanding to implement since each wave-function contains a sum of many Slater-determinants, the walkers. Therefore, we compute the so called *mixed estimator*

$$E^{(n)}_{\text{mixed}} = \frac{\langle \Psi_T|H|\Psi^{(n)}\rangle}{\langle \Psi_T|\Psi^{(n)}\rangle}.$$

Since $H\,|\Phi_0\rangle = E_0\,|\Phi_0\rangle$, the mixed estimator on the ground-state equals the ground-state energy

$$\frac{\langle \Psi_T|H|\Phi_0\rangle}{\langle \Psi_T|\Phi_0\rangle} = E_0.$$

As $|\Psi^{(n)}\rangle \to |\Phi_0\rangle$, the mixed estimator tends to the ground-state energy $E^{(n)}_{\text{mixed}} \to E_0$. Clearly, this estimator only provides unbiased average values of operators that commute with the Hamiltonian. The estimator we just introduced can be rewritten as a weighted average

$$E^{(n)}_{mixed} = \frac{\sum_k w_k E^n_k[\Psi_T, \Psi^{(n)}]}{\sum_k w_k} \quad \text{where} \quad E_k[\Psi_T, \Psi^{(n)}] = \frac{\langle \Psi_T|H|\Psi^{(n)}\rangle}{\langle \Psi_T|\Psi^{(n)}\rangle}. \tag{5.15}$$

The identity that we derived in the Appendix (B) can be applied in this context, enabling the computation of expressions of the form

$$\langle c^\dagger_{i\sigma} c_{j\sigma}\rangle = \left[\Psi^\sigma[(\Psi^\sigma_T)^\dagger \Psi^\sigma]^{-1}(\Psi^\sigma_T)^\dagger\right]_{ji}$$

This identity can be used for the computation of both kinetic and potential terms. The latter requires also the application of Wick's theorem, which enables to decouple the four-point expectation value into two-point expectation values, as already computed in the previous sections.

The computational method that we just introduced for the total energy is a valid procedure, but only works for observables that commute with the Hamiltonian. For the computation of quantities such as kinetic energy, potential energy and average density per site, namely in general, we need to propagate both sides of the product

$$\langle A \rangle = \frac{\langle \Psi^{(n)} | A | \Psi^{(n)} \rangle}{\langle \Psi^{(n)} | \Psi^{(n)} \rangle}.$$

A useful methodology, called *back propagation* [39], can be applied in these cases. It makes used of the relation

$$\langle A \rangle = \frac{\langle \Psi_T | e^{-\tau_{bp} H} A | \Psi^{(n)} \rangle}{\langle \Psi_T | e^{-\tau_{bp} H} \Psi^{(n)} \rangle},$$

which tends to the exact expectation value as the time τ_{bp} is increased. The idea behind the method is to represent the evolution $e^{-\tau_{bp} H}$ as a stochastic path, as we did for the $e^{-\tau H}$ term, expressing it as a product of operators $B(\vec{x})$. For the number of imaginary time steps corresponding to τ_{bp}, the information of the generated auxiliary fields at each time step is stored, and used to propagate in reverse order the ansatz wave-function to the left of the sandwich.

5.2.6 Sign Problem

Since we are dealing with electrons, the wave-functions $|\Psi^{(n)}\rangle$ that we consider are fermionic. This has the consequence that for each ensemble of walkers $\{|\phi\rangle\}$, there is another ensemble $\{-|\phi\rangle\}$ which represents the same $|\Psi^{(n)}\rangle$. The problem that can arise is that, along the sampling of auxiliary fields, the walkers go from one ensemble to the other, causing a fluctuation in the sign of the weighs w_k. The sum of weighs that fluctuates in sign is a computationally expensive task. Since we consider the sum in our calculations, see for example Equation (5.15), this method loses its efficiency.

The way we deal with the so called *sign problem* in this work, is by performing a *constrained path approximation*. The latter consists in imposing the overlap between the trial wave-function and the walker to be positive

$$\langle \Psi_T | \phi_k^{(n)} \rangle > 0.$$

In practice, this condition is implemented in the importance sampling by imposing $O_T(\phi_k) = \max\{\langle \phi_T | \phi_k \rangle, 0\}$, which means that we are preventing the negative walkers to be sampled and not discarding them. Finally, we observe that this approximation becomes exact when the trial wave-function $|\Psi_T\rangle$ coincides with the true ground-state. In auxiliary-field space, the two ensembles $\{|\phi\rangle\}$ and $\{-|\phi\rangle\}$ are divided by a node where $\langle \phi_0 | \phi \rangle = 0$. The two ensembles are equivalent, thus we could only consider one of them and know what happens in the other. However, since $|\phi_0\rangle$ is unknown, we can not locate the node and divide the two ensembles properly. We approximate the node to be $\langle \Phi_T | \phi \rangle$, which eliminates the sign problem, but introduces an error. We measure the size of this error in section (5.4.1).

5.3 Mean-Field Hartree-Fock Approximation

Before looking at the results of the implementation of the CP-AFQMC method introduced, we explain in this section the theory behind one of the other methods we used to tackle the interaction term in the Hamiltonian. To this aim, let us consider the Hubbard Hamiltonian, as introduced in Chapter (3)

$$H = -t \sum_{\langle i,j\rangle \in \Lambda} \sum_{\sigma} \left(c^{\dagger}_{i\sigma} c_{j\sigma} + c^{\dagger}_{j\sigma} c_{i\sigma} \right) + U \sum_{i \in \Lambda} n_{i\uparrow} n_{i\downarrow} \tag{5.16}$$

In this section, we tackle the issue coming from the two-body term by performing a mean-field Hartree-Fock approximation and we present the iterative scheme we apply to implement it.
The mean field approximation consists in writing the number operator as

$$n_{i\sigma} = \langle n_{i\sigma} \rangle + \delta n_{i\sigma}$$

the sum of a bulk part $\langle n_{i\sigma} \rangle$, that accounts for the major observable physics, and a term $\delta n_{i\sigma}$, which accounts for fluctuations around the mean value and are assumed to be small. The product of number operators in the Hubbard Hamiltonian for a single site becomes

$$\begin{aligned} n_{i\uparrow} n_{i\downarrow} &\simeq \langle n_{i\uparrow} \rangle \langle n_{i\downarrow} \rangle + \langle n_{i\uparrow} \rangle \delta n_{i\downarrow} + \langle n_{i\downarrow} \rangle \delta n_{i\uparrow} \\ &= \langle n_{i\uparrow} \rangle n_{i\downarrow} + \langle n_{i\downarrow} \rangle n_{i\uparrow} - \langle n_{i\uparrow} \rangle \langle n_{i\downarrow} \rangle \end{aligned}$$

when approximated to the first order in fluctuations. Replacing this term, the mean-field Hamiltonian can be written as the sum of independent spin-up and spin-down mean-field Hamiltonians

$$H_{MF} = H^{\uparrow}_{MF} + H^{\downarrow}_{MF} \tag{5.17}$$

where

$$H^{\sigma}_{MF} = -t \sum_{\langle i,j\rangle \in \Lambda, \sigma} \left(c^{\dagger}_{i\sigma} c_{j\sigma} + c^{\dagger}_{j\sigma} c_{i\sigma} \right) + U \sum_{i} n_{i\sigma} \langle n_{i\sigma} \rangle - \frac{U}{2} \sum_{i} \langle n_{i\uparrow} \rangle \langle n_{i\downarrow} \rangle .$$

After performing this approximation, only one-body operators remain, and we can solve the model by using the same techniques we adopted in the tight-binding limit, section (sec on tb). However, the term $\langle n_i \rangle$ is still unknown since computing expectation values requires the knowledge of the eigenfunctions, which are still unknown. To tackle this problem, we make use of a self-consinsten approach (Hartree-Fock method) together with the variational theory.

The idea behind the Hartree-Fock implementation is to start with a random Slater determinant $|\Phi_T\rangle$. Introduction the functional

$$E[\Phi_T] = \frac{\langle \Phi_T | H | \Phi_T \rangle}{\langle \Phi_T | \Phi_T \rangle}$$

we are allowed to state that, for the *variational principle*, the function Φ_T that minimizes this functional is an eigenfunction of the Hamiltonian

$$H \, |\Phi\rangle = E[\Phi] \, |\Phi\rangle$$

and the best approximation to the ground state Φ_0 with energy $E_0 < E[\Phi]$. In order to find the minimum of the functional, we proceed with an iterative scheme that consists in:

- Generate a random Hamiltonian H_T and a random Salter determinant $|\Phi_T\rangle$ and use it to compute $\langle n_i \rangle_T$ using (4.2). Diagonalizing H_T we find the energy E_T.

- Diagonalize the mean-field Hamiltonian

$$H^{\sigma}_{MF} = H^{\sigma}_{Free} + U \sum_i n_{i\sigma} \langle n_{i\sigma} \rangle_T - \frac{U}{2} \sum_i \langle n_{i\uparrow} \rangle_T \langle n_{i\downarrow} \rangle_T \tag{5.18}$$

- Find new Slater determinant $|\Phi_N\rangle$ and the energy of the system E_N from the diagonalization of H^{σ}_{MF}.

- Compare the energies E_N and E_T. If the difference is small enough, we have found the ground state (it was built taking the lowest energy single particle states) eigenfunction of the mean-field Hamiltonian. If it is not small enough, use Φ_N as a new Φ_T and diagonalize the H_{MF} again. Iterate this process until the difference in energy is small enough.

- Calculate the energy of the original Hamiltonian in this state using the mean-field ground state obtained at the end of the iterating process

$$\langle H \rangle_N = \langle \phi_N | H | \phi_N \rangle = \langle H_{Free} \rangle_N + U \sum_i \langle n_{i\uparrow} \rangle \langle n_{i\downarrow} \rangle . \tag{5.19}$$

To show the last equation in the list, we make use of *Wick's Theorem*, which allows us to decouple the mean of the two-body operator in the interaction term as a product of means of one body operators

$$\langle n_{i\uparrow} n_{i\downarrow} \rangle = \langle c^{\dagger}_{i\uparrow} c_{i\uparrow} c^{\dagger}_{i\downarrow} c_{i\downarrow} \rangle = \langle c^{\dagger}_{i\uparrow} c_{i\uparrow} \rangle \langle c^{\dagger}_{i\downarrow} c_{i\downarrow} \rangle - \langle c^{\dagger}_{i\uparrow} c^{\dagger}_{i\downarrow} \rangle \langle c_{i\uparrow} c_{i\downarrow} \rangle + \langle c^{\dagger}_{i\uparrow} c_{i\downarrow} \rangle \langle c_{i\uparrow} c^{\dagger}_{i\downarrow} \rangle . \tag{5.20}$$

The last two terms in the Wick's expansion vanish, the rightmost term due to the fact that spin up and down sectors are decoupled while the other due to conservation of the number of particles. Therefore we get:

$$\langle n_{i\uparrow} n_{i\downarrow} \rangle = \langle n_{i\uparrow} \rangle \langle n_{i\downarrow} \rangle .$$

Essentially, we applied the variational principle stated above to the mean-field Hamiltonian H_{MF} and used a self-consistently iterated approach to find the ground-state of the system.

However, if we look at equation (5.17) more carefully (Appendix C), we notice that the spin rotational invariance has been broken because it assumes S^z as the quantization axis. A more appropriate Hamiltonian that conserves this symmetry is found in Appendix C by using Wick's theorem to expand the product of operators in the interaction term. Using this expansion, shown in equation (C.2), we can write the full mean-fileld Hartree-Fock Hamiltonian

$$\begin{aligned} H_{HF} = -t \sum_{\langle i,j \rangle \in \Lambda, \sigma} \left(c^{\dagger}_{i\sigma} c_{j\sigma} + \text{h.c.} \right) + U \sum_{i \in \Lambda} \Big(& \langle n_{i\uparrow} \rangle n_{i\downarrow} + \langle n_{i\downarrow} \rangle n_{i\uparrow} + \langle n_{i\uparrow} \rangle \langle n_{i\downarrow} \rangle \\ & - \langle c^{\dagger}_{i\uparrow} c_{i\downarrow} \rangle c^{\dagger}_{i\downarrow} c_{i\uparrow} - \langle c^{\dagger}_{i\downarrow} c_{i\uparrow} \rangle c^{\dagger}_{i\uparrow} c_{i\downarrow} - \langle c^{\dagger}_{i\uparrow} c_{i\downarrow} \rangle \langle c^{\dagger}_{i\downarrow} c_{i\uparrow} \rangle \Big) \end{aligned} \tag{5.21}$$

which will be used instead of the previous mean-field Hamiltonian (5.18) in the implementation.

Finally, also the energy of the ground state we compute using equation (5.19) needs to be revised because the up and down sectors are not decoupled anymore (the Hamiltonian can not be separated in the separate contribution of a up and down Hamiltonian) and the rightmost term in equation (5.20) does not vanish. Therefore, we get the following:

$$\langle H \rangle_N = \langle \phi_N | H | \phi_N \rangle = \langle H_{Free} \rangle_N + U \sum_i \left(\langle n_{i\uparrow} \rangle \langle n_{i\downarrow} \rangle + \langle c^\dagger_{i\uparrow} c_{i\downarrow} \rangle \langle c_{i\uparrow} c^\dagger_{i\downarrow} \rangle \right).$$

5.4 Results

In this final section, we mainly present the results obtained from the implementation of the QMC method introduced in the previous sections. We start by validating the method by comparing it to exact diagonalization, thus considering a small lattice size and low electronic filling. This also allows to make a comparison with MF methods and find the reagion of interaction in which it can be considered a valid approximation. Then, we study how some of density configurations and many-body ground-state energies behave when interaction is added to the tight-binding model, we pay particular attention to the configurations that present larger density in the corners. Finally, we study the phases of the system in the second generation of the fractal-lattice.

5.4.1 Validity of the Method

The starting point of the implementation was the validation of the QMC method by comparing its results with exact ones, i.e. with results found by performing exact diagonalization (ED). We also compared these two methods with the MF approach to understand to what extent this approximation is appropriate. Since the simulation time required by ED scales exponentially with the system size and electron number, we considered a small system (the first generation of the Sierpinski triangle), with a couple of electrons ($N_\sigma = 1$). The quantities we considered were the total, kinetic and potential energy of the many-body ground-state, for values of the ratio $U/t \in [0.1, 9]$. For the rest of this chapter, we set the hopping parameter $t = 1$, and we label the interaction parameter U/t as simply U.

Recalling what was discussed in Chapter (4) about ED, computing the ground-state energy of such system involves the digonalization of a 81×81 matrix. The extrapolation of its eigenvalues with lowest energy gives the total ground-state many-body energy E_{ED}. The kinetic K_{ED} and potential V_{ED} energy are found by considering the eigenvector $|\Phi_{ED}\rangle$ corresponding to the lowest eigenvalue and computing the following quantities:

$$K_{ED} = \frac{\langle \Phi_{ED} | \hat{K} | \Phi_{ED} \rangle}{\langle \Phi_{ED} | \Phi_{ED} \rangle}, \qquad V_{ED} = \frac{\langle \Phi_{ED} | \hat{V} | \Phi_{ED} \rangle}{\langle \Phi_{ED} | \Phi_{ED} \rangle}.$$

The computation of these energies in the context of QMC is performed using back-propagation technique, introduced in Section (5.2.5).

Regarding the MF approach, in section (5.3) we showed the iterative procedure used to generate the variational ground-state wave-function, from which we derived the total E_{MF}, kinetic K_{MF} and kinetic V_{MF} energies.

In Figure (5.3), we present the behaviour of the energies computed using these three different methods, as the interaction strength increases. We see that for these parameters, the MF approximation can be considered valid only for small values of interaction, while the QMC approach follows very accurately the exact behaviour. We also notice that in the value of the kinetic energy computed by QMC for interaction $U = 6$ deviates from the exact solution and coincides with the MF solution. This fact could be a consequence of the fact that the MF ansatz is biasing the QMC.

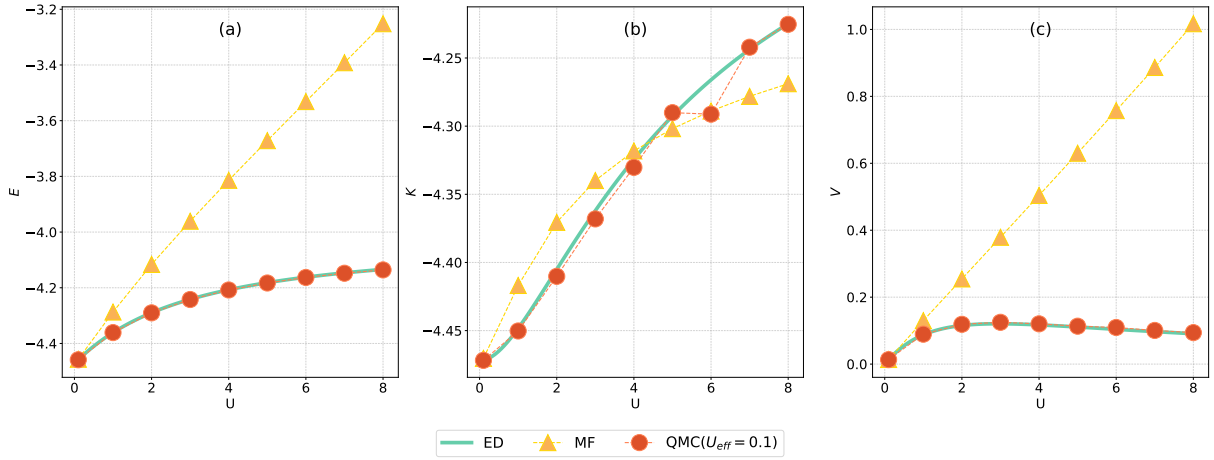

Figure 5.3: Comparison of the ground-state many-body energies as a function of interaction. We consider the first generation of the unfrustrated Sierpinksi triangle with $N_\sigma = 1$. These energies are computed with three different implementation methods: ED, MF, and QMC. (a) The total energy E, (b) the kinetic energy K and (c) the potential energy V.

At this stage, we recall that, in an importance sampling scheme, the QMC walkers are guided by a trial wave-function $|\Psi_T\rangle$ throughout their evolution in imaginary time, and this wave-function is taken to be the MF ground-state wave-function. Therefore, a bad MF ansatz influences negatively the QMC simulation. To understand the extent of this influence, we performed simulations of the first generation with $N_\sigma = 6$. We studied the behaviour of the QMC energies as the interaction strength is increased, with the simulation being guided by different MF ansätze. In particular, we performed simulations where the MF ansatz is generated using $U_{eff} = U$, where U_{eff} is the interaction strength used in the MF simulation, referred to as *effevtive potential*. This behaviour is indicated by the green curves in Figure (5.4). Then performed a simulation where we used a MF ansatz generated by fixing $U_{eff} = 0.1$ for every value of interaction strength. The simulation that provides the smallest total energy is the best approximation of the ground state, due to the variational principle. Figure 5.4(a) shows the ground-state energy. It is possible to observe that the latter ansatz gives better results for every value of interaction. The variational principle only applies to the total energy but, for completeness, we also show the behaviour of

kinetic and potential energies.

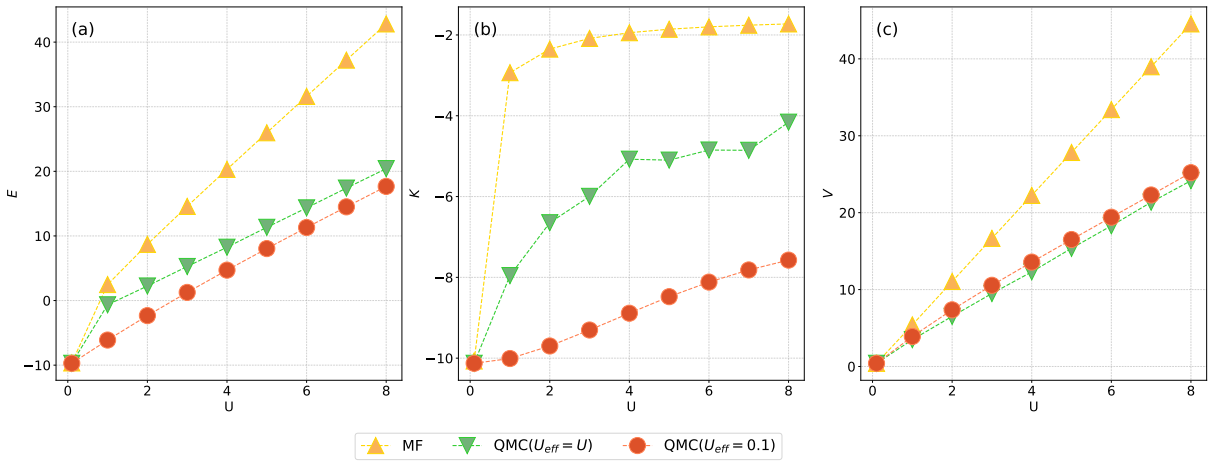

Figure 5.4: Comparison of the ground-state many-body energies as a function of interaction in the first generation of the unfrustrated Sierpinksi triangle with $N_\sigma = 6$. These energies are computed with three different implementation methods: MF, QMC ($U_{eff} = U$) and QMC ($U_{eff} = 0.1$). Different MF ansätze are considered in the QMC simulations. (a) Total energy E, (b) kinetic energy K and (c) potential energy V.

From this analysis, we can conclude that a preliminary study on the influence of the MF ansatz on the QMC simulation has to be performed before proceeding with the implementation. In fact, since the path of the walkers is influenced by the MF trial wave-function, a bad ansatz affects negatively the paths, making them deviate from the exact solution. Moreover, to handle the sign problem, we introduce a constrained-path approximation that renders systematic errors. However, those errors are small, as shown in Figure (5.3).

Moreover, we observe that QMC simulations are reliable for every value of interaction strength, while MF solutions can be considered to be valid for a value of approximately $U \simeq 1$. For this reason, we will focus on results performed using QMC simulations, MF remains useful to make the QMC more efficient.

5.4.2 Energy and Density in the many-body ground-state

In this section, we study the total energy and average density configurations of the ground-state when interaction is introduced in the model. This allows to understand the effects of interaction by comparing with the results obtained within the tight-binding limit discussed in Chapter (4).

Let us start considering the first generation of the fractal lattice. For different values of interaction U, we computed the ground-state energy as a function of electronic filling, the result is shown in Figure (5.5). When the interaction is close to zero, in Figure 5.5(a), the energy dependence on the filling is very similar to the tight-binding one. But now, the level around half-filling has a small slope. However, as we increase the value of interaction, we observe that the degen-

eracy at the lowest energy level is effectively broken, and that the energy for values of electronic filling that exceed half-filling increases, becoming more positive as U increases. Looking at the particle-hole transformed Hamiltonian in Equation (A.2), we can see that for the case of $U = 0$, the symmetry implies equal energies after the transformation: a state with N_p particles has the same energy as a state with $N - N_p$ holes. When the interaction is not null, there is an extra term $U(\Lambda - N)$ coming from the PHT, as shown in equation (A.2), that influences the behaviour and makes the energy dependence on the filling not symmetric around half-filling anymore. For example, we can see that in Figure 5.5(b) for $U = 1$ the value of energy corresponding to filling $N_\sigma = 9$ is $E_T(9) = 9$, obtained by summing to the PH symmetric value at $N_\sigma = 0$ the extra term coming from the transformation:

$$E_T(9) = E_T(0) + U(\Lambda - N) = 0 + 9 = 9.$$

As the strength of the interaction increases, the contribution from this term increases as well. This is shown in Figure 5.5(c) and Figure 5.5(d).

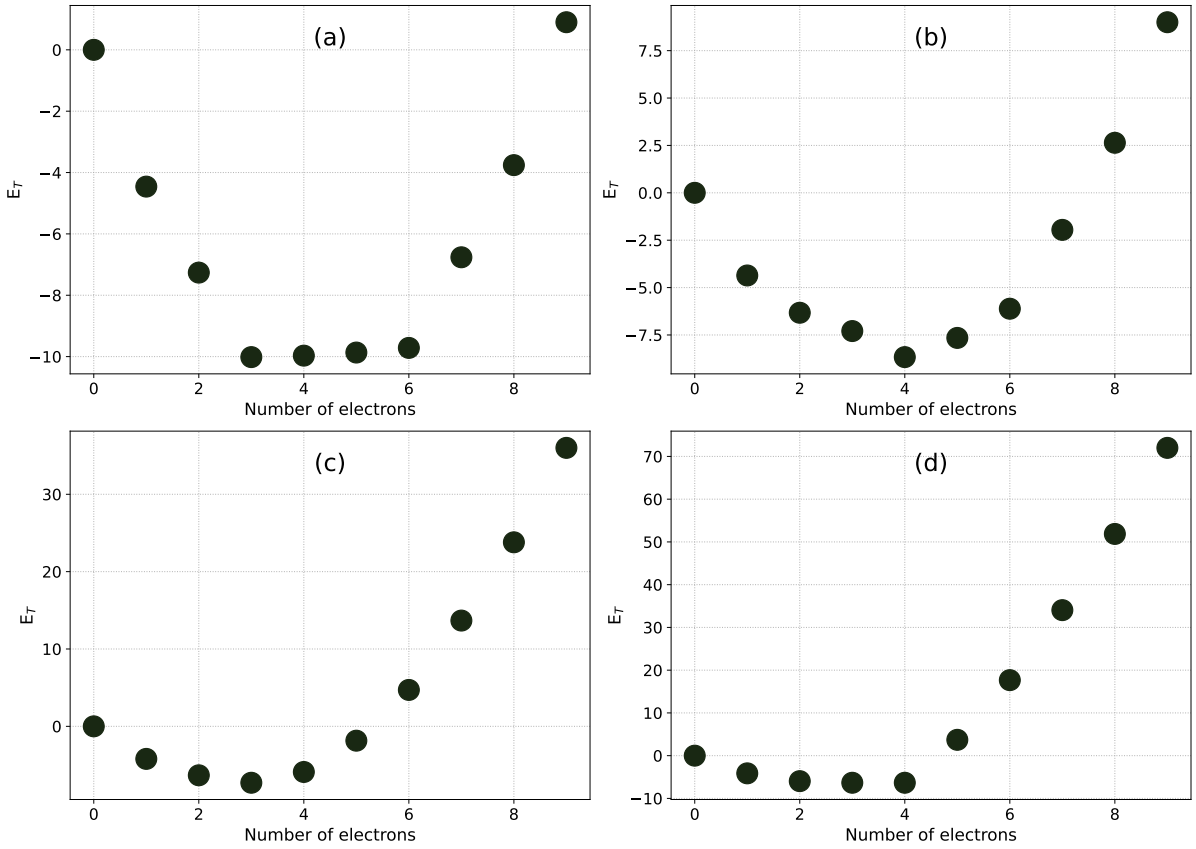

Figure 5.5: Many-body ground-state energy in the first generation of the unfrustrated Sierpinski lattice computed using MC. (a) $U = 0.1$, (b) $U = 1$, (c) $U = 4$ and (d) $U = 8$. The x axis in indicates the number of electrons of one kind σ, the total number of electrons in the system is $2N_\sigma$.

Then, we looked at the average density per site $n_i = \langle n_{i\uparrow} \rangle + \langle n_{i\downarrow} \rangle$ and, in particular, we considered the configuration where $N_\sigma = 6$, which corresponds to the last energy state in the degenerate energy-level found at $U = 0$. In the tight-binding studies, we understood that this state is a

consequence of the CLS, with destructive interference happening in the sites at the centre of the triangles. We also observed that the density in the corners has a value close to the Hausdorff dimension. Studying this configuration allows us to tackle the consequences of interaction in this type of states.

First, for small interaction ($U = 0.1$), we compare the density distributions obtained with the QMC and the MF methods. The results are shown in Figure (5.6). Comparing the results from the two methods, we observe that not only the QMC gives a smaller energy, but the density configuration is symmetrically distributed on the lattice. In fact, looking at the result from MF, Figure 5.6(a), we observe a small asymmetry in the distribution of the density on the pink and red sites. See, for example, the density on site 4 and 8 in Figure 5.6(a). We can divide the lattice in three groups of sites: sites $1, 6, 9$ called *corners*, sites $2, 5, 7$ called *center* and sites $3, 4, 8$ called *connections*. We expect the density to be the same in each of these groups, since there is no reason for an imbalance. We see this behaviour in the QMC simulation, while the MF simulation gives small discrepancies. We found these discrepancies to increase when we increase the interaction strength. This is another reason why we choose to focus on QMC results.

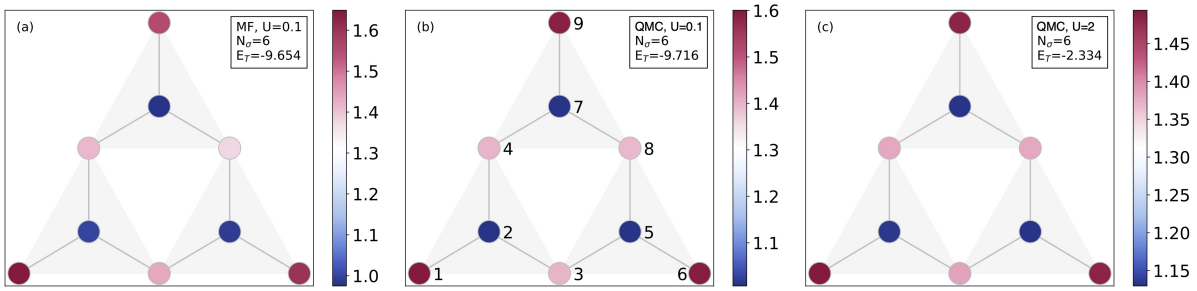

Figure 5.6: Average density per site for $N_\sigma = 6$ on the first generation of the Sierpinski triangle. (a) Configuration computed with MF and interaction $U = 0.1$, (b) configuration computed with QMC and interaction $U = 0.1$, (c) configuration computed with QMC and interaction $U = 2$.

Performing QMC simulations on the system with $N_\sigma = 6$ for different values of interactions revealed how the density configuration behaves when the spin-up and spin-down electrons interact. Figure 5.6(b) and Figure 5.6(c) show the result when we increase the interaction from $U = 0.1$ to $U = 2$. We set the color bar of the two figures to the same limits in order to be able to visually compare them. We observe that when the interaction is increased, the overall colors in the figures become more pale which, in the color bar representation chosen, means that the values of density in all groups of states get closer to the center value of the color bar: the density on corners and connections decreases, while the density in the centre sites increases. When there is no interaction, it seems energetically favourable to stuck electrons in the corners and let the ones in the bulk, where the sites have more connectivity, hop with higher probability. In the presence of interaction, positioning electrons in the corners is energetically expensive and, thus, the electrons move to the bulk. Finally, it is interesting to notice that the density on connection sites does not vary as much as it varies on other types of sites. This could be due to the fact that

those sites have on intermediate number of nearest neighbours.

With the aim of studying how the density configurations change when the interaction is increased even more, we took advantage of the fact that the values of density on the lattice can be divided in three groups, and we restricted the study to their behaviour instead of considering the configurations as a whole. The result of this investigation is shown in Figure (5.7). We

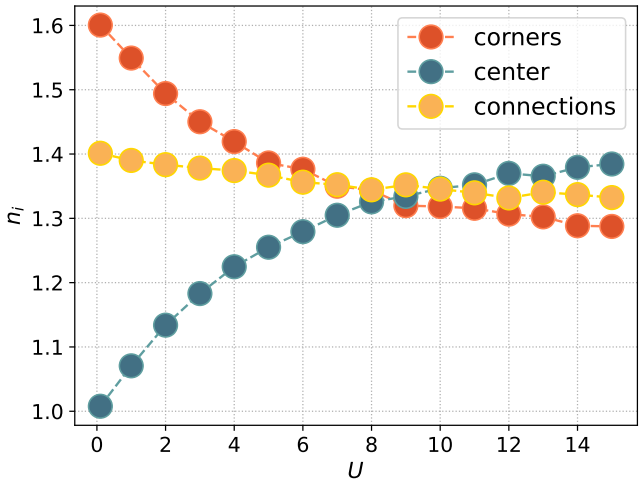

Figure 5.7: Average density per site n_i as a function of interaction strength U in the three different groups of states.

observe that at small interaction both corners and connections sites are more populated than the center sites. As the interaction increases, their density decreases, while it grows in the sites at the center. The electrons start spreading on the lattice, and they keep spreading until the density is approximately homogeneous on every site, at a value of approximately $n_i \sim 1.35$ and $U \sim 8$. Thereafter, the density in the center sites continues to increase, while decreasing slowly on the rest of the lattice sites, meaning that electrons start to accumulate in the center sites. Apparently, for very strong interaction values it becomes more favourable to stuck electrons in sites with more connectivity where hopping is more probable.

Relating this study to the tight-binding considerations and the CLS type-1, discussed in section (4.2.1), we expect that those type of states with destructive interference on center sites get destroyed as soon as the interaction is turned on, since the density on those sites increases.

Finally, we want to check if the QMC solves the problem of computing average density configurations in states belonging to a degenerate level of eigenstates. To this end, let us consider the second generation of the unfrustrated lattice at half-filling. The 12th eigenstate in order of increasing energy belongs to the degenerate zero-energy level and the corresponding average density configuration does not have the expected symmetry properties in MF results. We observe, as shown in Figure (5.8), that QMC solves this issue and correctly calculates a unitary average density per site, as expected form PHT, see Appendix (A).

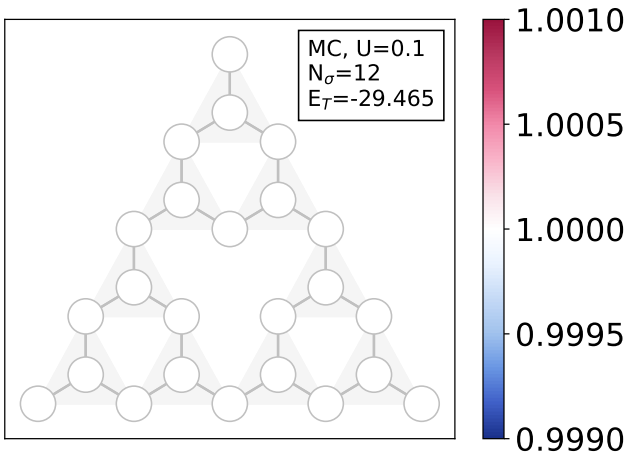

Figure 5.8: Average density configuration in the second generation of the Sierpinski lattice with interaction strength $U = 0.1$, computed in the QMC method.

5.4.3 Quantum Phases in the second generation

Before analysing the phases of the model on the fractal lattice, we recall some known results for a similar lattice structure: the honeycomb lattice. As discussed in the introduction to the Hubbard Model in section (3.3), QMC simulations [32] revealed a phase transition from a nonmagnetic semi-metal to an antiferromagnetic (AF) insulator for a critical value of $U_c/t = 4.5 \pm 0.5$. The existence of this transition was extensively corroborated by many studies, including a recent paper [40] that compares different numerical methods to describe the transition. In the latter study, in was found that the staggered magnetization is null in the semi-metallic phase but finite in the AF phase.

We consider a configuration at half-filling since, as discussed in the introductory section on the Hubbard Model, we know that the system in this condition has antiferromagnetic order at strong interaction. Previous to the implementation of the results that will follow in this section, we performed various simulations for different values of effective interaction for the MF ansatz. We found that choosing $U_{eff} = U$ for $U < 5$ and $U_{eff} = 5$ for $U \geq 5$ gives better approximations to the ground state energy. From now on, we consider $U_{eff} = \min(U, 5t)$.

Let us start studying the behaviour of the magnetisation. To do so, it is convenient to divide the lattice structure in two sub-lattices. This is possible in this case because the lattice is bipartite, the two sub-lattices lattices $\mathcal{A}$ and $\mathcal{B}$ are shown in the introductory chapter on fractals (2.3). We define the local magnetization m_i and the total magnetization m_α per sub-lattice as

$$m_i = (n_{i\uparrow} - n_{i\downarrow}),$$

$$m_\alpha = \frac{1}{N_\alpha} \sum_{i \in \alpha} m_i,$$

where the index α refers to sublattice. Figure (5.9) shows the magnitude of the local magnetization for weak interaction on the lattice structure. We see that the magnetization on different sublattices has opposite sign, and the magnitude of one is larger than the magnitude of the other. This type of phase is called *ferrimagnetic*.

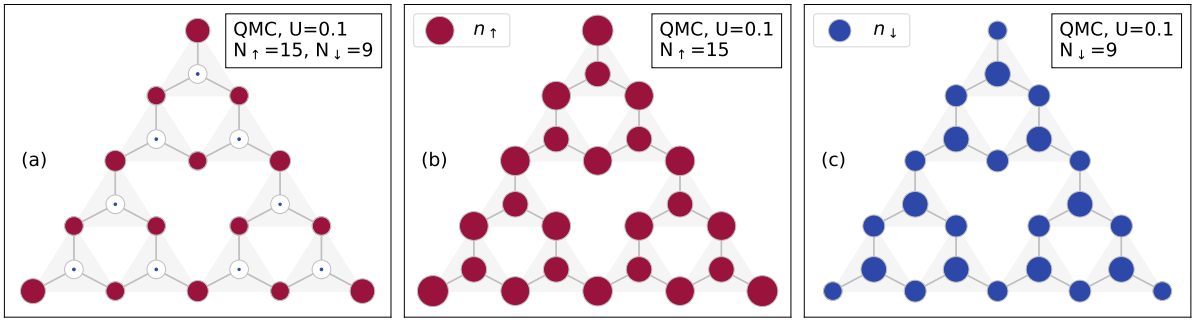

Figure 5.9: Behaviour of average densities and local magnetization of the ground-state at half-filling and weak interaction strength ($U = 0.1$). (a) Local magnetization per site m_i. The size of the dots represents its magnitude and the color its sign: dark-red is positive, blue is negative. (b) Average density of spin-up electrons per lattice site, (c) average density of spin-down electrons per lattice site. The size of the dots represents the magnitude of the density, the color does not represent the sign but spin of the electrons populating the lattice.

We also notice that the values of the spins on the lattice does not sum to zero. This means that the ground state of the system at half filling has an imnbalance in the number of electrons with spin-up and spin-down. In particular, we found that these numbers correspond to the number of sites in the two sublattices. Indeed, for the case of the second generation of the Sierpinski triangle, we have $N_{\mathcal{A}} = 15$ and $N_{\mathcal{B}} = 9$. Without loss of generality, we investigate the case with $N_{\uparrow} = N_{\mathcal{A}}$ and $N_{\downarrow} = N_{\mathcal{B}}$. The opposite case is obtained by inverting the positive direction along the axis where the spin is projected. In Figure 5.9(b) and Figure 5.9(c) we show the distribution of the 15 spin-up and the 9 spin-down electrons on the lattice, in the weak interacting regime. We can interpret Figure 5.9(b) by considering that the 9 spin-up and spin-down electrons fill the single-particle energy levels with negative energy, Figure 4.13(a). The remaining 6 spin-up electrons are placed in the degenerate zero-energy level. In this level, the CLS have destructive interference on the sites in the centre and sites on sublattice $\mathcal{A}$ get more densely populated. Therefore, the origin of imbalanced magnetic properties at half-filling and weak interaction can be reconnected to the zero-energy CLS that we found at a tight-binding level.

Now, we want to investigate the behaviour of the system when increasing the interaction strength. First, we noticed that the imbalance between spin-up and spin-down electrons remains when increasing the interaction strength. Regarding the local magnetization, in Figure (5.10) we show the total magnetization in the two sublattices as a function of interaction strength. We observe that the sum of the magnetization in two sublattices almost does not change. This quantity represents the total magnetization along a projection axis and, since the ratio of number of spin-up

and spin-down electrons remains unchanged, we expect a constant behaviour. However, we need to take into account the fact that the number of spin-up and spin-down electrons is an output of the QMC simulation and, thus, subject to subtle fluctuations. The thoery predicts antiferromagnetic behaviour in the strong coupling regime, where the average local magnetization per site, in both sublattices, is $m_\alpha = 1$. The reason why we are not able to see this behaviour is due to the imbalance in the number of electrons that populated the system which, in turn, is a consequence of the geometry of the lattice.

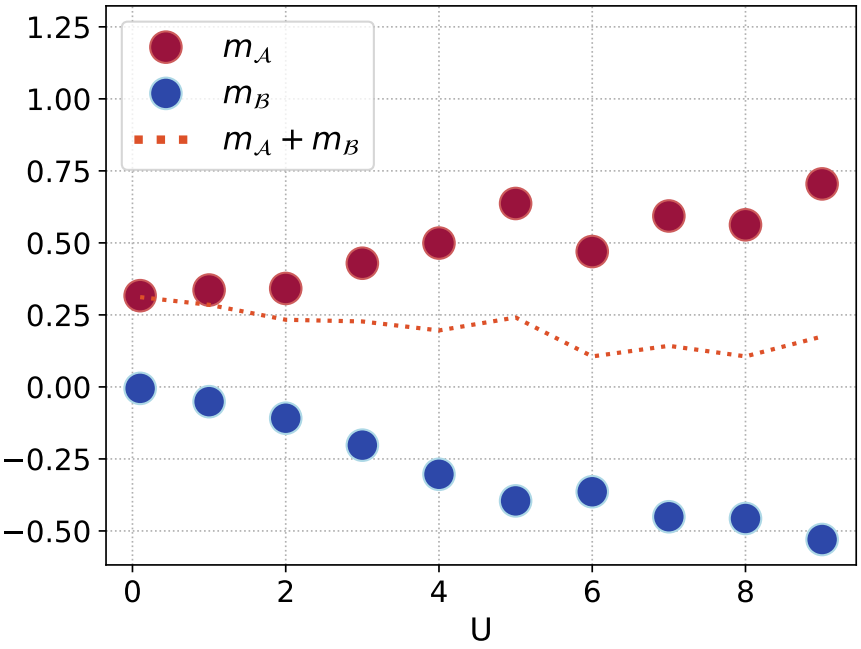

Figure 5.10: Average magnetization over the two different sublattices $\mathcal{A}$ and $\mathcal{B}$ as a function of interaction strenght.

We then consider the average of the squared magnetization

$$\langle m^2 \rangle = \frac{1}{N} \sum_i \langle {m_i}^2 \rangle \,, \tag{5.22}$$

where we can expand the terms in the sum performing the square

$$\langle m_i^2 \rangle = \langle (n_{i\uparrow} - n_{i\downarrow})^2 \rangle = \langle n_{i\uparrow}^2 \rangle + \langle n_{i\downarrow}^2 \rangle - 2 \langle n_{i\uparrow} n_{i\downarrow} \rangle$$

The first term on the right-hand side can be simplified using Wick's theorem and the commutation relations between creation and annihilation operators

$$\langle n_{i\uparrow}^2 \rangle = \langle c_{i\uparrow}^\dagger c_{i\uparrow} c_{i\uparrow}^\dagger c_{i\uparrow} \rangle = \langle c_{i\uparrow}^\dagger c_{i\uparrow} \rangle \langle c_{i\uparrow}^\dagger c_{i\uparrow} \rangle + \langle c_{i\uparrow}^\dagger c_{i\uparrow} \rangle \langle c_{i\uparrow} c_{i\uparrow}^\dagger \rangle = \langle n_{i\uparrow} \rangle \,,$$

where, in the last step, we used the commutation relations between creation and annihilation operators. The same holds for $\langle n_{i\downarrow} \rangle$. In Appendix (A), we showed that at half-filling the average

density per site is unitary. Since in this section we restrict our study to half-filling, we can set $\langle n_i \rangle = 1$. Therefore, the average of the magnetization squared can be written as

$$\langle m^2 \rangle = 2\,(1 - D)\,,$$

where we defined the quantity

$$D = \frac{1}{N} \sum_i \langle n_{i\uparrow} n_{i\downarrow} \rangle$$

known as *doublon density*. The latter is easily computed from the potential energy, and quantifies the density of doubly occupied states. In Figure (5.11), we show the result of QMC simulations that compute both these quantities on the second generation at half-filling. While being easy

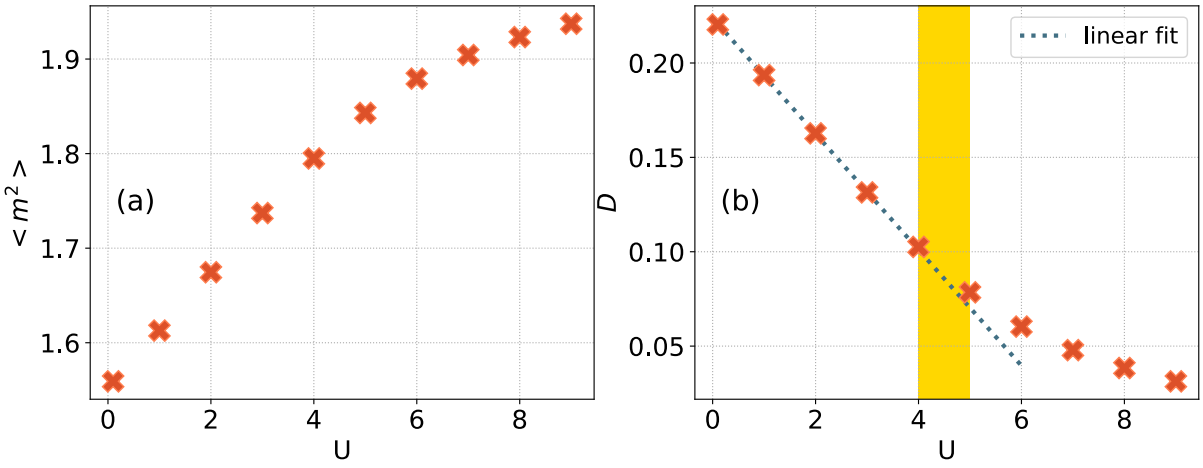

Figure 5.11: In (a) average of magnetization squared $\langle m^2 \rangle$ and in (b) doublon density D for increasing values of interaction strength. A linear fit is preformed for values of doublon density in the region $U \in [0.1, 4]$.

to compute, the double occupancy has the advantage of being related to the metallic behaviour of the system. Moreover, studies on periodic lattices suggest that its behaviour should differentiate metallic and insulating phases. In particular, Brinkman and Rice [41] derived, through a variational calculation, that the doublon density behaves linearly in the metallic phase. Even if this result was derived in the context of conventional band theory, we observe in Figure 5.11(b) a linear behaviour of D until a critical value of approximately $U_c/t \sim 4.5$, where the metallic to insulating transition is expected in the honeycomb lattice. After this value of interaction strength, the behaviour deviates from the linear one.

In order to further analyze the magnetic nature of the system at different values of interaction, and to have more insights on possible phase transitions, we consider the *magnetic correlation function*,

$$c_m(i, j) = \langle m_i m_j \rangle\,,$$

which quantifies the correlation between the local magnetization of a pair of electrons, one placed at site i and one at site j. From this quantity, we can define the *radial magnetic correlation*,

$$c_m(\boldsymbol{r}) = \frac{1}{n_{\boldsymbol{r}}} \sum_{\{i,j\} \in n_{\boldsymbol{r}}} c_m(i, j),$$

where $n_{\boldsymbol{r}}$ is the number of pairs $\{i, j\}$ that have the same distance $\boldsymbol{r}$. This quantity averages the magntic correlation functions of pairs of electrons located at sites $\boldsymbol{r}$ far from each other. The set of possible distances $\boldsymbol{r}$ is discrete, and it is important to notice that, for a given distance, all the pairs connect sites belonging either to the same sublattice or to different sublattices. In Figure 5.12(a) we show the dependence of this correlation on the radial distance $\boldsymbol{r}$. The be-

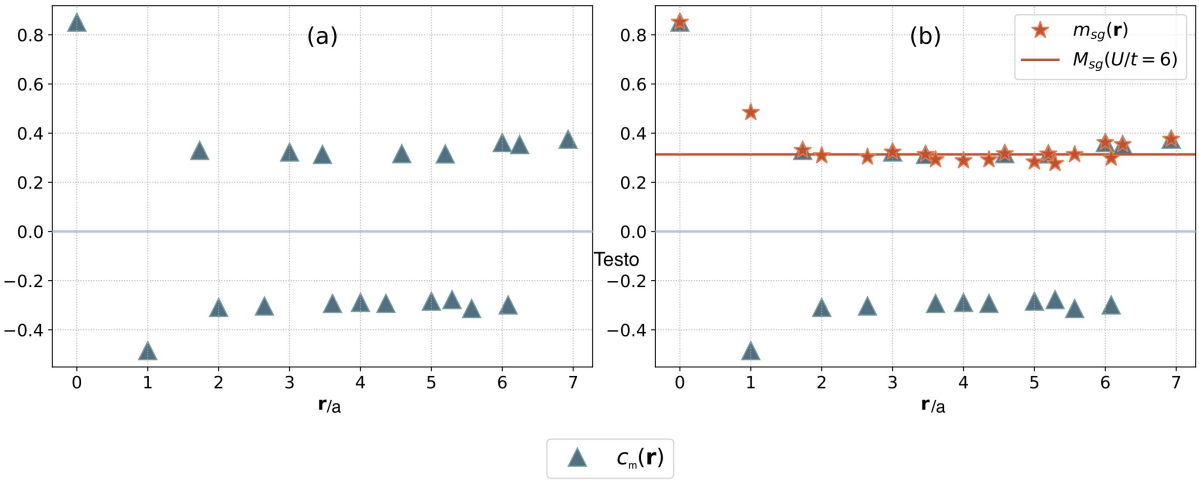

Figure 5.12: (a) Radial magnetic correlation, (b) staggered radial magnetic correlation. These plots were generated for $U = 6$.

haviour shows positive and negative correlations, which indeed can indicate antiferromagnetic or ferrimagnetic order. One of the properties of anti and ferrimagnetism is to have spin orientations that alternate in the lattice. This means that electrons on sites belonging to the same sublattice should have spins oriented to the same direction (the correlation is positive) while electrons on sites belonging to different sublattices should have spins pointing in opposite direction (the correlation is negative). To check this, we multiply the spin radial correlation by a factor $(-1)^{\alpha}$, where α is even (odd) if sites i, j belong to the same (different) sublattice. The quantity obtained will be referred to as *radial staggered magnetization*,

$$m_{sg}(\boldsymbol{r}) = \frac{1}{n_{\boldsymbol{r}}} \sum_{\{i,j\} \in n_{\boldsymbol{r}}} (-1)^{\alpha} c_m(i, j).$$

In Figure 5.12(b), we see the result of this multiplication. We can conclude that the property of opposite spins in different sublattices is satisfied, as expected from the analysis on the local magnetization for the different lattice sites.

In order to study the magnetic order at different values of interaction, we investigate the *total staggered magnetization*,

$$M_{sg} = \frac{1}{N_{\boldsymbol{r}}} \sum_{i_{\boldsymbol{r}}} m_{sg}(\boldsymbol{r}),$$

where the sum is over the number of possible distances $N_{\boldsymbol{r}}$. This quantity represents the average staggered magnetization over different values of radial distances. The resulting behaviour is shown in Figure (5.13), where we see that the value increases with the interaction before the

critical interaction around $U_c \sim 4.5$. After it seems to oscillate without an overall growth or decrement for larger U.

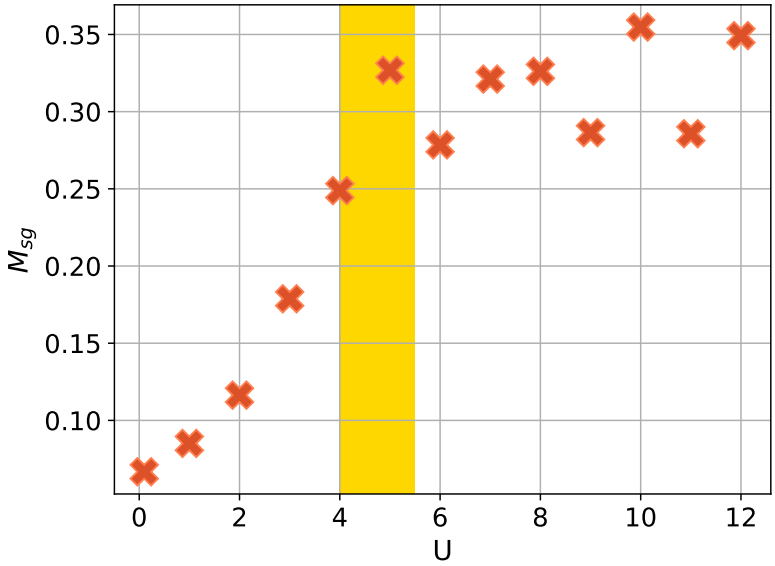

Figure 5.13: Total staggered magnetization as a function of interaction strength.

From the magnetic correlation, one can compute the *magnetic structure factor*, defined as

$$S(\boldsymbol{k}) = \frac{1}{N^2} \sum_{i,j} e^{i\boldsymbol{k}\cdot\boldsymbol{r}_{ij}} c_m(i,j),$$

where $\boldsymbol{r}_{ij} = \boldsymbol{r}_i - \boldsymbol{r}_j$. It is possible to define a similar quantity, where instead of considering magnetic correlations, one considers density correlations. The computation of magnetic and density structure factors is a common method used to investigate both the metallic and spin phases of the system. In particular, the behaviour of the density structure factor around the origin $\boldsymbol{k} = 0$ enables to differentiate between metallic and insulating phases. The former follows from a linear behaviour, whereas the latter from a quadratic one [42]. However, in order to investigate this behaviour, one should be able to compute the allowed momenta in the reciprocal space. In the case of our finite and non-periodic lattice, the reciprocal space and, thus, the allowed momenta, are not defined. The magnetic structure factor is used to detect magnetic order. Aside from getting information from its behaviour around the origin in the reciprocal space, it shows peaks on the K points of the Brillouin zone [3] and the analysis of the intensity of these peaks as a function of the interactions strength could reveal the formation or not of a magnetic order. This method can be followed in our context because it does not require knowledge of allowed momenta in the reciprocal space.

In Figure 5.14(a), we show the magnetic structure factor in the strong interaction regime, where we see the formation of peaks, which are a signature of magnetic order. We observed that these peaks do not form in the K_{hon} points of the honeycomb lattice, which are positioned at

$$K_{hon} = \frac{4\pi}{3a\sqrt{3}}.$$

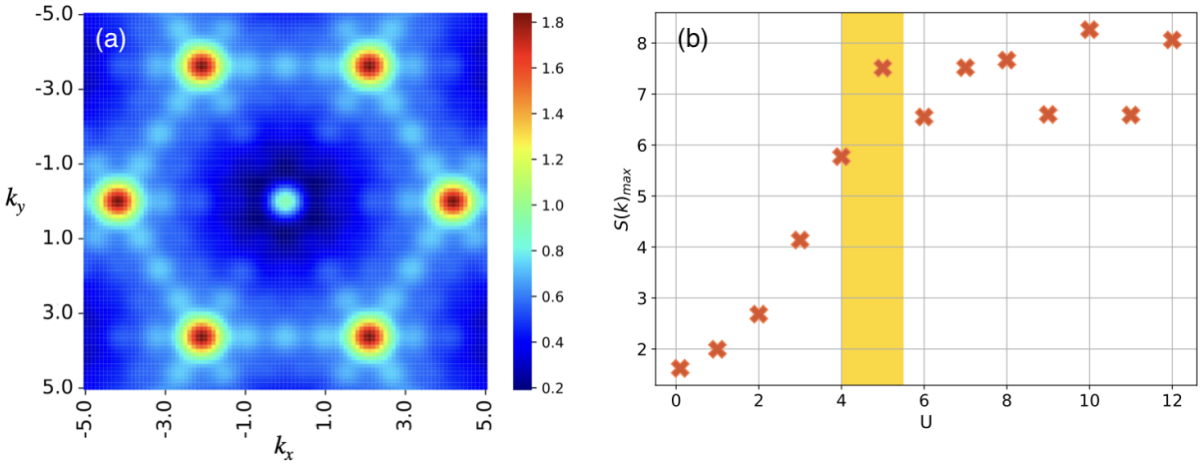

Figure 5.14: (a) Structure factor in the $\boldsymbol{k}$ space and $U = 1$. (b) Maximum value of structure factor for increasing interaction strength.

We then computed the spin-spin structure factor for various values of interaction and we found a similar structure for each value. This seems to suggest that the system has spin order for any value of interaction strength. For each of these configuration, we singled out the maximum value, i.e. the value in the peaks, and studied its behaviour, shown in Figure 5.14(b).

Overall, we observe the formation of a ferrimagnetic order, which can be related, at weak interaction, to the zero-energy CLS states studied at a tight-binding level and, more in general, to the imbalance in the number of spin-up and spin-down electrons. The latter, is a consequence of the geometry of the lattice. We observe a phase transition from metallic to insulating phase, suggested by the change in behaviour of the doublon density, the total staggered magnetization and the maximum of the magnetic correlation function in $\boldsymbol{k}$ space. Since this phase transition is driven by interaction between electrons, it is a Mott transition. Our results agree with the picture in the ordinary honeycomb lattice regarding the Mott transition for a very similar critical value $U_c \simeq 4.5$[32]. The difference is in the magnetic order, that we find to be ferrimagnetic for every value of interaction strength. The latter result, in turn, agrees with studies of Hubbard model on non-periodic lattices, such as the two-dimensional hexagonal golden-mean tiling [40].

6 | Conclusions and Outlooks

In this thesis, we have successfully solved the Hubbard Model, for fermions on a fractal lattice, using various methodologies. Initially, we examined the non-interacting case of the model, employing a tight-binding approach. Subsequently, we numerically implemented the full model, including the interaction term, utilizing three distinct numerical simulations. The first approach involved exact diagonalization, which is an exact method but limited in computational scalability. Therefore, we employed it primarily for validating the results obtained from the other two numerical methods, specifically for smaller system sizes and lower electronic fillings. The second approach entailed employing a mean-field Hartree-Fock approximation, which offers analytical insights but is observed to be valid only for relatively weak interaction strengths.

The primary method, extensively employed in this study, is CP-AFQMC. This method utilizes the mean-field solution as a starting point and evolves it in imaginary time. As the imaginary time becomes large, the solution converges to the ground state of the system. The evolution in imaginary time is implemented by employing a Hubbard-Stratonovich transformation, which decouples the two-body interaction term into one-body terms coupled to auxiliary external fields. To overcome the sign problem, arising from the fermionic nature of the wave function, we employ a constrained-path technique, restricting the sampling of auxiliary fields. This approach enables the computation of various observables. For observables that do not commute with the Hamiltonian, we utilized a back-propagation technique. It is important to notice that the CP approximation introduces a systematic error. Nevertheless, a comparison with exact diagonalization substantiates its validity for all interaction strengths considered.

Regarding the results obtained at the tight-binding level, we successfully confirmed the presence of particle-hole symmetry through the examination of the average density distribution on the lattice and the symmetry of the total many-body energy. Additionally, by analyzing the energy spectrum of the Hamiltonian at the single-electron level, we identified the emergence of CLS at various energy levels. In the first generation, we observed the formation of a specific type of CLS, characterized by zero energy and destructive interference on sites with a connectivity of 3. Moving to the second generation, we witnessed the appearance of an additional type of CLS, manifesting at energy levels of t and $-t$, and displaying destructive interference along the reflection axes. Progressing to the third generation, we observed the emergence of even more diverse types of CLS, forming at new energy values and exhibiting destructive interference on other sub-lattices within the lattice configuration. Remarkably, the number of CLS at

each energy level increased in higher generations of the fractal, scaling with the dimension of the fractal $d \simeq 1.58$. This result resembles the analysis of the study of HOTI on the Sierpinksi carpet[7], where outer corner modes with the same dimension of the fractal were found. Unlike their framework, in our system there is no need for an external magnetic flux to give rise to this interesting connection between outer modes and fractal dimension. Furthermore, we established a connection between the number of CLS and the symmetries of the lattice. Finally, we discovered that the density at the corners, for configurations with a number of electrons that fills the degenerate level at zero energy, closely approximates the dimension of the fractal across all generations of the lattice.

When examining the effects of interaction, the application of CP-AFQMC enabled a comprehensive exploration of the density configurations. By concentrating on the electronic filling value that displayed density patterns closely aligned with the dimension of the fractal at the corners, we observed notable changes in the density distribution upon introducing interaction. Notably, we demonstrated that under strong interaction, sites with higher connectivity, where destructive interference occurred under weak interaction, became more populated as a countermeasure against the effects of interaction. We observe a decrease in the density at the corners as soon as interaction is introduced, leading us to the conclusion that the CLS of type-1 are not robust in the presence of interaction.

We further employed CP-AFQMC to investigate the quantum phases of the system within the second generation of the lattice at half filling, considering non-zero interaction strengths. Initially, we observed that the simulation reached an equilibrium state characterized by an unequal number of spin-up and spin-down electrons, corresponding to the sizes of the two sub-lattices. Our subsequent focus shifted towards studying the magnetic order within the system. To accomplish this, we computed the local magnetization per site and discovered that neighboring sites exhibited opposingte signs and varying magnitudes. This was consistently observed across all interaction strengths and indicated the presence of a ferrimagnetic phase. We were able to establish a connection between the imbalance in local magnetization and the Type-1 CLS under weak interaction. Subsequently, we verified the magnetic order by observing prominent peaks in the magnetic structure factor. Lastly, we detected a Mott transition by analyzing the behavior of the peak values in the structure factor and the doublon density. This transition occurred at an approximate value of $U/t \simeq 4.5$, which intriguingly aligns with the critical value detected through QMC methods for a Mott transition on a honeycomb lattice [32], the periodic lattice configuration most similar to our chosen lattice structure.

As we conclude this thesis, there remain several intriguing open questions for further exploration. It would be interesting to investigate other fractal lattices with dimensions between 1 and 2, to determine whether the results we obtained can be generalized to different types of fractal configurations. An advantage of the CP-AFQMC simulations, employed in this study, is their versatility, as they could be applied to analyze quantum systems on any lattice configuration. From the Sierpinski triangle, we could, for example, place only sites in the center of

the configuration. This lattice geometry, could not only confirm our findings but also give rise to intriguing phases of matter, including spin liquids, due to its inherent magnetic frustration. Additionally, a prospect involves validating our findings by extending the study to fractal lattices with dimension between 2 and 3. Although computationally demanding, such a study would provide a robust foundation for our results. Finally, a valuable validation of our findings could stem from the analytical generalization of methods employed in one dimension, such as the Bethe ansatz, which could be generalized to analytically solve the model [30]. These potential avenues for future research would further corroborate our understanding of the behavior of particles on fractal lattices and strengthen the significance of our findings.

Acknowledgements

I am very grateful to everyone who played a part in making this work possible, as well as those who supported me during this period. Your encouragement has been invaluable.

I would like to start from my supervisor, Cristiane, for her attentive guidance throughout this project. Her intelligence and determination have been a constant source of inspiration for me. Additionally, I would like to extend my thanks to my daily supervisor, Vinicius. His fundamental contribution has made this work possible, and his guidance, availability, and support have been invaluable. I am also grateful for all the knowledge and insights I have learned from him along the way.

I extend my sincere thanks to all those who have made significant contributions to this work. Firstly, I am deeply grateful to Malte Röntgen for his invaluable insights on the study of the tight-binding model, which greatly enriched the analysis. His interest and support were truly encouraging. Additionally, I would like to express my gratitude to Tiago do Espirito Santo for his contributions during the initial stages of the thesis. Lastly, I would like to extend my appreciation to the entire research group led by Cristiane for the engaging and insightful discussions.

I am incredibly grateful to my friends, who contributed by supporting me and creating memories I will always cherish. In particular, I want to thank Riley and Mithuss for the long study sessions and for the amazing time we spent together. Takumi Ramen consolidated our friendship, and I am looking forward to the many times we will go back. I also want to thank Marco for always being there, your friendship means the world to me.

Finally, I would like to thank my parents, Elena and Walter. Their support and encouragement have been crucial, and I will always be grateful for it.

Bibliography

[1] Aaron Szasz et al. "Chiral Spin Liquid Phase of the Triangular Lattice Hubbard Model: A Density Matrix Renormalization Group Study". In: *Physical Review X* 10.2 (May 2020). DOI: 10.1103/physrevx.10.021042. URL: https://doi.org/10.1103%2Fphysrevx.10.021042.

[2] Vito Marino, Federico Becca, and Luca Fausto Tocchio. "Stripes in the extended $t - t$ \prime$Hubbard model : AVariational Monte Carlo analysis$". In: *SciPost Physics* 12.6 (June 2022). DOI: 10.21468/scipostphys.12.6.180. URL: https://doi.org/10.21468%2Fscipostphys.12.6.180.

[3] Vinicius Zampronio and Tommaso Macrì. *Chiral superconductivity in the doped triangular-lattice Fermi-Hubbard model in two dimensions*. 2022. arXiv: 2210.13551 [cond-mat.str-el].

[4] M. Frame and A. Urry. *Fractal Worlds: Grown, Built, and Imagined*. Yale University Press, 2016. ISBN: 9780300197877. URL: https://books.google.nl/books?id=Qm6PjgEACAAJ.

[5] S. N. Kempkes et al. "Design and characterization of electrons in a fractal geometry". In: *Nature Physics* 15.2 (Nov. 2018), pp. 127–131. DOI: 10.1038/s41567-018-0328-0. URL: https://doi.org/10.1038%2Fs41567-018-0328-0.

[6] Xiao-Yun Xu et al. "Quantum transport in fractal networks". In: *Nature Photonics* 15 (Sept. 2021), pp. 1–8. DOI: 10.1038/s41566-021-00845-4.

[7] Junkai Li et al. *Higher-order topological phase in an acoustic fractal lattice*. 2022. arXiv: 2205.05298 [cond-mat.mes-hall].

[8] Wladimir A. Benalcazar, B. Andrei Bernevig, and Taylor L. Hughes. "Quantized electric multipole insulators". In: *Science* 357.6346 (July 2017), pp. 61–66. DOI: 10.1126/science.aah6442. URL: https://doi.org/10.1126%2Fscience.aah6442.

[9] Martin C. Gutzwiller. "Effect of Correlation on the Ferromagnetism of Transition Metals". In: *Phys. Rev. Lett.* 10 (5 Mar. 1963), pp. 159–162. DOI: 10.1103/PhysRevLett.10.159. URL: https://link.aps.org/doi/10.1103/PhysRevLett.10.159.

[10] J. Kanamori. "Electron Correlation and Ferromagnetism of Transition Metals". In: *Progress of Theoretical Physics* 30.3 (Sept. 1963), pp. 275–289. DOI: 10.1143/PTP.30.275.

[11] J. Hubbard and Brian Hilton Flowers. "Electron correlations in narrow energy bands". In: *Proceedings of the Royal Society of London. Series A. Mathematical and Physical Sciences* 276.1365 (1963), pp. 238–257. DOI: 10.1098/rspa.1963.0204.

[12] D. Eichenberger and D. Baeriswyl. "Superconductivity and antiferromagnetism in the two-dimensional Hubbard model: A variational study". In: *Phys. Rev. B* 76 (18 Nov. 2007), p. 180504. DOI: 10.1103/PhysRevB.76.180504. URL: https://link.aps.org/doi/10.1103/PhysRevB.76.180504.

[13] Jie Xu et al. "Spin- and charge-density waves in the Hartree–Fock ground state of the two-dimensional Hubbard model". In: *Journal of Physics: Condensed Matter* 23.50 (Nov. 2011), p. 505601. DOI: 10.1088/0953-8984/23/50/505601. URL: https://doi.org/10.1088%2F0953-8984%2F23%2F50%2F505601.

[14] Wei-Chih Chen, Yao Wang, and Cheng-Chien Chen. *Superconducting Phases of the Square-Lattice Extended Hubbard Model*. 2022. arXiv: 2206.01119 [cond-mat.supr-con].

[15] Aaron Szasz et al. "Chiral Spin Liquid Phase of the Triangular Lattice Hubbard Model: A Density Matrix Renormalization Group Study". In: *Physical Review X* 10.2 (May 2020). DOI: 10.1103/physrevx.10.021042. URL: https://doi.org/10.1103%2Fphysrevx.10.021042.

[16] Luca Fausto Tocchio, Federico Becca, and Arianna Montorsi. "Superconductivity in the Hubbard model: a hidden-order diagnostics from the Luther-Emery phase on ladders". In: *SciPost Physics* 6.2 (Feb. 2019). DOI: 10.21468/scipostphys.6.2.018. URL: https://doi.org/10.21468%2Fscipostphys.6.2.018.

[17] Henrik Bruus and Karsten Flensberg. *Many-body quantum theory in condensed matter physics - an introduction*. English. United States: Oxford University Press, 2004.

[18] H.T.C. Stoof, D.B.M. Dickerscheid, and K. Gubbels. *Ultracold Quantum Fields*. Theoretical and Mathematical Physics. Springer Netherlands, 2008. ISBN: 9781402087639. URL: https://books.google.nl/books?id=-9c2Ns2J5P4C.

[19] Charles Kittel. *Introduction to Solid State Physics*. 8th ed. Wiley, 2004. ISBN: 9780471415268. URL: http://www.amazon.com/Introduction-Solid-Physics-Charles-Kittel/dp/047141526X/ref=dp_ob_title_bk.

[20] Juan Luis Díaz Jiménez. *Introduction to the Hubbard Model*. URL: https://diposit.ub.edu/dspace/handle/2445/124899.

[21] Nicola Marzari et al. "Maximally localized Wannier functions: Theory and applications". In: *Rev. Mod. Phys.* 84 (4 Oct. 2012), pp. 1419–1475. DOI: 10.1103/RevModPhys.84.1419. URL: https://link.aps.org/doi/10.1103/RevModPhys.84.1419.

[22] Hal Tasaki. *The Hubbard Model: Introduction and Selected Rigorous Results*. 1997. arXiv: cond-mat/9512169 [cond-mat.str-el].

[23] Hans-Peter Eckle. "241Models of Strongly Interacting Quantum Matter". In: *Models of Quantum Matter: A First Course on Integrability and the Bethe Ansatz*. Oxford University Press, July 2019. ISBN: 9780199678839. DOI: 10.1093/oso/9780199678839.003.0008. eprint: https://academic.oup.com/book/0/chapter/367110104/chapter-pdf/45115450/oso-9780199678839-chapter-8.pdf. URL: https://doi.org/10.1093/oso/9780199678839.003.0008.

[24] E. Gottlob and U. Schneider. "Hubbard models for quasicrystalline potentials". In: *Physical Review B* 107.14 (Apr. 2023). DOI: 10.1103/physrevb.107.144202. URL: https://doi.org/10.1103%2Fphysrevb.107.144202.

[25] J. Hubbard and Brian Hilton Flowers. "Electron correlations in narrow energy bands III. An improved solution". In: *Proceedings of the Royal Society of London. Series A. Mathematical and Physical Sciences* 281.1386 (1964), pp. 401–419. DOI: 10.1098/rspa.1964.0190.

[26] Patrick Fazekas. *Lecture Notes on Electron Correlation and Magnetism*. WORLD SCIENTIFIC, 1999. DOI: 10.1142/2945. URL: https://www.worldscientific.com/doi/abs/10.1142/2945.

[27] Masatsugu Sei Suzuki. *Mott insulator and Hubbard model*. URL: https://bingweb.binghamton.edu/~suzuki/SolidStatePhysics/20-2_Mott_insulator_and_Hubbard_model.pdf.

[28] A. H. MacDonald, S. M. Girvin, and D. Yoshioka. "$\frac{t}{U}$ expansion for the Hubbard model". In: *Phys. Rev. B* 37 (16 June 1988), pp. 9753–9756. DOI: 10.1103/PhysRevB.37.9753. URL: https://link.aps.org/doi/10.1103/PhysRevB.37.9753.

[29] Elliott Lieb. *The Hubbard Model: Some Rigorous Results and Open Problems*. 1993. arXiv: cond-mat/9311033 [cond-mat].

[30] Elliott H. Lieb and Werner Liniger. "Exact Analysis of an Interacting Bose Gas. I. The General Solution and the Ground State". In: *Phys. Rev.* 130 (4 May 1963), pp. 1605–1616. DOI: 10.1103/PhysRev.130.1605. URL: https://link.aps.org/doi/10.1103/PhysRev.130.1605.

[31] P. W. Anderson. "The Resonating Valence Bond State in La¡sub¿2¡/sub¿CuO¡sub¿4¡/sub¿ and Superconductivity". In: *Science* 235.4793 (1987), pp. 1196–1198. DOI: 10.1126/science.235.4793.1196. eprint: https://www.science.org/doi/pdf/10.1126/science.235.4793.1196. URL: https://www.science.org/doi/abs/10.1126/science.235.4793.1196.

[32] S. Sorella and E. Tosatti. "Semi-Metal-Insulator Transition of the Hubbard Model in the Honeycomb Lattice". In: *Europhysics Letters* 19.8 (Aug. 1992), p. 699. DOI: 10.1209/0295-5075/19/8/007. URL: https://dx.doi.org/10.1209/0295-5075/19/8/007.

[33] Akihisa Koga and Sam Coates. "Ferrimagnetically ordered states in the Hubbard model on the hexagonal golden-mean tiling". In: *Phys. Rev. B* 105 (10 Mar. 2022), p. 104410. DOI: 10.1103/PhysRevB.105.104410. URL: https://link.aps.org/doi/10.1103/PhysRevB.105.104410.

[34] Alexander Weiße and H. Fehske. "Exact Diagonalization Techniques". In: vol. 739. Dec. 2007, pp. 529–544. ISBN: 978-3-540-74685-0. DOI: 10.1007/978-3-540-74686-7_18.

[35] Huy Nguyen et al. "CPMC-Lab: A Matlab package for Constrained Path Monte Carlo calculations". In: *Computer Physics Communications* 185.12 (Dec. 2014), pp. 3344–3357. DOI: 10.1016/j.cpc.2014.08.003. URL: https://doi.org/10.1016%2Fj.cpc.2014.08.003.

[36] Lev Davidovich Landau and E. M. Lifshits. *Quantum Mechanics: Non-Relativistic Theory*. Vol. v.3. Course of Theoretical Physics. Oxford: Butterworth-Heinemann, 1991. ISBN: 978-0-7506-3539-4.

[37] Nicholas Metropolis et al. "Equation of State Calculations by Fast Computing Machines". In: *The Journal of Chemical Physics* 21.6 (1953), pp. 1087–1092. DOI: 10.1063/1.1699114. URL: http://link.aip.org/link/?JCP/21/1087/1.

[38] J. E. Hirsch. "Two-dimensional Hubbard model: Numerical simulation study". In: *Phys. Rev. B* 31 (7 Apr. 1985), pp. 4403–4419. DOI: 10.1103/PhysRevB.31.4403. URL: https://link.aps.org/doi/10.1103/PhysRevB.31.4403.

[39] Wirawan Purwanto and Shiwei Zhang. "Quantum Monte Carlo method for the ground state of many-boson systems". In: *Physical Review E* 70.5 (Nov. 2004). DOI: 10.1103/physreve.70.056702. URL: https://doi.org/10.1103%2Fphysreve.70.056702.

[40] Akihisa Koga and Sam Coates. "Ferrimagnetically ordered states in the Hubbard model on the hexagonal golden-mean tiling". In: *Phys. Rev. B* 105 (10 Mar. 2022), p. 104410. DOI: 10.1103/PhysRevB.105.104410. URL: https://link.aps.org/doi/10.1103/PhysRevB.105.104410.

[41] W. F. Brinkman and T. M. Rice. "Application of Gutzwiller's Variational Method to the Metal-Insulator Transition". In: *Phys. Rev. B* 2 (10 Nov. 1970), pp. 4302–4304. DOI: 10.1103/PhysRevB.2.4302. URL: https://link.aps.org/doi/10.1103/PhysRevB.2.4302.

[42] Caterina De Franco, Luca F. Tocchio, and Federico Becca. "Metal-insulator transitions, superconductivity, and magnetism in the two-band Hubbard model". In: *Phys. Rev. B* 98 (7 Aug. 2018), p. 075117. DOI: 10.1103/PhysRevB.98.075117. URL: https://link.aps.org/doi/10.1103/PhysRevB.98.075117.

[43] Pierre Ramond. "SU(2)". In: *Group Theory: A Physicist's Survey*. Cambridge University Press, 2010, pp. 78–101. DOI: 10.1017/CBO9780511781865.005.

[44] D. Vollhardt E. Pavarini E. Koch. *The LDA+DMFT approach to strongly correlated materials*. Forschungszentrum Jülich GmbH, Institute for Advanced Simulaton.

[45] Patrick Fazekas. *Lecture Notes on Electron Correlation and Magnetism*. WORLD SCIENTIFIC, 1999. DOI: 10.1142/2945. eprint: https://www.worldscientific.com/doi/pdf/10.1142/2945. URL: https://www.worldscientific.com/doi/abs/10.1142/2945.

A | Particle-Hole Symmetry

In this section, we want to show how the Hubbard Hamiltonian transforms under a particle-hole transformation on the unfrustrated lattice. We consider this lattice because of its property of being bipartite: it can be divided into two sub-lattices $\mathcal{A}$ and $\mathcal{B}$ where each element of $\mathcal{A}$ is only connected to elements of $\mathcal{B}$ and vice-versa. In Figure (2.8) we can see that this is possible. A particle-hole transformation (PHT) consists in the redefinition of the creation and annihilation operators as follows:

$$c_{i\sigma} = \eta_i d^\dagger_{i\sigma} \quad \text{and} \quad c^\dagger_{i\sigma} = \eta_i d_{i\sigma},$$

where $\eta_i = \pm 1$ depending on which sub-lattice the $i-$th site belongs to. This means that when c destroys a particle $d^\dagger$ creates a hole, with a pre-factor η.
The kinetic term the Hamiltonian contains terms that are invariant under this transformation, in fact:

$$c^\dagger_{i\sigma} c_{j\sigma} = \eta_i \eta_j d_{i\sigma} d^\dagger_{j\sigma}.$$

The pre-factor containing η contributes with a minus sing since the sum in the Hamliltonian is over nearest-neighbours, which belong to different sub-lattices. This is also the reason why the operators $d_{i\sigma}$ and $d^\dagger_{j\sigma}$ anti-commute, cancelling the negative sign of the pre-factor and leaving the kinetic term as

$$c^\dagger_{i\sigma} c_{j\sigma} = d^\dagger_{j\sigma} d_{i\sigma}.$$

Regarding the interaction term, it can be written in the same form using hole creation and annihilation operators with an additional term in the Hamiltonian that accounts for a shift in energy. Let us start transforming the particle number operator:

$$n_{i\sigma} = c^\dagger_{i\sigma} c_{i\sigma} = (\eta_i)^2 d_{i\sigma} d^\dagger_{i\sigma} = 1 - d^\dagger_{i\sigma} d_{i\sigma}, \tag{A.1}$$

where we used $\{d^\dagger_{i\sigma}, d_{i\sigma}\} = 1$, that follows from the anti-commutation relations of the particle operators and from the fact that $(\eta_i)^2 = 1$. Now we consider the contribution of the single sites to the sum in the interacting term and we rewrite it using the relation just derived,

$$n_{i\uparrow} n_{i\downarrow} = (1 - d^\dagger_{i\uparrow} d_{i\uparrow})(1 - d^\dagger_{i\downarrow} d_{i\downarrow}) = 1 - d^\dagger_{i\uparrow} d_{i\uparrow} - d^\dagger_{i\downarrow} d_{i\downarrow} + d^\dagger_{i\uparrow} d_{i\uparrow} d^\dagger_{i\downarrow} d_{i\downarrow},$$

so that we can identify a term similar to the original product of particle number operators, but written as a product of hole number operators $h_{i\sigma} = d^\dagger_{i\sigma} d_{i\sigma}$. Summing over the lattice sites, we can obtain how the interaction term transforms under PHT,

$$U \sum_i h_{i\uparrow} h_{i\downarrow} + U \left(|\Lambda| - N \right),$$

where $|\Lambda|$ is the number of sites and N the number of particles.
The total Hubbard Hamilton after PHT reads as:

$$H' = -t \sum_{\langle i,j\rangle \in \Lambda} \sum_{\sigma} \left(d^{\dagger}_{i\sigma} d_{j\sigma} + \text{h.c.} \right) + U \sum_{i} h_{i\uparrow} h_{i\downarrow} + U \left(|\Lambda| - N \right), \tag{A.2}$$

from which can deduce that for half-filling the system is left invariant by this transformation since $|\Lambda| = N$. Moreover, in such a condition, since the Hamiltonian is the same, we should have that the density of particles equals the density of holes,

$$\langle n_{i\sigma} \rangle = \langle h_{i\sigma} \rangle ,$$

but equation (A.1) suggests that $\langle h_{i\sigma} \rangle = 1 - \langle n_{i\sigma} \rangle$, therefore we obtain that the total average density of particles per site is

$$\langle n_i \rangle = \langle n_{i\uparrow} \rangle + \langle n_{i\downarrow} \rangle = 1. \tag{A.3}$$

B | Slater determinant identity

We are going to prove that, given two Slater determinants $|\Phi\rangle$ and $|\Psi\rangle$, the expectation value of the operators $c_j^\dagger c_i$, satisfies the following identity:

$$\langle c_j^\dagger c_i \rangle = \frac{\langle \Psi | c_j^\dagger c_i | \Phi \rangle}{\langle \Psi | \Phi \rangle} = \left[\Phi [(\Psi)^\dagger \Phi]^{-1} (\Psi)^\dagger \right]_{ij}.$$

The key step of this proof is realizing that the product of operators $c_j^\dagger c_i$ in the expectation value can be substituted by the operator $\hat{O}$, defined by its matrix elements $O_{mn} = \delta_{jm}\delta_{ni}$ in the following way:

$$c_j^\dagger c_i = \sum_{m,n} \delta_{mj}\delta_{ni} c_m^\dagger c_n = \sum_{m,n} O_{mn} c_m^\dagger c_n = \hat{O},$$

where the last step is motivated by

$$\langle m|O|n\rangle = \delta_{mj}\delta_{ni} \quad \text{using} \quad \sum_{m,n} O_{mn} c_m^\dagger c_n = \hat{O}.$$

Therefore, our goal now is to compute the following quantity:

$$G_{ij} = \frac{\langle \Phi | \hat{O} | \Psi \rangle}{\langle \Phi | \Psi \rangle}$$

and we will do it by writing the left term in a convenient way,

$$\frac{\langle \Phi | \hat{O} | \Psi \rangle}{\langle \Phi | \Psi \rangle} = \frac{\partial}{\partial \eta} \ln \langle \Phi | e^{\eta \hat{O}} | \Psi \rangle \Big|_{\eta=0}.$$

Hence, we can apply the Thouless theorem to identify $e^{\eta \hat{O}} |\Psi\rangle$ as a Slater determinant and use the property of the product of Slater determinants:

$$\langle \Phi | e^{\eta \hat{O}} | \Psi \rangle = \det[\Phi^\dagger e^{\eta O} \Psi].$$

Since the determinant of a diagonalizable matrix M can be written as the trace of its logarithm, we can evaluate the desired expectation value:

$$G_{ij} = \frac{\partial}{\partial \eta} \ln \det[\Phi^\dagger e^{\eta O} \Psi] \Big|_{\eta=0} = \frac{\partial}{\partial \eta} \operatorname{Tr} \ln[\Phi^\dagger e^{\eta O} \Psi] \Big|_{\eta=0} = \operatorname{Tr} \frac{\partial}{\partial \eta} \ln[\Phi^\dagger e^{\eta O} \Psi] \Big|_{\eta=0},$$

where we also used the fact that trace and derivative operations commute. We now compute the derivative inside the trace and use its cyclic property to simplify the expression,

$$G_{ij} = \operatorname{Tr} \left[\frac{\Phi^\dagger O e^{\eta O} \Psi}{\Phi^\dagger e^{\eta O} \Psi} \right] \Big|_{\eta=0} = \operatorname{Tr} \left[\frac{\Phi^\dagger O \Psi}{\Phi^\dagger \Psi} \right] = \operatorname{Tr}[(\Phi^\dagger \Psi)^{-1} \Phi^\dagger O \Psi] = \operatorname{Tr}[\Psi (\Phi^\dagger \Psi)^{-1} \Phi^\dagger O],$$

Finally, we call the matrix $\Psi(\Phi^\dagger\Psi)^{-1}\Phi^\dagger = N$ to realize that:

$$\mathrm{Tr}[NO] = \sum_m (NO)_{mm} = \sum_{m,n} N_{mn}O_{nm} = \sum_{m,n} N_{mn}\delta_{jn}\delta_{mi} = N_{ij},$$

which leads to the desired identity:

$$G_{ij} = \frac{\langle\Psi|c_j^\dagger c_i|\Phi\rangle}{\langle\Psi|\Phi\rangle} = [\Psi(\Phi^\dagger\Psi)^{-1}\Phi^\dagger]_{ij}.$$

C | $SU(2)$ Symmetry

The $SU(2)$ group is a special unitary group of complex matrices with unit determinant. The "S" stands for "special" because the determinant of the matrices in the group is required to be 1. The "U" stands for "unitary" because the matrices are required to be unitary, meaning their conjugate transpose is equal to their inverse. The number 2 in the round brackets indicates the lowest non-trivial *Lie algebra* is realized in a 2 dimensional Hilbert space [43]. Due to the constrained imposed by unitary determinant and unitarity of the matrices, the generators are specified by 3 real parameters. It follows that the group has 3 generators, S_x, S_y and S_z. These generators satisfy the algebra:

$$[S_i, S_j] = i\hbar\epsilon_{ijk}S_k,$$

so they do not commute with each other.
In the fundamental representation of the $SU(2)$ group, the spins operators are 2×2 matrices and can be written in terms of creation and annihilation operators as

$$\boldsymbol{S}_i = \frac{1}{2}\sum_{\mu\nu} c^\dagger_{i\mu}\boldsymbol{\sigma}_{\mu\nu}c_{i\nu}$$

or, developing the Pauli matrices,

$$S^x_i = \frac{1}{2}[c^\dagger_{i\uparrow}c_{i\downarrow} + c^\dagger_{i\downarrow}c_{i\uparrow}], \quad S^y_i = \frac{1}{2i}[c^\dagger_{i\downarrow}c_{i\uparrow} - c^\dagger_{i\uparrow}c_{i\downarrow}], \quad S^z_i = \frac{1}{2}[c^\dagger_{i\uparrow}c_{i\uparrow} + c^\dagger_{i\downarrow}c_{i\downarrow}].$$

If we introduce the ladder operators $S^+_i = c^\dagger_{i\uparrow}c_{i\downarrow}$ and $S^-_i = c^\dagger_{i\downarrow}c_{i\uparrow}$, we can rewrite the three operators as:

$$S^x_i = \frac{1}{2}[S^+_i + S^-_i], \quad S^y_i = \frac{1}{2i}[S^-_i - S^+_i], \quad S^z_i = \frac{1}{2}[n_{i\uparrow} + n_{i\downarrow}].$$

The Hubbard Hamiltonian commutes with the three generators of the SU(2) symmetry, from this spin isotropy follows. However, the mean-field approximation in equation (5.17) we modified the interaction term, on which we focus in this appendix. This term can be written using only the z component of the generators of the $SU(2)$ group,

$$\begin{aligned} n_\uparrow n_\downarrow &\simeq \langle n_{i\uparrow}\rangle n_{i\downarrow} + \langle n_{i\downarrow}\rangle n_{i\uparrow} - \langle n_{i\uparrow}\rangle \langle n_{i\downarrow}\rangle \\ &= \frac{1}{2}\left[n\langle n\rangle - 4S^z\langle S^z\rangle - \left(\frac{\langle n\rangle^2}{2} - 2\langle S_z\rangle^2\right)\right], \end{aligned} \tag{C.1}$$

where we introduced $n = n_\uparrow + n_\downarrow$. Therefore, it does not commute with the other two generators of the group, breaking the spin rotational invariance.

In order to find a rotational invariant Hamiltonian, we expand the interaction term using Wick's theorem [44],

$$\begin{aligned} n_{i\uparrow}n_{i\downarrow} &= c^{\dagger}_{i\uparrow}c_{i\uparrow}c^{\dagger}_{i\downarrow}c_{i\downarrow} \\ &\simeq \langle n_{i\uparrow}\rangle n_{i\downarrow} + \langle n_{i\downarrow}\rangle n_{i\uparrow} + \langle n_{i\uparrow}\rangle \langle n_{i\downarrow}\rangle - \langle S^{+}_{i}\rangle S^{-}_{i} - \langle S^{-}_{i}\rangle S^{+}_{i} - \langle S^{+}_{i}\rangle \langle S^{-}_{i}\rangle , \end{aligned} \tag{C.2}$$

where we omitted the contractions that involve two creation or annihilation operators since the total number of particles is conserved. We can rewrite the ladder operators using the the x and y components of the generators of the symmetry in the following way:

$$S^{+}\langle S^{-}\rangle + S^{-}\langle S^{+}\rangle = 2S^{x}\langle S^{x}\rangle + 2S^{y}\langle S^{y}\rangle$$

$$\langle S^{+}\rangle\langle S^{-}\rangle = \langle S^{x}\rangle^{2} + \langle S^{y}\rangle^{2} .$$

These expressions, together with equation (C.1), allow us to write the interaction term as

$$n_{\uparrow}n_{\downarrow} \simeq \frac{1}{2}\left(n\langle n\rangle - 4\boldsymbol{S}_{i}\langle \boldsymbol{S}_{i}\rangle - \frac{\langle n\rangle^{2}}{2} - 2\langle \boldsymbol{S}\rangle^{2}\right),$$

which is now written in terms of all the generators of $SU(2)$, restoring the spin-rotational symmetry [45].